Electrical and Computer Engineering ETDs

Engineering ETDs

8-27-2009

Rectangular waveguide narrow-wall longitudinal-aperture antenna arrays for high-power applications

Naga Ravi Kanth Devarapalli

Follow this and additional works at: https://digitalrepository.unm.edu/ece_etds

RECTANGULAR WAVEGUIDE NARROW-WALL
LONGITUDINAL-APERTURE ANTENNA ARRAYS FOR
HIGH POWER APPLICATIONS

by

DEVARAPALLI, NAGA RAVI KANTH

Bachelor of Engineering, Electronics & Communication, Andhra
University, 2001
Master of Science, Electrical Engineering, University of New Mexico,
2006

DISSERTATION

Submitted in Partial Fulfillment of the
Requirements for the Degree of

Doctor of Philosophy

Engineering

The University of New Mexico
Albuquerque, New Mexico

August 2009

Devarapalli, Naga Ravi Kanth
_____
Candidate

Electrical and Computer Engineering
_____
Department

This dissertation is approved, and it is acceptable in quality
and form for publication:

Approved by the Dissertation Committee:

_____ , Chairperson

_____

_____

_____

_____

_____

_____

_____

To a primal instinct:

The desire to belong to a community, which in

its supreme form, is referred to as

LOVE

&

To:

RIDHIMA and SRIKANTH

ACKNOWLEDGMENTS

**RECTANGULAR WAVEGUIDE NARROW-WALL
LONGITUDINAL-APERTURE ANTENNA ARRAYS FOR
HIGH POWER APPLICATIONS**

by

DEVARAPALLI, NAGA RAVI KANTH

ABSTRACT OF DISSERTATION

Submitted in Partial Fulfillment of the
Requirements for the Degree of

Doctor of Philosophy

Engineering

The University of New Mexico
Albuquerque, New Mexico

August 2009

RECTANGULAR WAVEGUIDE NARROW-WALL LONGITUDINAL-APERTURE ANTENNA ARRAYS FOR HIGH POWER APPLICATIONS

by

Devarapalli, Naga Ravi Kanth

B.E., Electronics & Communication, Andhra University, 2001

M.S., Electrical Engineering, University of New Mexico, 2006

Ph.D., Engineering, University of New Mexico, 2009

ABSTRACT

This work deals with the design and bench test of rectangular waveguide narrow-wall longitudinal-aperture antenna arrays for high power applications. The best narrow-wall longitudinal-aperture array designs in the work are called the double-narrow-wall-slot-HPB-array and the double-split-waveguide-HPB-array. The double-narrow-wall-slot-HPB-array (double-split-waveguide-HPB-array) consists of two identical narrow-wall-slot-HPB-arrays (split-waveguide-HPB-arrays) with a common broad wall.

All elements of the split-waveguide-HPB-array are identical and are called H-plane-bend-radiators (HPB-radiators). An HPB-radiator is an H-plane bend terminating in a radiating aperture with the narrow dimension of the waveguide flaring out. Optimizing the HPB-radiator's performance involves designing its aperture dimensions and the function that determines the H-plane taper to minimize the reflected power into the feed-

waveguide while maintaining a half sine wave aperture electric field (E-field) distribution. Once the optimal HPB-radiator is designed, the design of the split-waveguide-HPB-array is similar to designing a uniform linear array. There is minimal mutual coupling between the elements through the waveguide, and for design purposes, external coupling between the elements can be ignored.

The first four elements of the narrow-wall-slot-HPB-array are longitudinal-slots in the narrow wall of a rectangular waveguide, and the last element is an HPB-radiator with the same optimal performance criteria as that of the split-waveguide-HPB-array. The narrow-wall-slot-HPB-array is designed by a combination of computational and microwave network analysis techniques. First, computational analysis of the individual slots is performed separately. In the next step, each longitudinal-slot in the narrow wall of the guide is reduced to a lossy two port microwave network whose S-parameters have been obtained from the computational analysis; the loss in the network represents the power radiated by the slot. Finally, microwave network analysis is used to design a uniform linear array with a low reflected power into the feed-waveguide. The primary advantage of the split-waveguide-HPB-array over the narrow-wall-slot-HPB-array is its ability to beam steer since the inputs to its elements can be controlled separately.

Since the structures are used for high power applications, the HPB-radiator's H-plane taper function needs to be smooth without any sharp corners. Its design procedure, using just computational or analytical methods, was intractable. The design procedure is therefore formalized using a novel approach, which processes the computational analysis data using iterative search algorithms. This approach is made possible by mapping a design output variable that is computationally intensive, to another that requires much

less computational time. This approach is based on a hypothesis that is called the 'dimensional offset hypothesis'.

The behavior of narrow-wall longitudinal-slots with dimensions comparable to a free-space wavelength is also characterized. The similarities they possess with wire radiators are presented.

The experimental results validate the theoretical analysis results for the design of an HPB-radiator and from the microwave network analysis. The power handling capability analysis for the double-narrow-wall-slot-HPB-array and the double-split-waveguide-HPB-array is also presented.

TABLE OF CONTENTS

LIST OF FIGURES

LIST OF TABLES

0. MOTIVATION

This work deals with the design and bench test of waveguide antennas that can handle high powers. Each antenna should be rugged and have a low profile. The antenna will be front-mounted on a land vehicle.

Most suitable antenna types for high power applications are reflector and waveguide antennas. Two important requirements for a high power antenna are high directivity and low reflected power into the source in addition to the ability to handle high powers. In order to achieve a high gain using a reflector antenna design, the reflector is generally quite big, which makes it less conformal and have higher wind resistance than, for instance, a waveguide slot array that can handle high powers and have a high gain. A reflector antenna is also less rugged than an air-filled waveguide antenna. Unlike the waveguide antenna, taking out just one part of a reflector antenna, specifically its feed, makes it powerless. The waveguide antenna under consideration is an air-filled rectangular waveguide slot array; the slots are longitudinal and are in the narrow wall of the waveguide as shown in Figure 0.1(b). The basic idea for the slot array is described in *[SSN 503]*.

The required radiation pattern along with the polarization of the radiated electric field for the high power antenna to be designed is shown in Figure 0.1(c). The reasons for having longitudinal-slots in the narrow wall of the waveguide are as follows.

Since the waveguide antenna is to be approximately vertically front-mounted, the configuration shown in Figure 0.1(b) is well suited to achieve the radiation pattern and the electric field (E-field) polarization shown in Figure 0.1(c). In addition, it is also advantageous to have slots in the narrow wall of a rectangular waveguide for improving

1

the power handling capabilities of the antenna. For the dominant (TE_{10}) mode of operation for the waveguide, not only the tangential but also the normal component of the E-field at the narrow-wall is zero. The existence of a slot in the narrow-wall presents a discontinuity to the propagating mode inside the waveguide and induces an aperture E-field as shown in Figure 0.1(b).
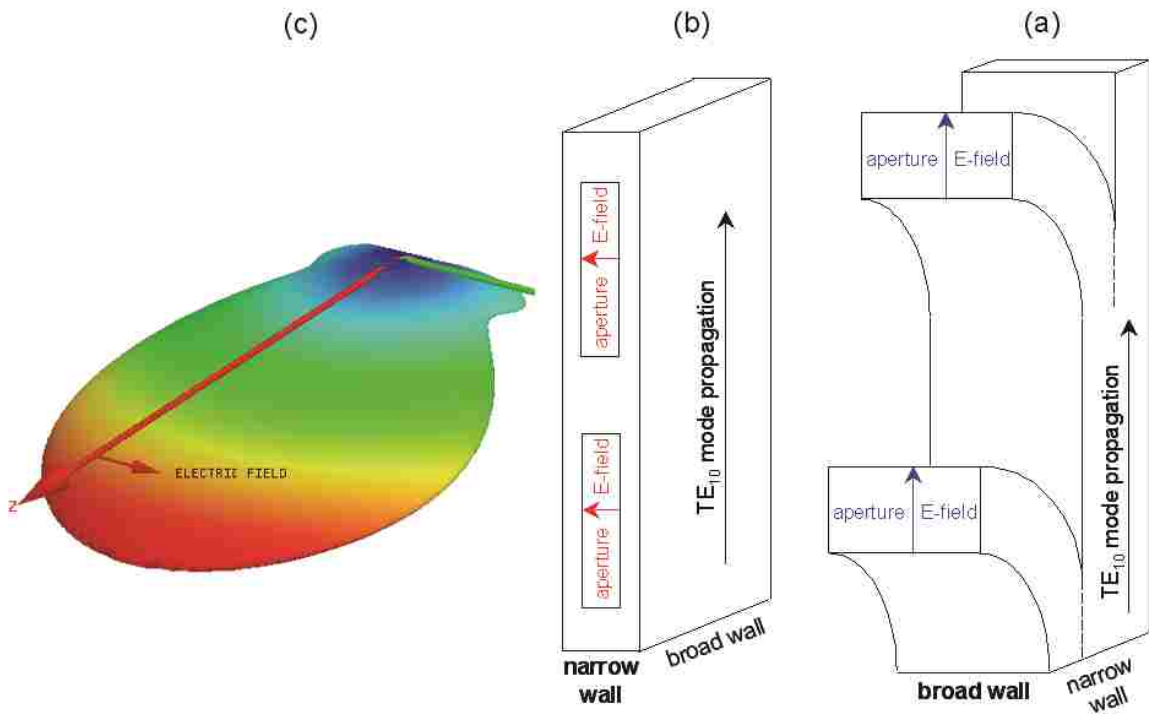
Figure 0.1. (a) Complementary structure to the narrow-wall longitudinal-slot array concept shown in Figure 0.1(b). (b) Schematic of the narrow-wall longitudinal-slot array. (c) Fan beam radiation pattern showing the radiated E-field direction as produced by the narrow-wall longitudinal-slot array in Figure 0.1(b).

The antenna in Figure 0.1(a) is described in *[SSN 459]* and is a complementary structure to the antenna shown in Figure 0.1(b). Both structures produce a similar fan beam radiation pattern as shown in Figure 0.1(c), but with the radiated E-field

polarization of one structure orthogonal to that of the other. Depending on the application, either one or both of the structures shown in Figures 0.1(a) and 0.1(b) is/are required. Therefore, when both structures are used together, they can complement each other. All the high power waveguide antenna arrays designed/tested in this work radiate a similar fan beam radiation pattern with the E-field polarized along the broad dimension of the fan beam pattern as shown in Figure 0.1(c).

Note that a fan beam radiation pattern with two main lobes so as to cover both sides of the road can be obtained as follows. Two identical arrays of the kind shown in Figure 0.1(b) can be approximately vertically front-mounted on the land vehicle. The distance of separation and the input phase difference between the arrays can be adjusted to produce a null in the direction along the center of the road and a fan beam radiation pattern with two main lobes. Each main lobe is similar to the radiation pattern shown in Figure 0.1(c). Hence the two linear arrays perform together to illuminate both sides of the road with a null along the direction of the center of the road.

The operating frequency for the narrow-wall longitudinal-slot array is required to be in the industrial frequency band (902MHz - 928MHz). From the operating frequency, the dimensional constraint on the array is obtained so that the array is front mountable on a land vehicle. However, to facilitate the bench testing process, the array is first designed to operate at 10GHz and is fed by a standard X-band waveguide. The dimensions of the array design in the X-band can then be easily scaled-up accordingly to obtain an array with exactly the same design performance characteristics but operating in the industrial band.

This work is divided into the following six chapters. The first chapter describes the characterization of a generic longitudinal-slot in the narrow wall of a rectangular waveguide. The second chapter describes the design of a novel structure used as the last element of the narrow-wall longitudinal-slot array that enhances the array's performance. The third chapter describes the design of the narrow-wall longitudinal-slot array using microwave theory and computational analysis. The fourth chapter describes a waveguide aperture array, each element of which is a novel structure described in Chapter 2. The split-waveguide-HPB-array described in Chapter 4 has an additional functionality of beam steering capability. The fifth chapter describes the validation of the theoretical results through experiments and the scaling up of the dimensions of the final array designs to operate in the industrial band. Chapter 5 also includes the power handling capability analysis of the final array designs in the industrial band. The sixth chapter describes the future work for designing a circularly polarized waveguide high power antenna and the possibility for further improving the design of the narrow-wall longitudinal-slot array.

Note that all the theoretical design analyses in Chapters 1 through 4 and the experiments in Chapter 5 are at a frequency of 10GHz and with a standard X-band waveguide operating in the TE_{10} mode acting as the feed-waveguide. The dimensions of the optimal array designs at 10GHz obtained from Chapters 3 and 4 are then scaled up to obtain the corresponding array designs operating in the industrial band, in Chapter 5.

1. NARROW-WALL LONGITUDINAL-SLOT RADIATOR

1.1 Small aperture in the narrow wall of a rectangular waveguide

The Scattering analysis of an aperture with dimensions small compared to a wavelength in a ground plane already exists in literature *[Collin]*. The polarizabilities of different shaped apertures have been found using this analysis, and presented in *[Lee]*. These expressions can be conveniently used to study the radiation characteristics of the apertures. The (electric / magnetic) polarizability of an object is the dipole moment induced in it per unit (electric / magnetic) field intensity incident upon it. Hence the electric (magnetic) polarizability, α_e (α_m) and the electric (magnetic) field incident upon a small slot can be used to find the fictitious electric (magnetic) current, $\overline{J}$ ($\overline{M}$) in the slot; i.e. the scattered fields radiated by the slot problem are the same when the slot is replaced by a perfect electric (magnetic) conductor with the equivalent electric (magnetic) current on it. Assuming that a rectangular waveguide is operating in the dominant (TE_{10}) mode, the tangential as well as and the normal components of the E-field at its narrow wall are zero; hence only the magnetic terms, α_m, $\overline{M}$ need to be considered to find the far fields radiated by a narrow longitudinal-slot with dimensions small compared to a wavelength in the narrow wall of a rectangular waveguide. The polarizability of a small and narrow longitudinal slit in the narrow wall of a rectangular waveguide can be used, as described in this section, to find the radiated power by the longitudinal slit in the far field.
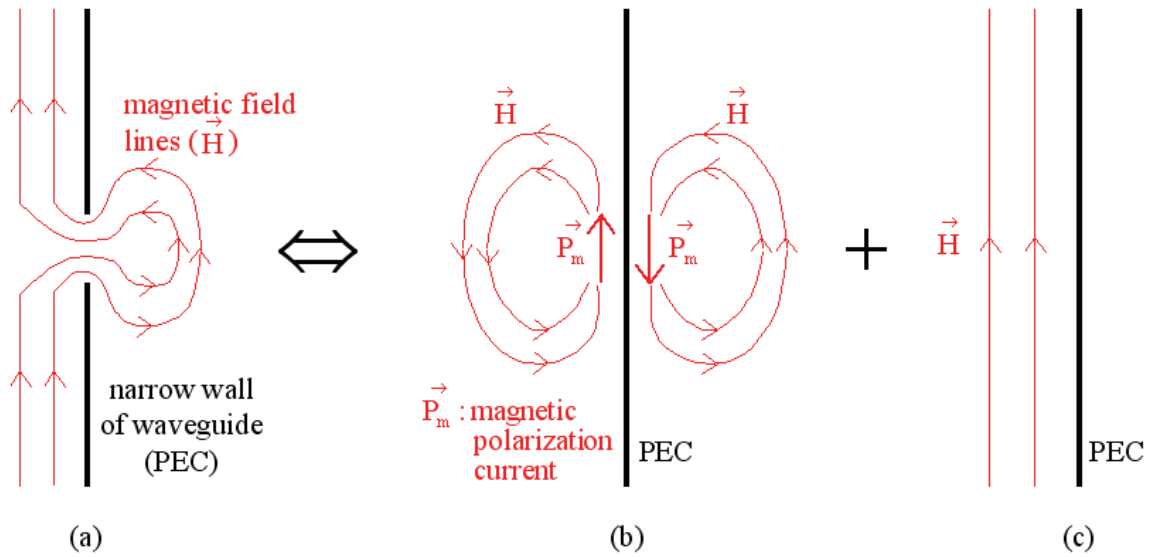
Figure 1.1. Small aperture in the narrow wall of a rectangular waveguide.
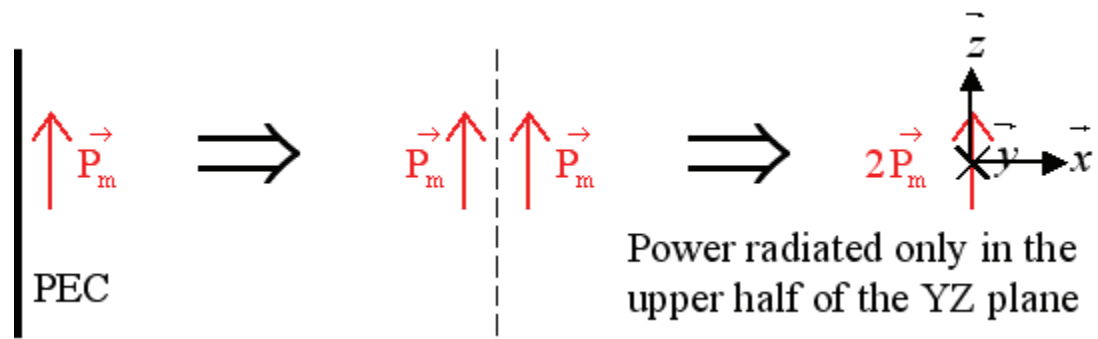
Figure 1.2. Radiation problem for the small aperture in Figure 1.1.

Figure 1.1(a) shows a partial view of a rectangular waveguide with a small aperture in its narrow wall. The propagating mode inside the waveguide is the dominant (TE_{10}) mode and the length of the waveguide is very small compared to the guide wavelength. The problem in Figure 1.1(a) can be expressed as a superposition of the two problems shown in Figures 1.1(b), 1.1(c). Hence the radiation problem in Figure 1.1(a) reduces to the one shown in Figure 1.2, where $\vec{x}$, $\vec{y}$, $\vec{z}$ are the unit vectors in the

Cartesian coordinate system. The magnetic polarization current ($\overrightarrow{P_m}$) in Figure 1.2 is given by Equation 1.1 *[Pozar]*. The equivalent magnetic current ($\overrightarrow{M}$) that is used to find the radiated fields is related to the magnetic polarization current as given by Equation 1.2 *[Pozar]*.

$$\overrightarrow{P_m} = -\alpha_m \overrightarrow{H}_{10}\delta(x)\delta(y)\delta(z) \qquad \textbf{(1.1)}$$

Where:

α_m is the magnetic polarizability of the small aperture in Figure 1.1(a)

$\overrightarrow{H}_{10}$ is the magnetic field intensity of the propagating TE$_{10}$ mode inside the waveguide

δ is the Dirac delta function

$$\overrightarrow{M} = 2j\omega\mu_o \overrightarrow{P_m} \qquad \textbf{(1.2)}$$

Where:

ω is the angular frequency of operation

μ_o is the permeability of free-space

The reason for the factor of two in Equation 1.2 is illustrated in Figure 1.2 and results from image theory.

Considering that the small aperture shown in Figure 1.1(a) is a narrow longitudinal slit, the magnetic polarizability (α_m) is given by Equation 1.3 *[Lee]*.

$$\alpha_m = \frac{\pi}{24}\frac{l^3}{\ln\left(\dfrac{4l}{w}\right)-1} \qquad \textbf{(1.3)}$$

Where:

λ is the free space wavelenth

l is the length of the slot and satisfies the condition: $l \ll \lambda$ \qquad **(1.3(a))**

w is the width of the slot and satisfies the condition: $w \ll l$ **(1.3(b))**

Hence the electric and magnetic fields and the power radiated in the far field of a small longitudinal-slot in the narrow wall of a rectangular waveguide with only the dominant TE$_{10}$ propagating inside are given as follows. The electric vector potential ($\vec{F}$) can be found from the magnetic current ($\vec{M}$); the radiated electric ($\vec{E}_r$) and magnetic ($\vec{H}_r$) fields in the far field can be found from $\vec{F}$; the power radiated in the far field ($\vec{P}_r$) can be found from $\vec{E}_r$, $\vec{H}_r$. *[Balanis]* The reference coordinate system used for these results is shown in Figure 1.2.

$$\vec{F} = -jF_z \cos\theta \frac{e^{-j\beta r}}{r}\vec{r} + jF_z \sin\theta \frac{e^{-j\beta r}}{r}\vec{\theta} \qquad (1.4)$$

Where:

$$F_z = \frac{\omega\varepsilon_o\mu_o}{48} \frac{l^3 A_{10}}{\ln\left(\frac{4l}{w}\right)-1}$$

A_{10} is the magnitude of $\vec{H}_{10}$

$\vec{r}$, $\vec{\theta}$, $\vec{\phi}$ are the unit vectors in the Spherical coordinate system

r, θ, ϕ are the spatial variables in the Spherical coordinate system

$$\vec{E}_r = \omega\eta_o F_z \sin\theta \frac{e^{-j\beta r}}{r}\vec{\phi} \qquad (1.5)$$

Where:

η_0 is the impedance of free space

$$\vec{H}_r = -j\omega\vec{F} \qquad (1.6)$$

$$\vec{P}_r = \frac{\pi}{6} \eta_o \left(\frac{\beta_o}{24} \frac{l^3 A_{10}}{\ln\left(\frac{4l}{w}\right) - 1} \right)^2 \qquad \textbf{(1.7)}$$

Where:

β_o is the free space wave number

1.2 <u>Longitudinal-slot in the narrow wall of a rectangular waveguide</u>

Although the analytical analysis of small apertures exists, there is very little discussion available in literature when the aperture dimensions are comparable to a wavelength and the slot width (w) is not negligible in comparison with the slot length (l). The analytical approach becomes intractable under this condition. The work in this section deals with the characterization of such slots in the narrow wall of a rectangular waveguide, using computational techniques; the cases for which 'w' is not negligible compared to 'l' are also included. The generic slot under consideration is shown in Figure 1.3.
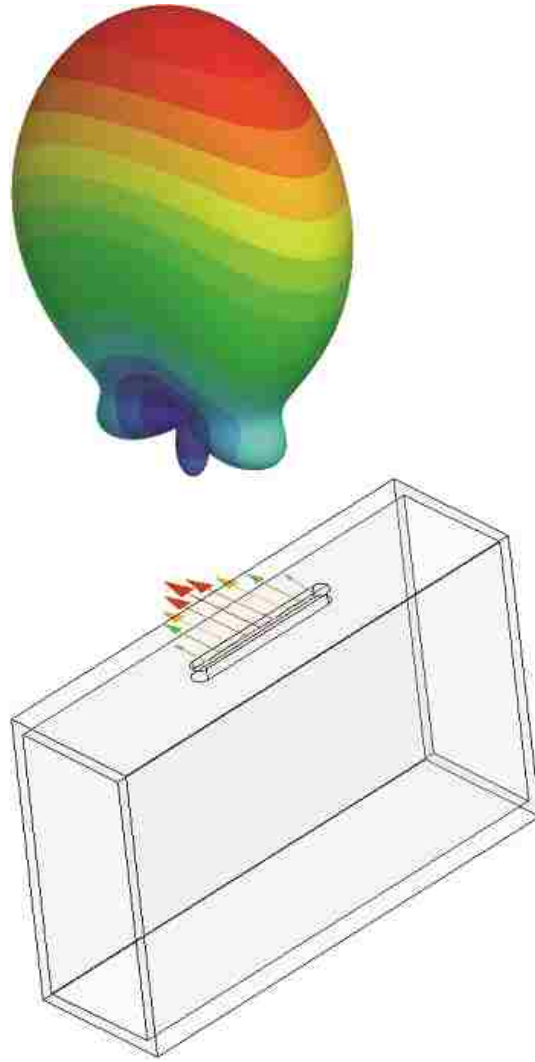
Figure 1.3. Narrow-wall longitudinal-slot along with its aperture E-field distribution and the 3-D radiation power pattern in absolute units.

The aim of this discussion is to generate intuition into the behavior of rectangular waveguide narrow-wall longitudinal-slots by presenting the extensive similarities they possess with a very well known antenna. In addition, new insights into the behavior of these slots can be achieved through the study of the relationships between the following parameters: the magnitude of the power radiated by the slot, vs., the magnitude / phase of the reflected / transmitted power through the waveguide, the phase of the power radiated

by the slot. The phase of the power radiated by the slot is proportional to the aperture phase at the center of the slot.

The computational analysis was performed with the aid of Ansoft Corporation's High Frequency Structure Simulator (HFSS). Full wave analysis using HFSS was performed for various values of lengths, widths of a rounded-rectangular shaped longitudinal-slot in the narrow wall of an X-band waveguide operating at 10GHz. Only part of this data was used in Chapter 3 for designing a narrow-wall longitudinal-slot array comprising of these slots due to the following reason. A half sine wave aperture E-field distribution is maintained only for certain slot dimensions, specifically for all possible widths as long as the length of the slot satisfied the condition in Equation 1.8.

$$l \leq \frac{\lambda}{2} \qquad \textbf{(1.8)}$$

The narrow-wall longitudinal-slot is first examined by comparing its properties to cylindrical wire antennas, where the width (length) of the slot is analogous to the diameter (length) of the wire. The characteristics of cylindrical wire antennas have been studied using the Integral Equation method and are presented in *[Kraus]*. Slot radiators that satisfy the condition in Equation 1.3(b) have been compared to thin wire antennas previously in *[Stevenson]*, *[Jasik]*, *[Lee]*; but the behavior of longitudinal-slots in the narrow wall of a rectangular waveguide that violate the conditions in Equations 1.3(a) and 1.3(b) has not been studied.

Figure 1.4 shows the resonant lengths associated with a thin wire antenna, specifically a center fed dipole of infinitesimal diameter. It can be seen that when the radiation resistance peaks, the input resistance at the antenna feed terminals goes to a very large value. From Figure 1.5 it can be seen that when the wire diameter is finite for a

monopole being fed over a ground plane the input impedance associated with a resonant

length is again very high but finite. Clearly, for a specific wire diameter there is a specific

length that produces resonance.
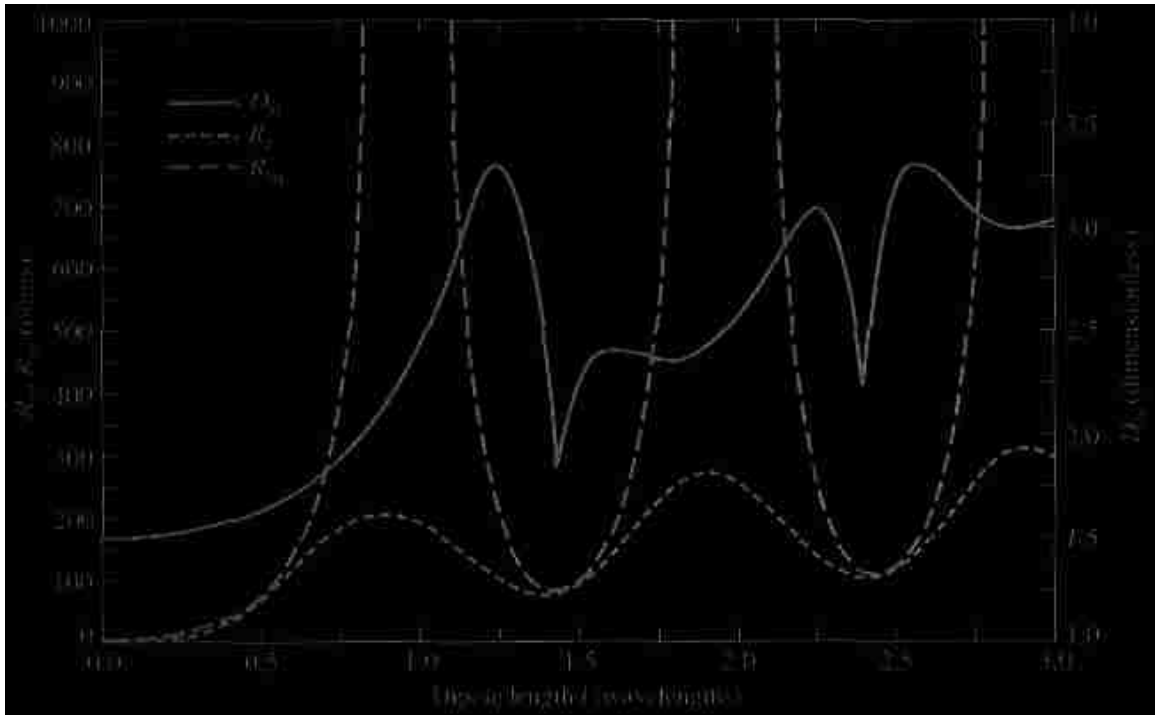
Figure 1.4. Relation between the radiation resistance (R$_r$), antenna input resistance (R$_{in}$) for an infinitesimally thin center fed dipole. "Excerpted from *[Balanis]*"
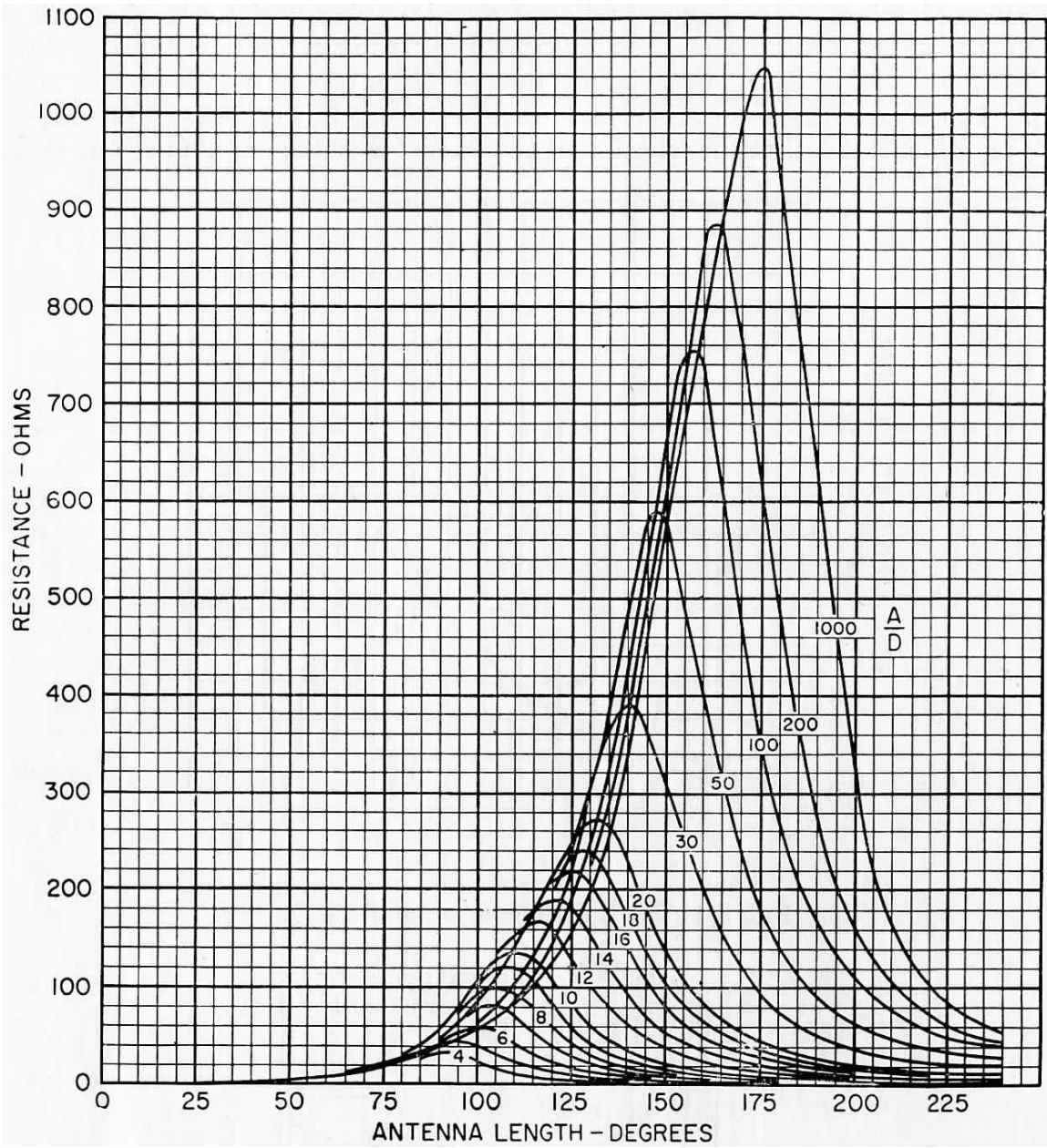
Figure 1.5. Resonances for a cylindrical monopole over a ground plane as indicated by the input resistance of the wire. Length of the wire=A. Diameter of the wire=D. "Excerpted from *[Jasik]*"
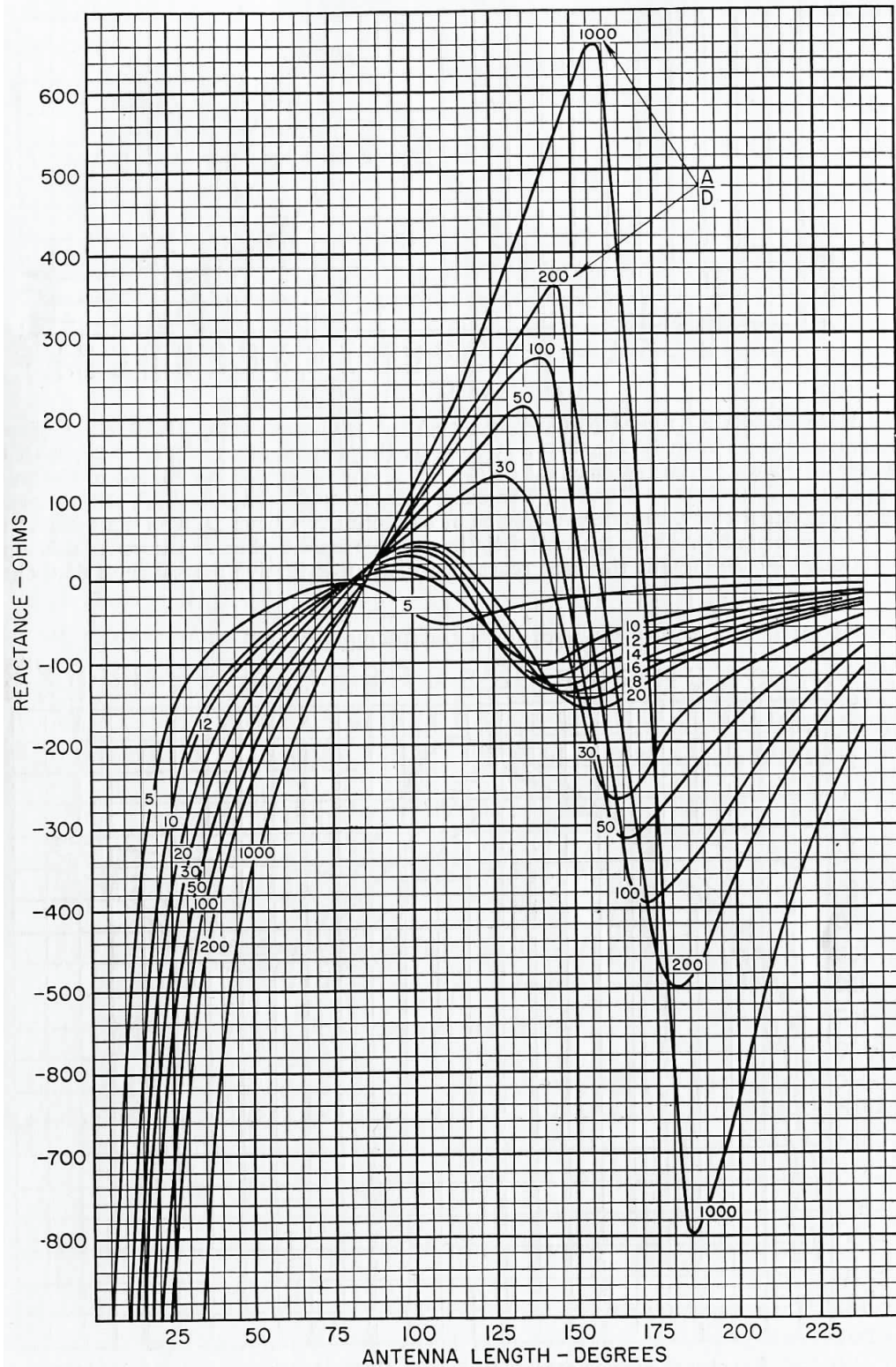
Figure 1.6. Resonance characteristics of a cylindrical monopole over a ground plane as indicated by the input reactance of the wire. Length of the wire=A. Diameter of the wire=D. "Excerpted from [Jasik]"

14

From Figures 1.5 and 1.6 it can also be deduced that a thinner wire has a higher quality factor, i.e. the resonances are sharper. Figures 1.7, 1.8 and 1.9 illustrate similar behavior but for the narrow-wall longitudinal-slot. For a specific width of the slot there is a specific length that produces resonance; and thinner the slot, sharper the resonance. The data in Figures 1.7 through 1.14 was collected from HFSS simulations for a rounded-rectangular shaped longitudinal-slot in the narrow wall of a rectangular X-band waveguide operating at 10GHz. Note that the free space wavelength at 10GHz is 30mm and the first resonance when the slot width is very small occurs approximately when the slot length is 15mm as shown in Figures 1.7 and 1.8. The curves in Figure 1.7 contain rapid fluctuations because the slot length-over-width ratios in the data used to obtain these curves were rounded off to the nearest integer.

Unlike the wire radiators, the dimensions of the waveguide also affect the resonances of slot radiators. For a wire radiator, as the diameter of the wire increases, the wire resonates at a shorter length. But for a narrow-wall longitudinal-slot, as the width of the slot increases, it can resonate for a longer or shorter length of the slot as shown in Figures 1.8 and 1.9 respectively, depending on the dimensions of the guide.

The dimensions of the waveguide used to obtain Figure 1.8 are the standard X-band waveguide dimensions; to obtain Figure 1.9, the broad dimension (a) of a standard X-band waveguide was changed from a=22.86mm to a=30mm. Note that even for the altered X-band waveguide, the propagating mode inside the guide is the dominant TE_{10} mode.

Consider a fixed operating frequency and the narrow dimension, b of the waveguide that is smaller than half the size of 'a'. Then the upper and lower limits of 'a',

such that only the dominant (TE$_{10}$) mode propagates inside the guide, are determined as follows. The lower (upper) limit on the broad dimension is found from the cut off frequency condition for the TE$_{10}$ (TE$_{20}$) mode shown in Equation 1.9 (1.10). The resulting limits on the broad dimension of the waveguide are shown in Equation 1.11.

$$f_{c10} = \frac{1}{2\pi\sqrt{\mu_o\varepsilon_o}}\frac{\pi}{a_1} \qquad\qquad \textbf{(1.9)}$$

Where:

a_1 is the lower limit on the broad dimension of the guide

μ_o is the permeability of free space

ε_o is the permittivity of free space

$$f_{c20} = \frac{1}{2\pi\sqrt{\mu_o\varepsilon_o}}\frac{2\pi}{a_2} \qquad\qquad \textbf{(1.10)}$$

Where:

a_2 is the upper limit on the broad dimension of the guide

The value of a_1 (a_2) is found by solving Equation 1.9 (1.10) after substituting 10GHz for the value of f_{c10} (f_{c20}).

$$15mm < a < 30mm \qquad\qquad \textbf{(1.11)}$$

Where:

a is the broad dimension of the waveguide

b is the narrow dimension of the waveguide and satisfies the condition $b \leq \dfrac{a}{2}$
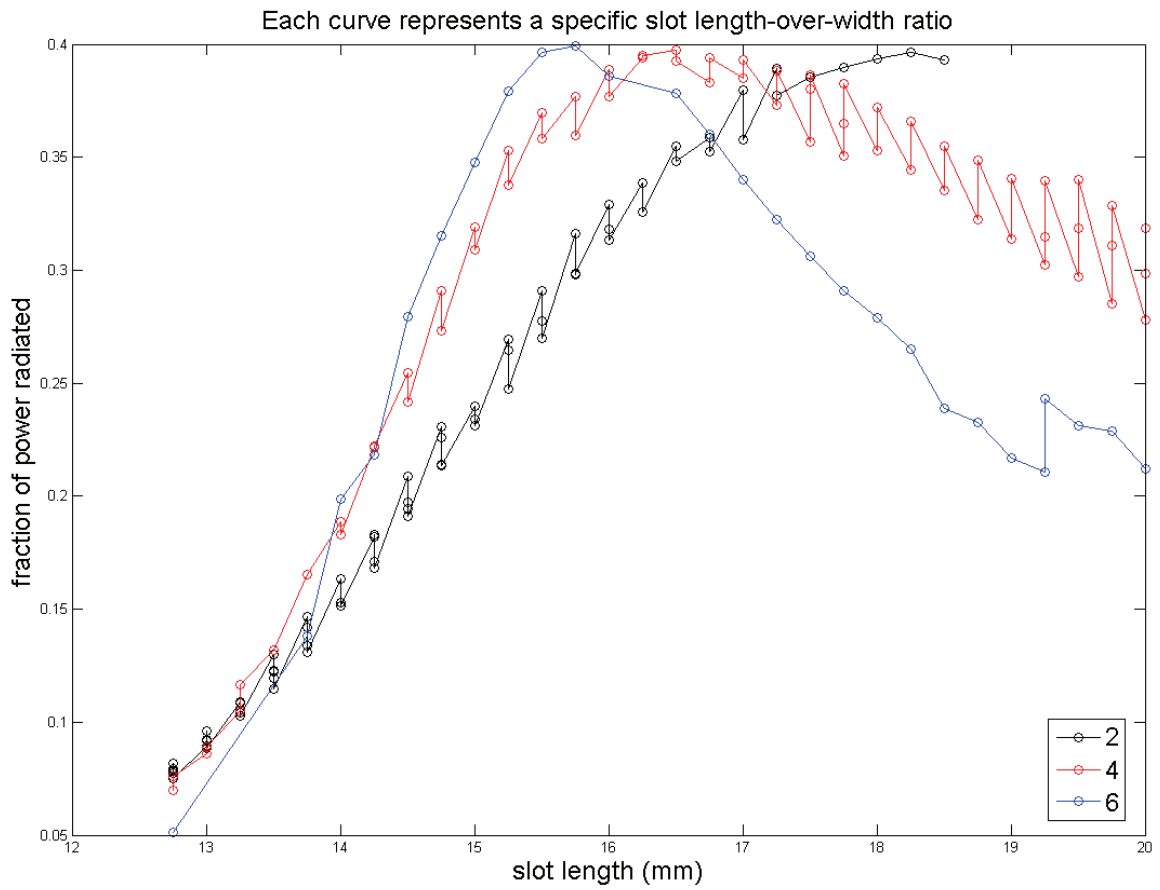
Figure 1.7. Resonances for a narrow-wall longitudinal-slot radiator. Each curve represents a specific slot length-over-width ratio.
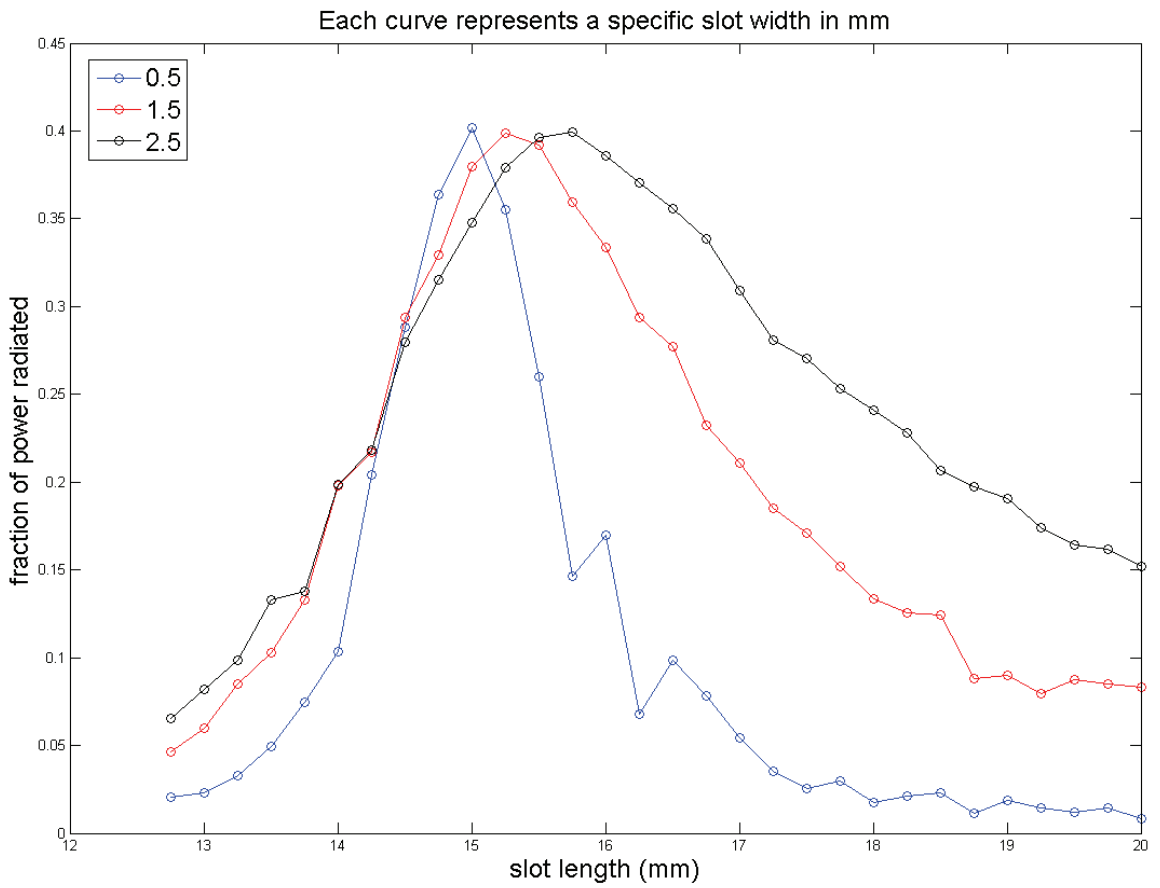
Figure 1.8. Resonances for a narrow-wall longitudinal-slot radiator. Each curve represents a specific slot width in mm.
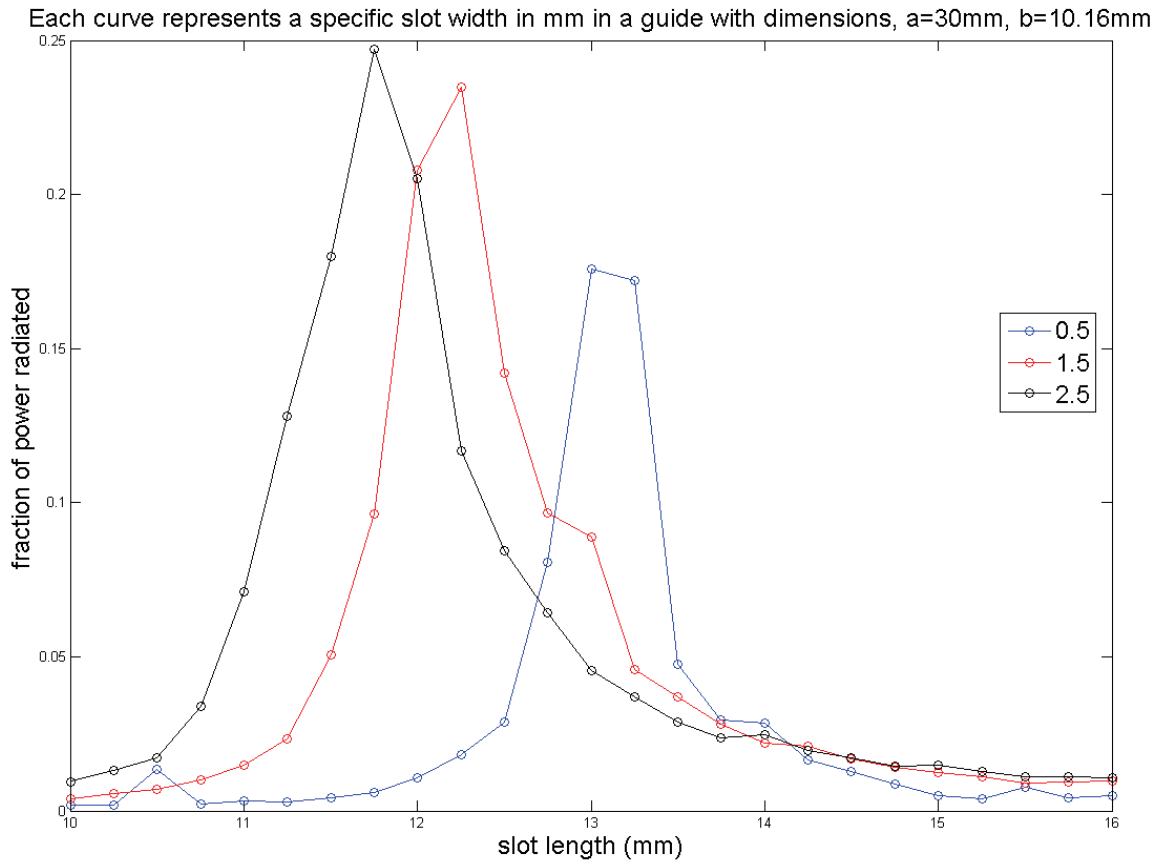
Figure 1.9. Resonances for a narrow-wall longitudinal-slot radiator in a waveguide with dimensions, a=30mm, b=10.16mm. Each curve represents a specific slot width in mm.

Figures 1.10 through 1.14 also show some interesting properties of a narrow-wall longitudinal-slot. They show that irrespective of the dimensions of the slot, the amplitude / phase of the power transmitted / reflected by the slot through the waveguide and the phase of the induced aperture E-field at the center of the slot have a predictable dependence on the amplitude of the power radiated through the slot. The phase of the transmitted (reflected) power through the waveguide is measured at the output (input) port of the waveguide containing the slot. All the sampled phases are measured relative to the phase of the input power, which is equal to zero at the input port. Figures 1.10

19

through 1.14 are obtained from two different data sets. For the first data set, the length of the waveguide containing the slot is two guide wavelengths long and the slot lengths (widths) ranged between 12.75mm (0.5mm) and 20mm (7.5mm). For the second data set, the length of the waveguide containing the slot is one guide wavelength long and the slot lengths (widths) ranged between 8.5mm (0.5mm) and 15mm (8mm). The reason for the 180° phase shift between the y-axes of the sub-plots in Figure 1.12 is due to the difference in the lengths of the waveguides used to obtain the two data sets.
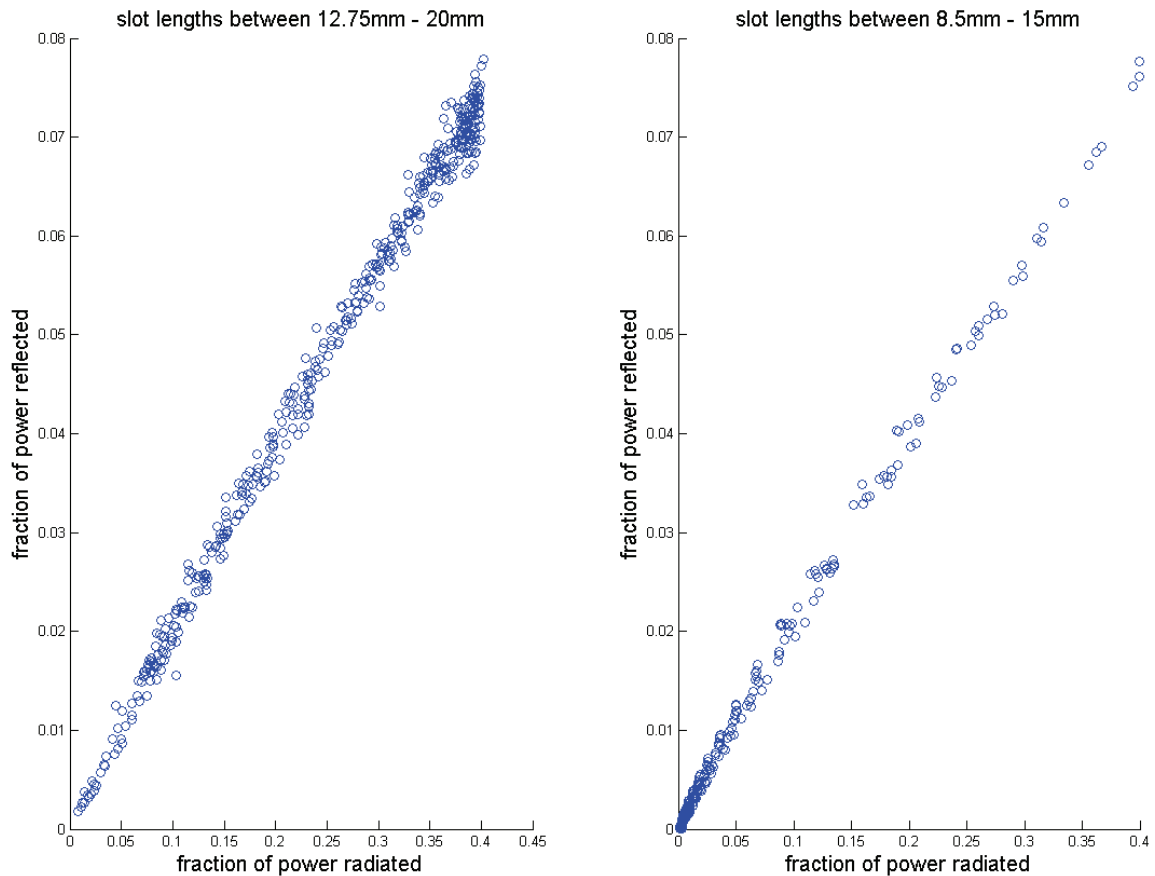
Figure 1.10. Relation between the amplitudes of the power radiated through the slot, power reflected through the waveguide for a narrow-wall longitudinal-slot.
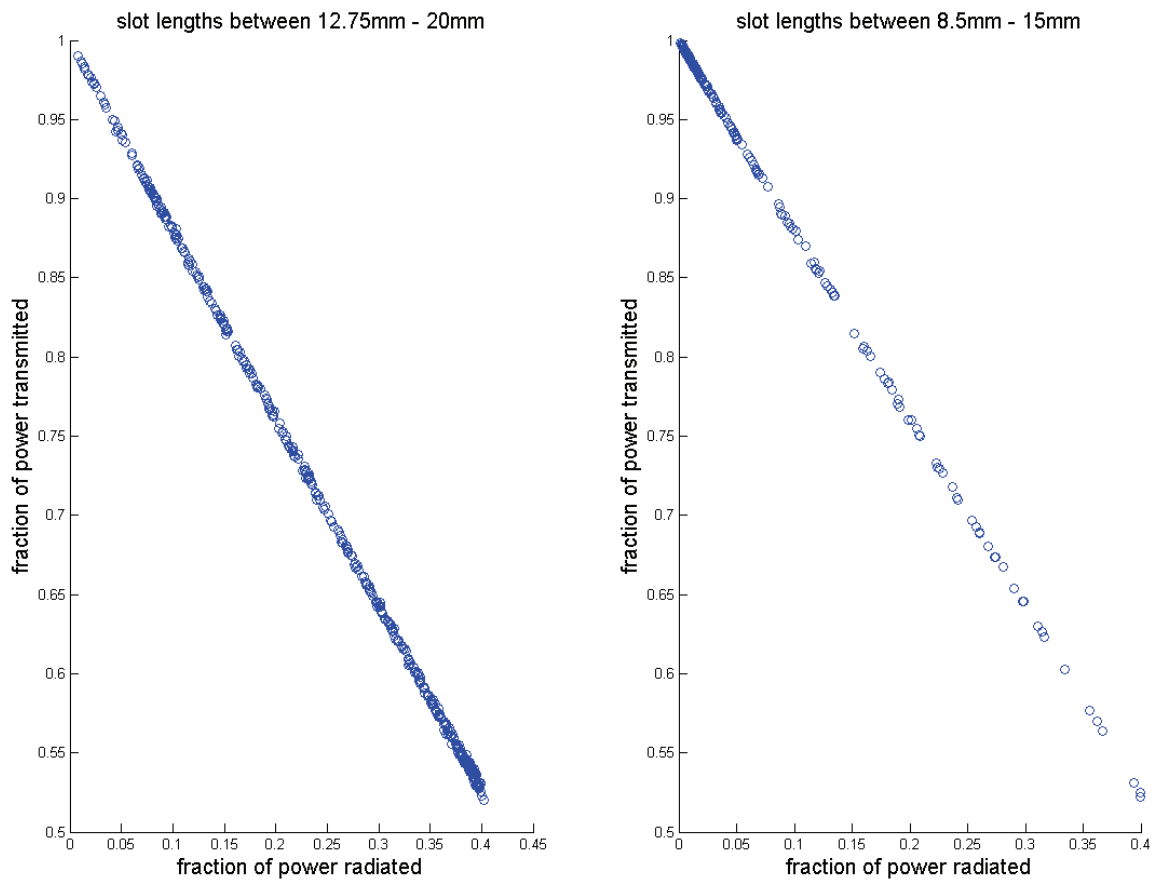
Figure 1.11. Relation between the amplitudes of the power radiated through the slot, power transmitted through the waveguide for a narrow-wall longitudinal-slot.
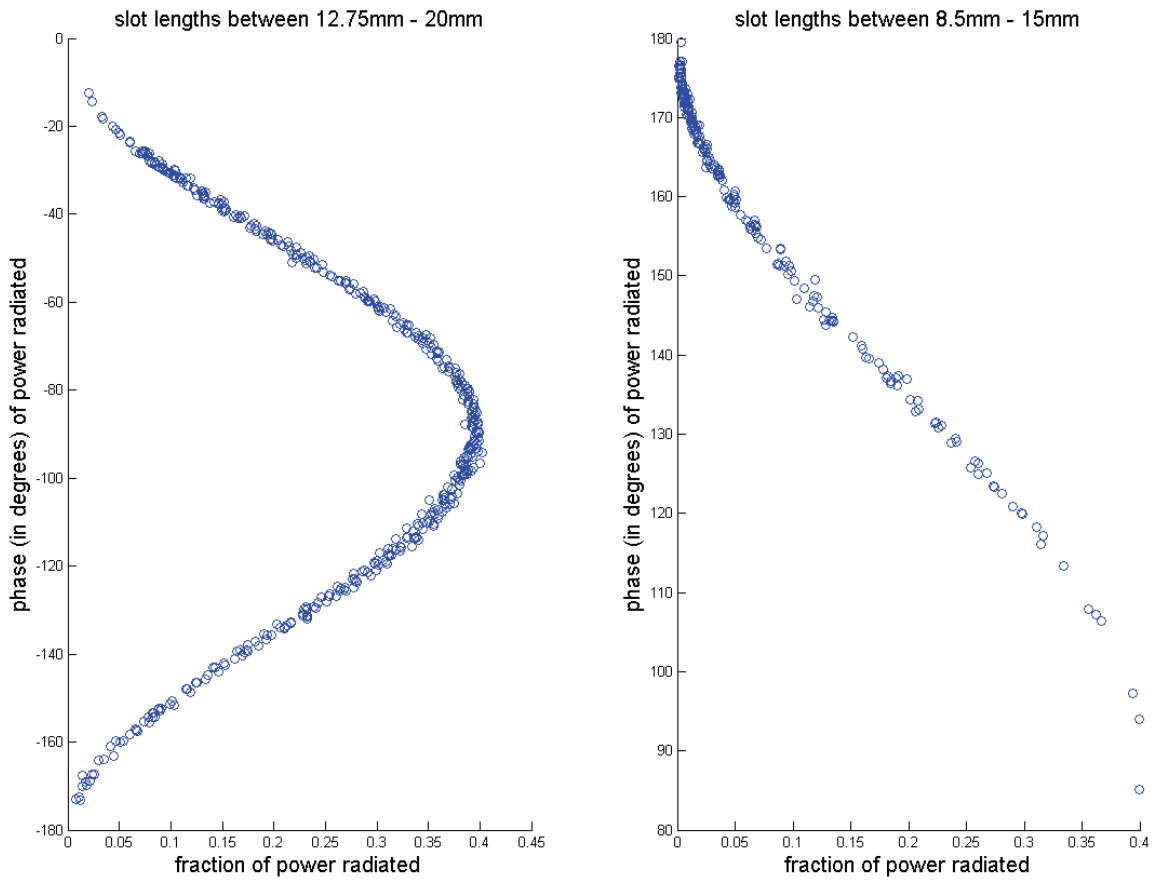
Figure 1.12. Relation between the amplitude of the power radiated through the slot, the phase of the induced aperture E-field at the center of the slot that is measured relative to the phase of the input power (= 0$^\text{o}$) at the waveguide's input port for a narrow-wall longitudinal-slot.

Figure 1.13. Relation between the amplitude of the power radiated through the slot, the phase of the power reflected through the waveguide that is measured relative to the phase of the input power (= 0°) at the waveguide's input port for a narrow-wall longitudinal-slot.
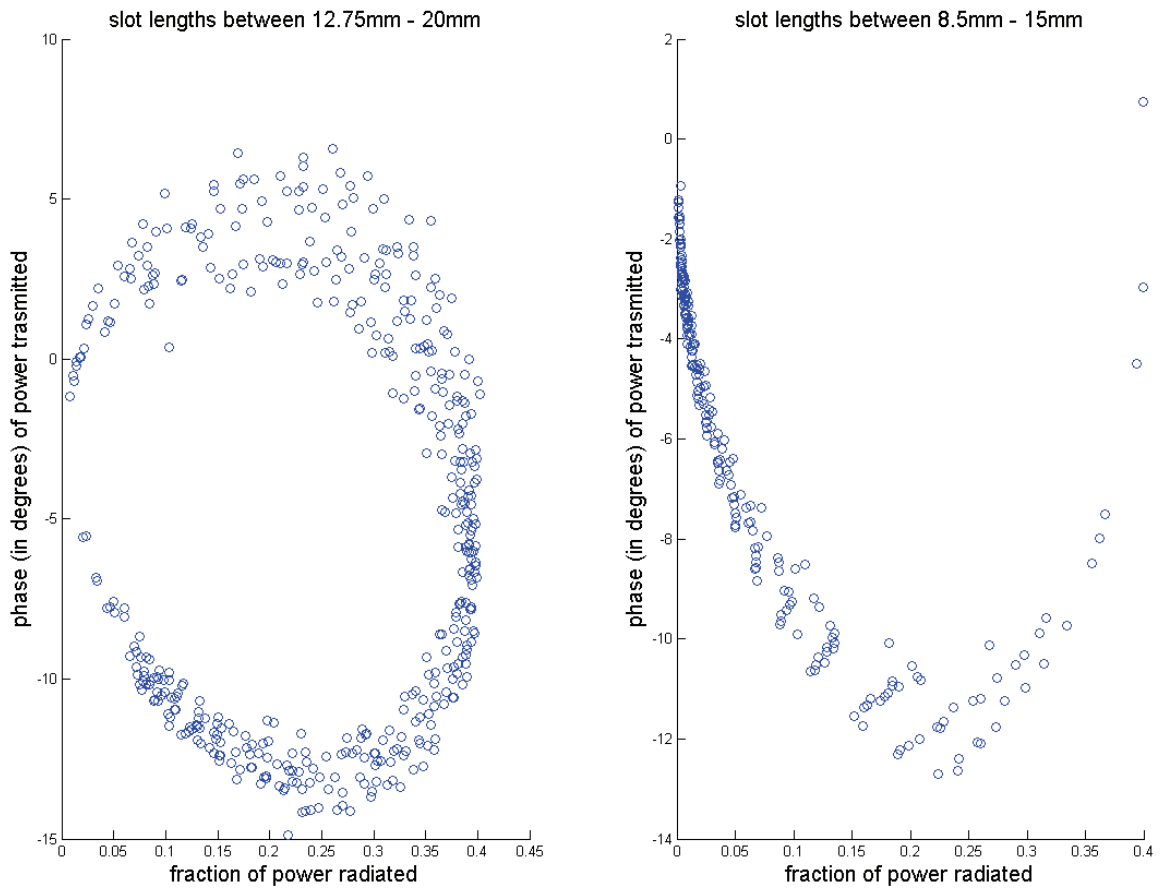
Figure 1.14. Relation between the amplitude of the power radiated through the slot, the phase of the power transmitted through the waveguide that is measured relative to the phase of the input power ($= 0^o$) at the waveguide's input port for a narrow-wall longitudinal-slot.

2. H-PLANE-BEND-RADIATOR

The H-plane-bend-radiator (HPB-radiator) is an H-plane bend terminating in a radiating aperture with the narrow dimension of the waveguide flaring out to the maximum possible width; the maximum possible width is the same as the maximum dimension for the narrow wall of a rectangular waveguide that still only supports the dominant (TE_{10}) mode. Figure 2.1(a) (2.1(b)) is a schematic of the HPB-radiator element to be used in the narrow-wall-slot-HPB-array (split-waveguide-HPB-array) described in Chapter 3 (4). The design variables for the HPB-radiator are its aperture dimensions and the function that determines the H-plane taper. The optimal HPB-radiator element has the same half sine wave aperture E-field distribution as a narrow-wall longitudinal-slot with minimal reflected power into the feed-waveguide.
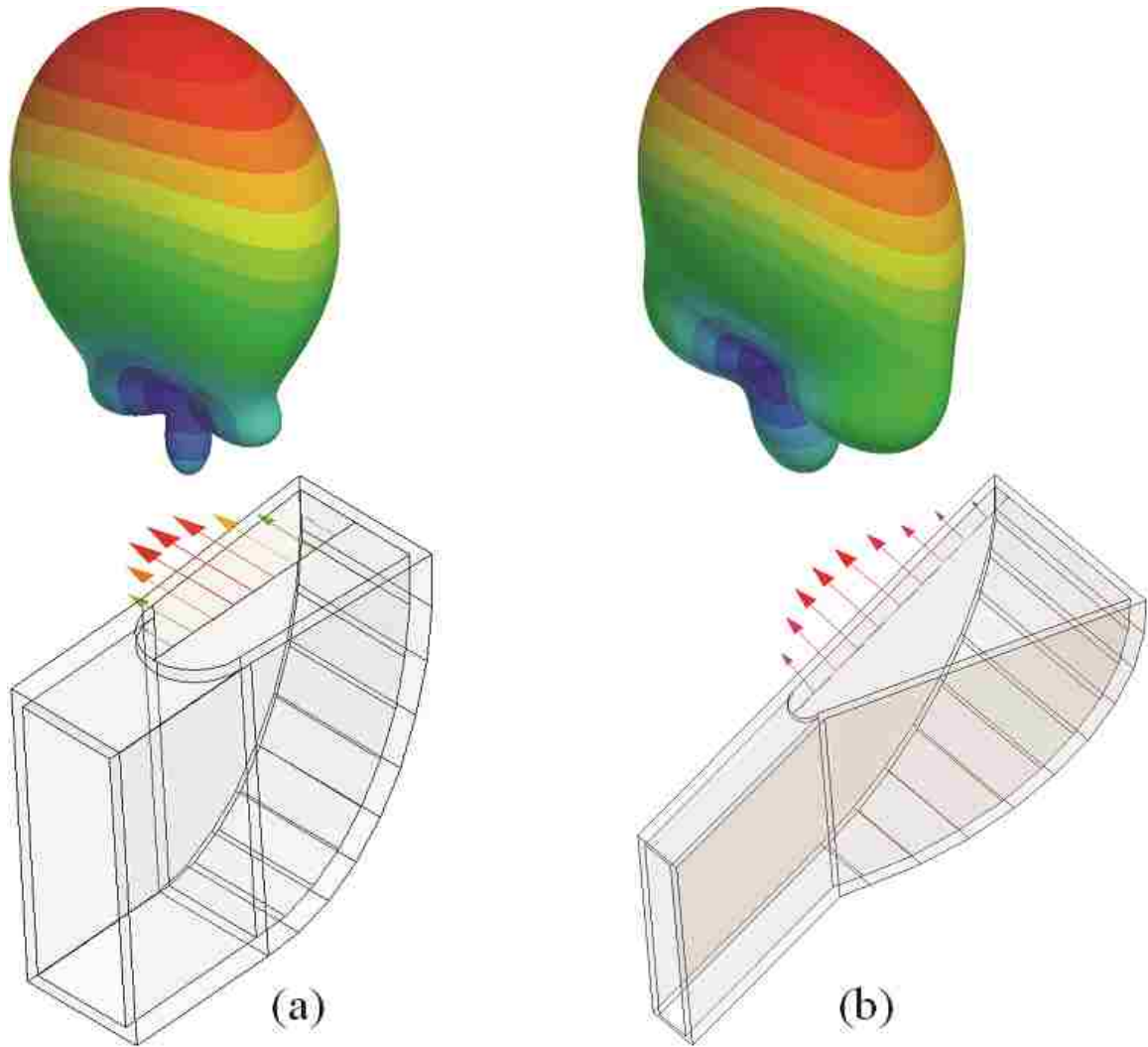
Figure 2.1. (a) Narrow-wall-slot-HPB-array's HPB-radiator element along with its aperture E-field distribution and the 3-D radiation power pattern in absolute units. (b) Split-waveguide-HPB-array's HPB-radiator element along with its aperture E-field distribution and the 3-D radiation power pattern in absolute units.

The HPB-radiator elements used for both the narrow-wall-slot-HPB-array and the split-waveguide-HPB-array are designed for minimum power reflected into the feed-waveguide for the following reasons.

It will be seen in Chapter 4 that the split-waveguide-HPB-array has beam steering

capability by the virtue of its split-waveguide input. A phase shifter can be placed at each of the split-inputs and use a single high power microwave source. When the elements of the array do not have minimum power reflected into the feed-waveguide, coupling between the elements can occur through the split-inputs at the output of the microwave source. This would disrupt the beam steering functionality of the array. It is important for the elements of the split-waveguide-HPB-array to have minimum power reflected to also protect the microwave source.

It will be seen in Chapter 3 that the narrow-wall-slot-HPB-array is designed by optimizing the mutual coupling through the waveguide between its array elements. From Chapter 1, it was seen that the power radiated by a narrow-wall longitudinal-slot is directly proportional to the power reflected by it into the feed waveguide. But nevertheless this power reflected can contribute adversely to the radiation pattern of the array, although the total power reflected at the array input can be minimized through mutual coupling analysis described in Chapter 3. This can be explained as follows.

When there is a good possibility that the radiation pattern of the array to be designed would have its main lobe canted from the broadside direction and the design goal is to maximize the directivity, it is advantageous to have power flow in only one direction along the length of the linear array. So it is important for the HPB-radiator element of the narrow-wall-slot-HPB-array also to be designed for minimum reflected power at its input.

The design of the HPB-radiator was initiated in HFSS; simulations were performed with no narrow-wall flare, for an aperture length of a half free space wavelength and for the function that defines the H-plane taper determined by the location

27

of a single point (HPB-radiator-1-point-optimization). Unlike the HPB-radiators shown in Figures 2.1(a) and 2.1(b), for the purpose of HPB-radiator-1-point-optimization, the aperture of the HPB-radiator begins at the same location along the length of the waveguide where the H-plane taper begins. This can be seen in Figure 2.2(a). Figure 2.2(a) shows a two dimensional view of the HPB-radiator with the narrow dimension of the waveguide as the missing dimension. The waveguide used was again a standard X-band guide operating at 10GHz. The data from these simulations, i.e. the point locations in the search-space (as illustrated in Figure 2.2(a)) versus the power reflected, forms the computational data to be analyzed. The details of this analysis are discussed in Section 2.1. Figure 2.2(b) is a surface plot of the amplitude of the power reflected into the feed-waveguide for the various simulation points in the search-space shown in Figure 2.2(a).
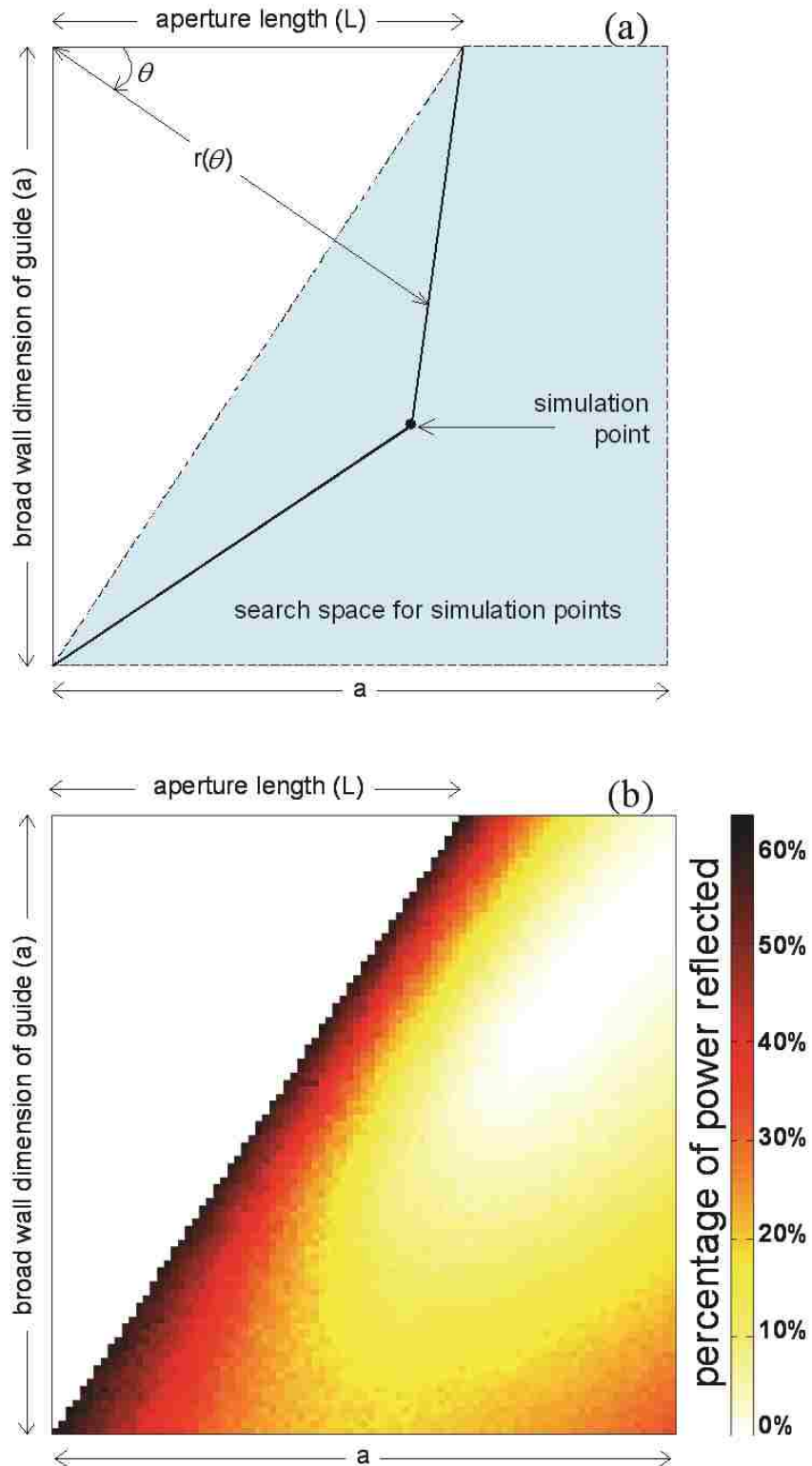
Figure 2.2. (a) Illustration of the HPB-radiator in two dimensions, showing the search-space for HPB-radiator-1-point-optimization. (b) Surface plot showing the power reflected amplitudes for points in the search-space shown in Figure 2.2(a).

29

2.1 HPB-radiator design procedure using dimensional offset hypothesis

Since the HPB-radiator will be part of a high power antenna, it is important that its final design have a smooth H-plane taper function containing no sharp corners. The following discussion proposes a design procedure for the HPB-radiator element's H-plane taper function for a given aperture length.

The design of the HPB-radiator element with a smooth H-plane taper function using just analytical or computational electromagnetics techniques felt intractable and the following novel design approach that processes the computational analysis (HPB-radiator-1-point-optimization) data using iterative search algorithms is proposed. These search algorithms were developed to utilize user-defined design criteria that can be adjusted according to the information available from the computational analysis data regarding the structure to be designed. The approach is based on the following hypothesis (called the dimensional offset hypothesis): for a fixed aperture length, the power reflected due to any taper function has a predictable dependence on the dimensional offset between the given taper function and the ideal-taper-function. The ideal-taper-function for a given aperture length produces the lowest reflected power and is represented by the black curve in Figure 2.3. The shaded region that is represented by the dotted lines in Figure 2.3 represents the dimensional offset.
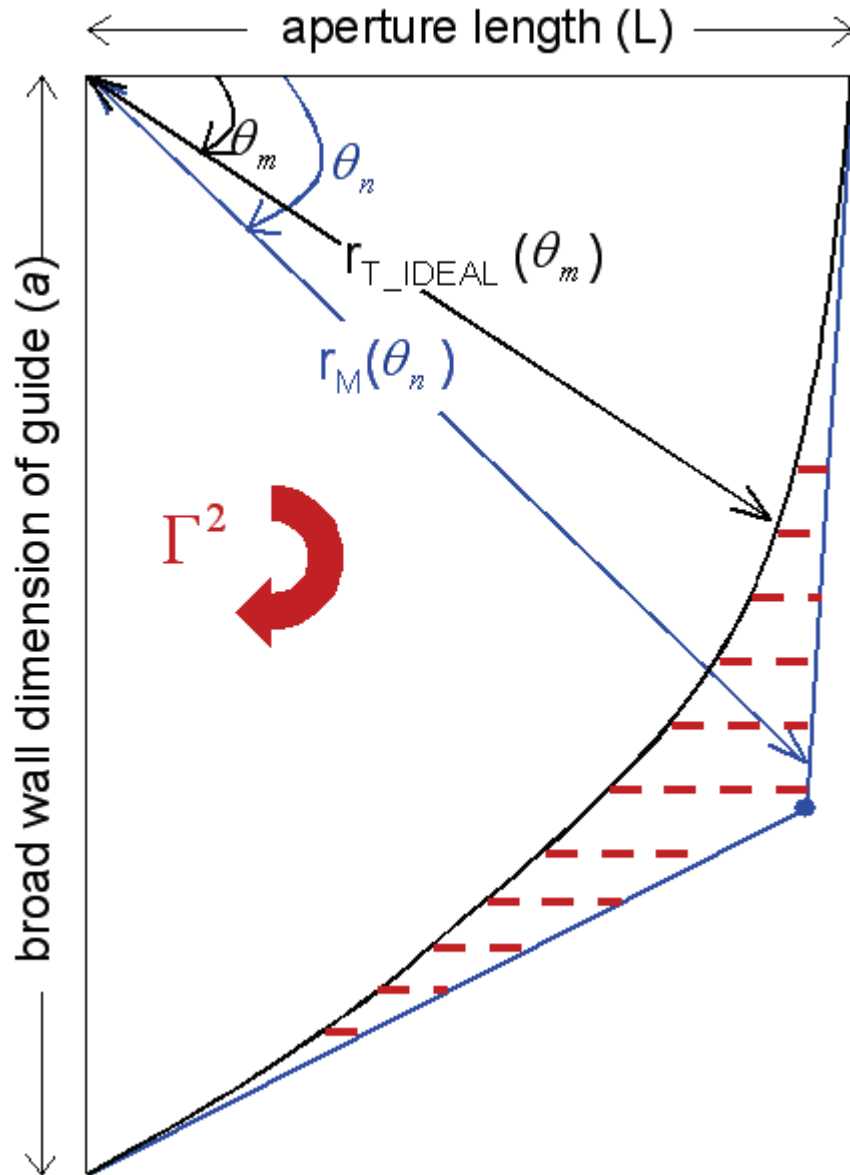
Figure 2.3. Illustration for the dimensional offset hypothesis.

To find the ideal-taper-function, the dimensional offset hypothesis is proposed to be implemented as follows. The dimensional offset is characterized by the dimensional offset parameter, p as defined in Equation 2.1. The H-plane taper functions obtained from HPB-radiator-1-point-optimization are labeled as 'measured-taper-functions'; therefore the power reflected into the feed-waveguide by an HPB-radiator constructed using a

measured-taper-function is known. The 'test-taper-functions' are used to eventually lead to the ideal-taper-function. The search-space for the test-taper-functions is discretized as shown in Figure 2.4(a) and each possible combination of points in the discretized space leads to a test-taper-function. A test-taper-function formed by a combination of points is as shown in Figure 2.4(a).

$$p = \sum_{n=2}^{N} p_n \Delta\theta_n \qquad (2.1)$$

Where:

$p_n = |r_M(\theta_n) - r_T(\theta_n)| w(\theta_n)$

$r_M(\theta_n)$ is the radius of a 'measured-taper-function' at an angle of θ_n as shown in Figure 2.3

$r_T(\theta_n)$ is the radius of a 'test-taper-function' at an angle of θ_n

$w(\theta_n)$ is a user defined weight function at an angle of θ_n

$\Delta\theta_n = \theta_n - \theta_{n-1}$

$\Delta\theta_n \leq 1°$

From Figure 2.3: $\theta_1 = 0°$ and $\theta_N = 90°$
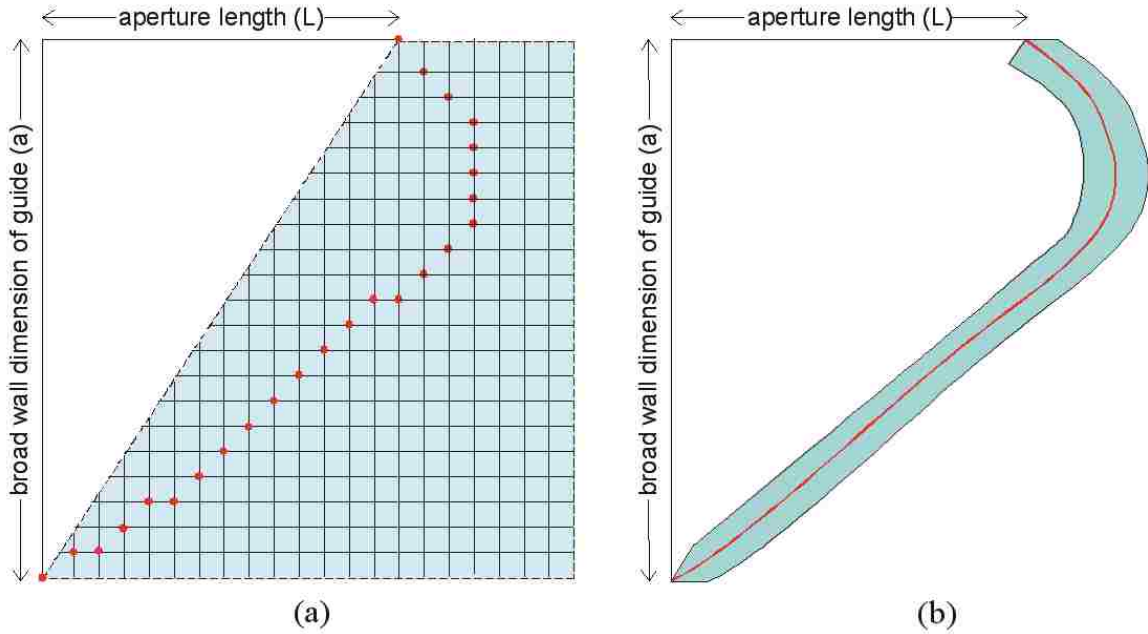
Figure 2.4. Search-space (shown in blue/green) for test-taper-functions (shown in red).

Consider, for instance, that there are one hundred measured-taper-functions and since for each measured-taper-function there is a corresponding reflected power measurement, there are one hundred corresponding reflected power measurements. Now consider a test-taper-function; from Equation 2.1 there would be one hundred dimensional offset parameter values corresponding to the test-taper-function. To implement the dimensional offset hypothesis, a scatter plot is made between the above mentioned reflected power values and dimensional offset parameter values. If the dimensional offset hypothesis does have any merit, then the test-taper-function that produces the scatter plot with the least scatter is the ideal-taper-function. It can be seen that the scatter plot in Figure 2.5(a) has a higher scatter/fit-error compared to the scatter plot in Figure 2.5(b); hence the test-taper-function used to obtain Figure 2.5(b) is a better test-taper-function.

(a) Test-taper-function with higher fit-error

Γ^2 values of measured-taper-functions

normalized dimensional offset parameter (*p*) values

(b) Test-taper-function with lower fit-error

Γ^2 values of measured-taper-functions

normalized dimensional offset parameter (*p*) values
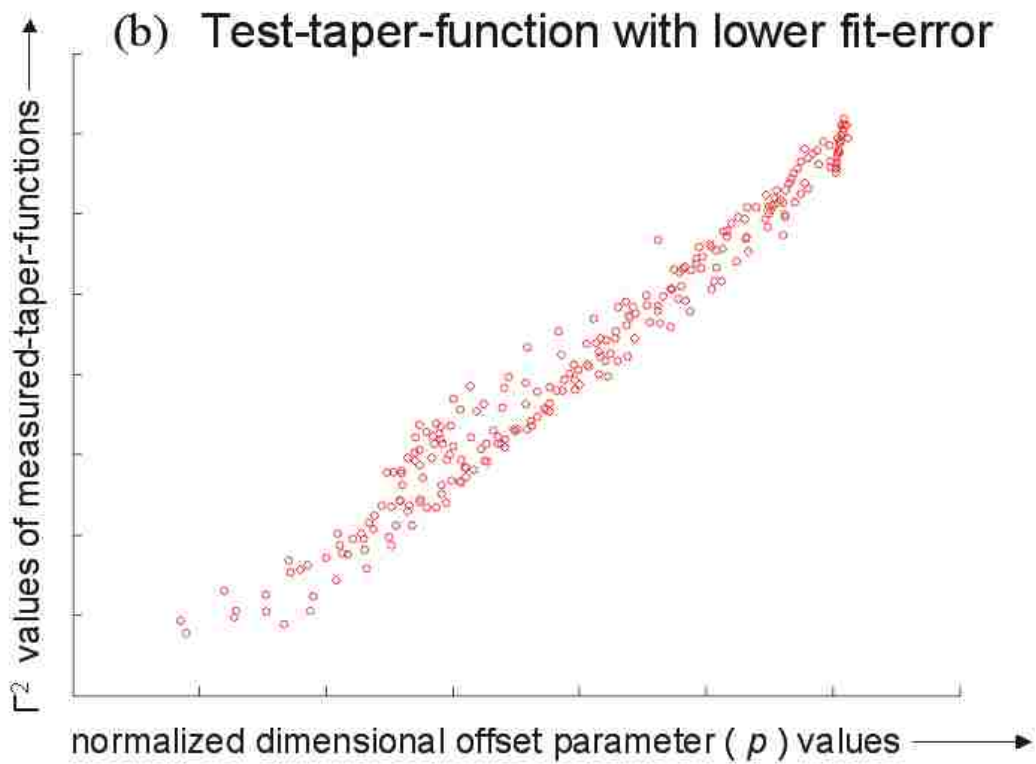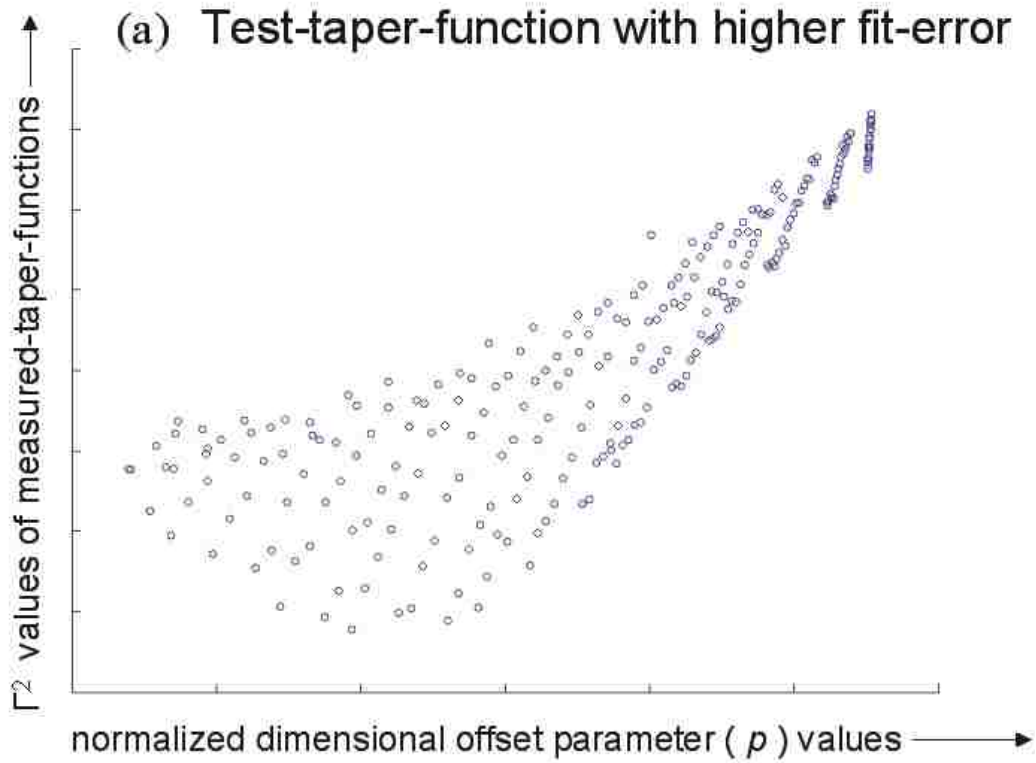
Figure 2.5. (a) Sample scatter plot with higher scatter/fit-error. (b) Sample scatter plot with lower scatter/fit-error.

34

To make the search for the ideal-taper-function efficient, the test-taper-functions can be iterated in two stages. The first stage is shown in Figure 2.4(a), where the grid used to obtain the set of points that make a certain test-taper-function, is coarse. After obtaining the best test-taper-function given the coarse grid, the search-space around this best test-taper-function is used as the new search-space as shown in Figure 2.4(b). The search-space in Figure 2.4(b) is discretized more finely than that in Figure 2.4(a) leading to the ideal-taper-function. The coarseness of the grid in Figures 2.4(a) and 2.4(b) is dependent upon the number of iterations that can be handled by the computational resources available. Hence for a given search-space discretization, the best test-taper-function becomes the ideal-taper-function.

To summarize, the search for the optimal HPB-radiator's ideal-taper-function is made possible by mapping the power reflected by a taper function (variable-1) to the corresponding scatter plot's fit-error (variable-2). Since the computational time required to find variable-2 is much lower compared to variable-1, it is possible to find the dimensional offset parameters and the scatter plots' fit-errors corresponding to the various test-taper-functions and these iterations eventually lead to the ideal-taper-function.

The aim of the following discussion is to illustrate that the dimensional offset hypothesis has the potential to be used as a procedure for designing the HPB-radiator, although the calculation of the dimensional offset parameter and the procedure for determining the amount of scatter in the scatter plots mentioned above has room for improvement. It is also hypothesized that it is reasonable to make the dimensional offset

hypothesis while designing other kinds of structures as long as the dimensional offset parameter's calculation and the scatter plots' analysis is appropriately performed.

The demonstration of the dimensional offset hypothesis' merit is performed in two steps that were implemented in a program coded in MATLAB (Matrix Laboratory). In the first step, the various test-taper-functions are described by Equation 2.2 and are labeled as 'spiral-taper-functions'. The best test-taper-function from the first step is a spiral-taper-function with n=1; it is used in the second step for determining the test-taper-functions as described by Equation 2.3 that are labeled as 'spiral-sine-taper-functions'. Figure 2.6 (2.7) shows the extent of variation for the test-taper-functions in step one (two) and the best test-taper-function obtained from this step is given by the red curve. The weight function given in Equation 2.1 is chosen to be equal to unity for the entirety of this analysis. Also, to characterize the amount of scatter in the scatter plots, the following procedure is undertaken. First the data in each scatter plot is fitted to a first order polynomial. Then the fit-error for each of the scatter plots is obtained by taking the sum of the absolute values of the differences between the y-coordinates of the scattered points and the corresponding y-coordinates of the points on the fitted polynomial. The y-axis of the scatter plots corresponds to the reflected power measurements of the measured-taper-functions. So the fit-error of a certain scatter plot is used to characterize the amount of scatter in it; a higher fit-error corresponds to a higher amount of scatter.

$$r(\theta) = \frac{a - L}{(\pi/2)^n} \theta^n + L \qquad (2.2)$$

Where:

$0° \leq \theta \leq 90°$

$0.6 \leq n \leq 4$

a, L, θ, $r(\theta)$ are shown in Figure 2.6
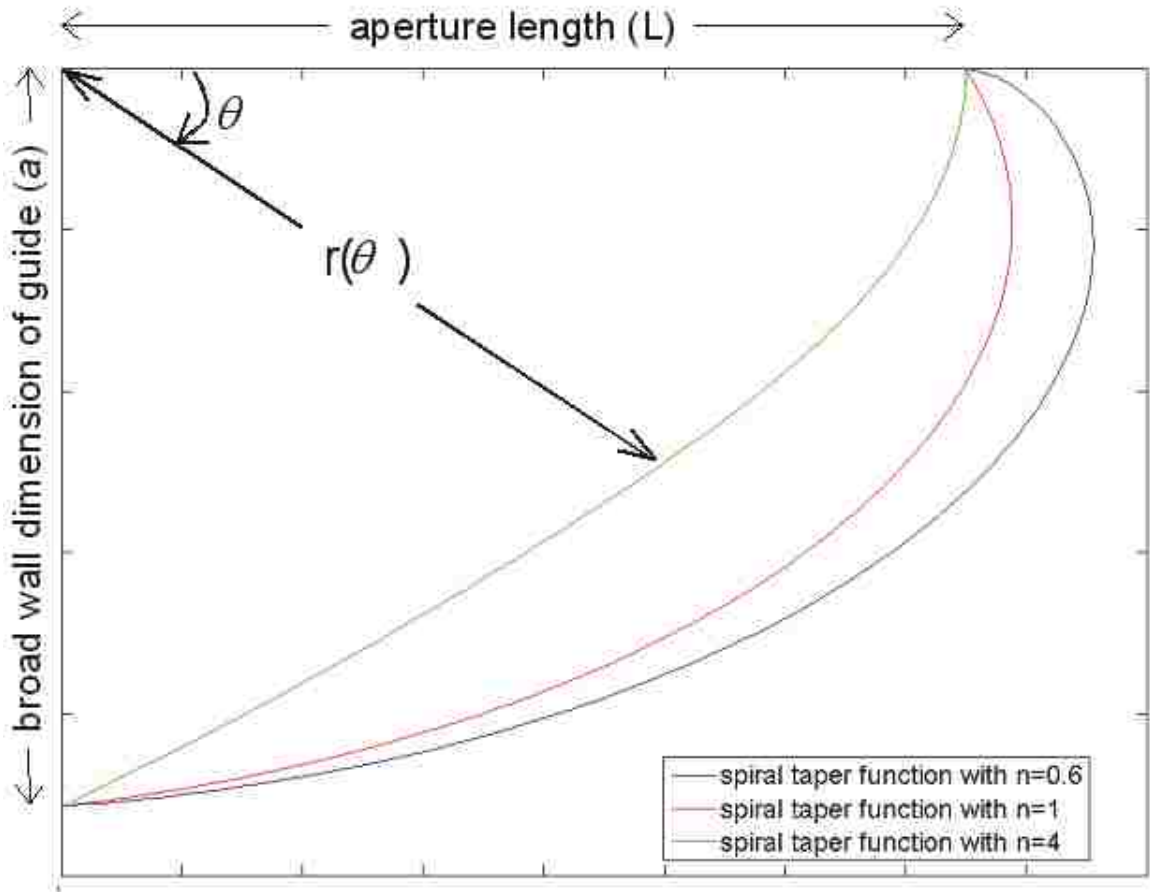
Figure 2.6. Spiral-taper-functions used for testing hypothesis.

$$r(\theta) = \frac{a - L}{\pi/2}\theta + L + (\text{sine\_amp})\sin(\frac{2\pi\theta}{\pi/2}) \qquad (2.3)$$

Where:

$0° \leq \theta \leq 90°$

$0.1 \leq \text{sine\_amp} \leq 4$

a, L, θ, $r(\theta)$ are shown in Figure 2.7
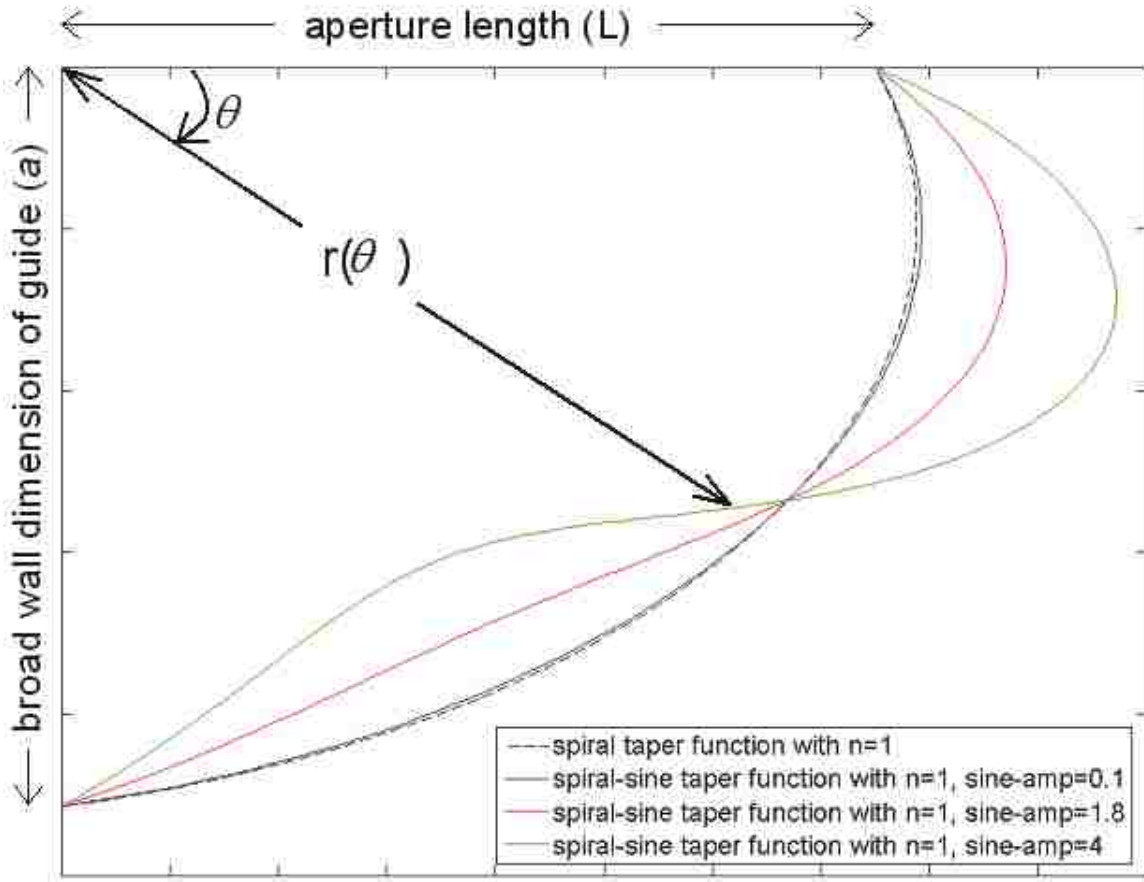
Figure 2.7. Spiral-sine-taper-functions used for testing hypothesis.

Figures 2.8 and 2.9 demonstrate the merit of dimensional offset hypothesis. Each scatter point in Figure 2.8 (2.9) corresponds to a test-taper-function that was obtained from Equation 2.2 (2.3). HFSS was used to find the reflected power from each of the test-taper-functions defined by Equations 2.2 and 2.3. Figures 2.8 and 2.9 confirm that a lower fit-error actually corresponds to a lower reflected power for a test-taper-function.
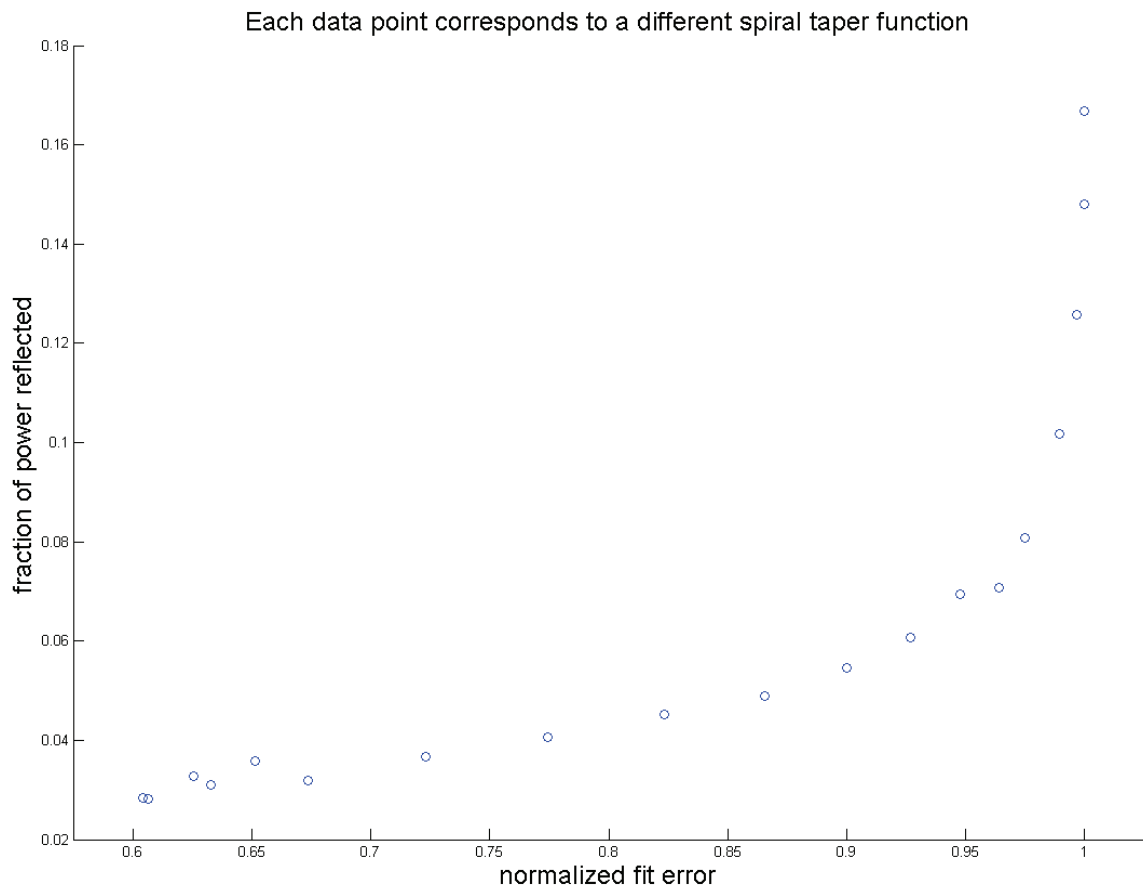
Figure 2.8. Hypothesis verification for spiral-taper-functions.
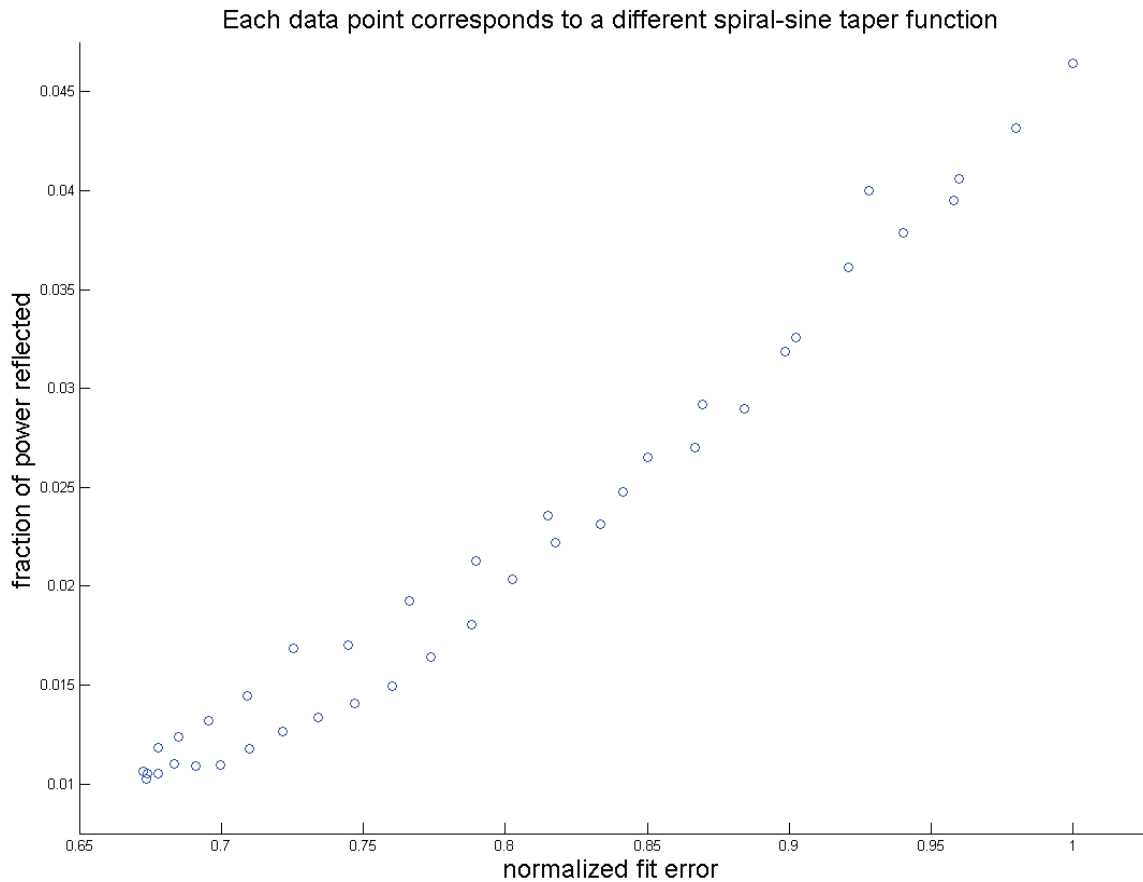
Figure 2.9. Hypothesis verification for spiral-sine-taper-functions.

2.2 HPB-radiator elements used in the narrow-wall-slot-HPB-array and the split-waveguide-HPB-array

The HPB-radiator element, which is used as the last element in the narrow-wall-slot-HPB-array, is shown in Figure 2.1(a). It can be inferred from Chapter 3 that not only does the power reflected into the feed-waveguide by the HPB-radiator element needs to be low but also its aperture phase plays an important role in the performance of the narrow-wall-slot-HPB-array. The aperture phase is the phase of the aperture E-field at the center of the aperture with reference to the phase of the input power (=0°) at the input

port of the element. The aperture length of the HPB-radiator greatly influences its aperture phase value that complements the narrow-wall-slot-HPB-array's performance; more specifically an aperture length slightly greater than a half free space wavelength was found to be more suitable.

With respect to the HPB-radiator analysis in Section 2.1, the aperture of the HPB-radiator began at the same location along the length of the waveguide where the H-plane taper began, as shown in Figure 2.2; the length of the radiating aperture of the HPB-radiator was chosen to be a half free space wavelength for the following reasons. An aperture length greater than a half free space wavelength produced an aperture E-field that is not necessarily a half sine wave distribution for different taper functions, and an aperture length less than a half free space wavelength produced a higher reflected power into the feed-waveguide.

The design of the HPB-radiator element is therefore a best compromise between: the reflected power into feeding waveguide, the aperture E-field distribution and the aperture phase. This was achieved for the design shown in Figure 2.1(a). The aperture of the HPB-radiator begins at a location along the length of the waveguide that is approximately 4mm before the beginning of the H-plane taper, and the length of the aperture is approximately 19mm, where 15mm corresponds to a half free space wavelength at 10GHz. The taper function used for the HPB-radiator in Figure 2.1(a) is defined by the equation of an ellipse. For this best compromise design: the power reflected into the feed-waveguide is less than 1%, with an approximately half sine wave aperture E-field distribution. The aperture phase also complements the performance of the narrow-wall-slot-HPB-array as will be shown in Chapter 3.

The HPB-radiator element, which is used as the standard element in the split-waveguide-HPB-array, is shown in Figure 2.1(b). The aperture of the HPB-radiator begins at a location along the length of the waveguide that is approximately 2.6mm before the beginning of the H-plane taper, and the length of the aperture is approximately 17.6mm, where 15mm corresponds to a half free space wavelength at 10GHz. The taper function used for the HPB-radiator in Figure 2.1(b) is defined by the equation of an ellipse. The power reflected into the feed-waveguide for the design is less than 1%, with an approximately half sine wave aperture E-field distribution as shown in Figure 2.1(b).

3. NARROW-WALL LONGITUDINAL-SLOT ARRAY WITH HPB-RADIATOR

An illustration of the narrow-wall longitudinal-slot array with an HPB-radiator element (narrow-wall-slot-HPB-array) is shown in Figure 3.1; the center-to-center distance between any two adjacent array elements is the same. For a rectangular waveguide in the dominant (TE_{10}) mode of operation, not only the tangential but also the normal component of the E-field at its narrow wall is zero. Therefore, the narrow-wall-slot-HPB-array can handle high powers. The design criteria for the narrow-wall-slot-HPB-array are to maximize the peak directivity of its fan beam radiation pattern and to minimize the reflected power into its feed-waveguide. The design variables are the slots' dimensions, spacing between the elements and the narrow-wall taper. The narrow wall of the waveguide can be squeezed to increase the power radiated by a slot. The last element of the array, i.e. the HPB-radiator, has been described in Chapter 2. As mentioned in Chapter 1, the dimensions of the slots considered in the array's design satisfied the condition given by Equation 1.8. Under this condition, all variations of the slot dimensions produced a very similar half sine wave aperture E-field distribution. To maximize the peak directivity of the array, the elements of the array are to radiate equal powers and have a progressive phase shift, i.e. the design is to produce a uniform linear array. To minimize the power reflected into the feed-waveguide, the power reflected from the individual elements need to destructively interfere. The optimal narrow-wall-slot-HPB-array design is a best compromise between the powers radiated by the elements, the progressive phase shift between the elements and the reflected power at the input of the array.

There is a length constraint on the narrow-wall-slot-HPB-array's design for the

industrial band, since it needs to be mountable on a land vehicle. Therefore for the narrow-wall-slot-HPB-array's design at 10GHz, its maximum length is restricted to 150mm. The length of the array is measured between the following two points: the location where the first array element's aperture begins, and the location where the last array element's aperture ends. From the analysis to follow, given the length restriction on the narrow-wall-slot-HPB-array, the optimal design for the distance between the elements and the elements' dimensions are such that the optimal narrow-wall-slot-HPB-array is made up of five elements.
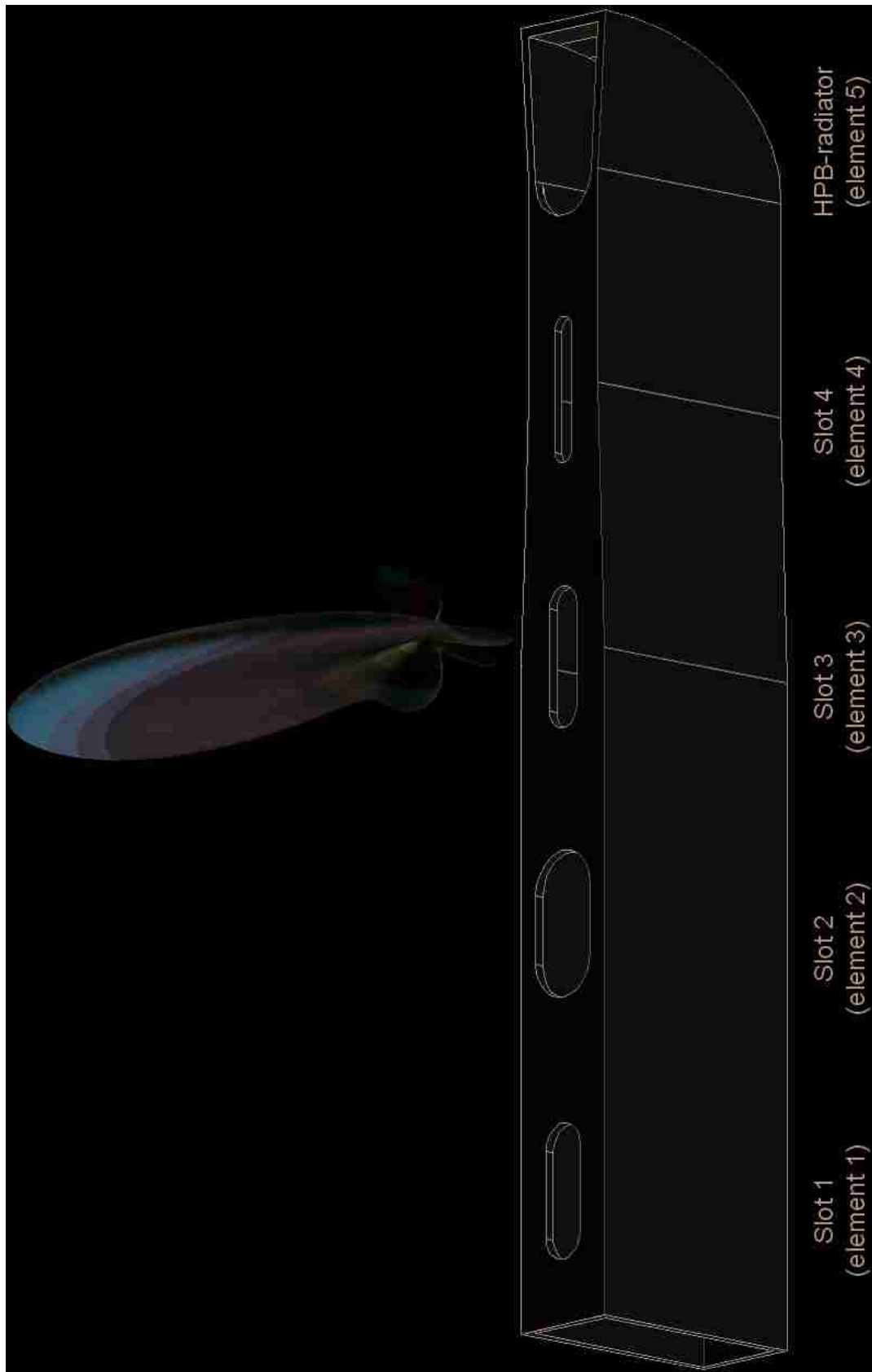
Figure 3.1. Narrow-wall-slot-HPB-array along with its 3-D radiation power pattern in absolute units.

3.1 <u>Microwave network analysis of narrow-wall-slot-HPB-array</u>

The narrow-wall-slot-HPB-array is designed by optimizing the mutual coupling through the waveguide between the array elements given the design variables and criteria. For this analysis, the external coupling between the array elements is ignored and the mutual coupling analysis is performed using microwave theory. Each radiating slot is reduced to a lossy two-port network, where the loss is representative of the power radiated by the slot; the HPB-radiator is represented as a lossy one-port network. The S-parameters and aperture phases of the array elements are obtained from computational analysis performed using HFSS; this discussion was presented in Chapters 1 and 2. Figure 3.2 shows the array in Figure 3.1 represented as a microwave network. P_{in1} through P_{in5} are the powers being input at the input ports of array elements 1 through 5 respectively as shown in Figure 3.2. P_{rad1} through P_{rad5} are the powers radiated by array elements 1 through 5 respectively as shown in Figure 3.2. Γ_1 through Γ_5 are the reflection coefficients under matched port conditions. For instance, Γ_1 is affected by the presence of slot 1 through slot 4 and the HPB-radiator and is the effective reflection coefficient at the input of the network shown, but assumes that the input of the network as a matched port.
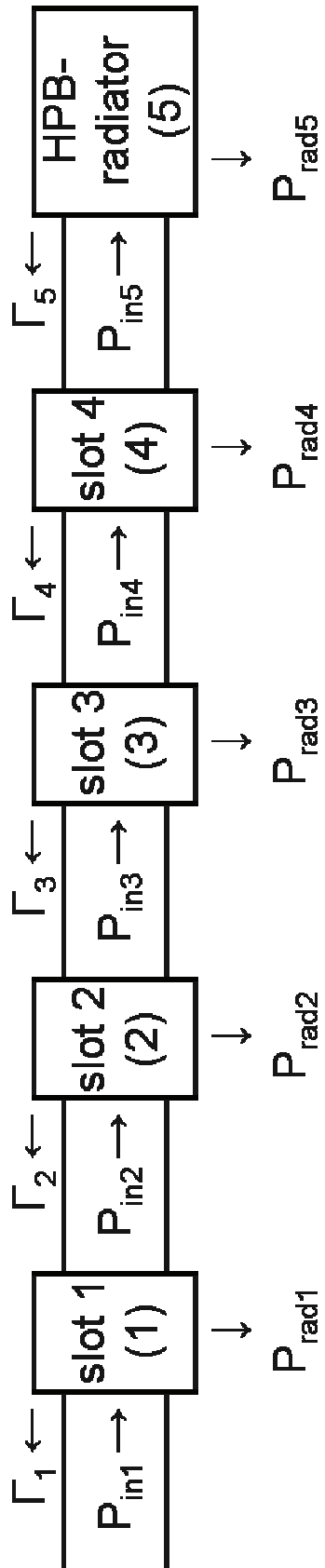
Figure 3.2. Equivalent microwave network of the narrow-wall-slot-HPB-array.

Γ_2 through Γ_5 in Figure 3.2 contribute to mutual coupling between the array elements and in the ideal case scenario it is better to have Γ_1 through Γ_5 equal to zero. In addition to the obvious reason for the reflected power to be minimized so as to maximize antenna efficiency/gain and protect the high power microwave source, an additional reason is as follows. There is a good possibility that the radiation pattern of the narrow-wall-slot-HPB-array would have its main lobe canted from the broadside direction, and since the design goal is to maximize the directivity, it is advantageous to have power flow in only one direction along the length of the linear array.

Although the powers radiated by all the elements (represented by P_{rad}s in Figure 3.2) need to be equal, the fraction of the power radiated to the amount of power being input to a certain element is different from the other elements. For instance, in the ideal case scenario: when Γ_1 through Γ_5 are equal to zero, the optimal values for P_{rad1} through P_{rad5} are given by $0.2P_{in1}$, $0.25P_{in2}$, $P_{in3}/3$, $0.5P_{in4}$, P_{in5} respectively. Since, in reality Γ_1 through Γ_5 are not equal to zero, the goal of the microwave network analysis is to obtain expressions for Γ_1, P_{rad1} through P_{rad5} in terms of: P_{in1}, the S-parameters of the array elements 1 through 5, and the distance between the array elements. The effect of mutual coupling on: the aperture phases obtained from computational analysis of the array elements 1 through 5, is factored in by simply knowing the distance between the elements and the phase of the input powers P_{in1} through P_{in5}. Hence, the aperture phase of slot 1 is only influenced by the phase of P_{in1} and the location of the array's input port from slot 1. Similarly, the aperture phase of slot 2 is only influenced by the phase of P_{in2} and the distance between slot 1 and slot 2. This aperture phase calculation procedure can be similarly extended to the array elements 3 through 5. Note that the aperture phase

calculations assume that the Γ s are small enough and therefore do not influence them.

The expressions for Γ_1, P_{rad1} through P_{rad5}, and the aperture phases can then be implemented in an iterative program whose inputs are the S-parameters and aperture phases for narrow-wall longitudinal-slots of various dimensions obtained from the computational analysis in Chapter 1. The program iterates on the possible distances/dimensions between/of the array elements without exceeding the maximum length constraint on the array, to find the best combination of slots' dimensions and inter-element spacing that produces the optimal narrow-wall-slot-HPB-array design.

The microwave network analysis is started by beginning at the HPB-radiator element and progressing towards the array input, one element at a time, until slot 1 is reached ('reverse path analysis'); then by progressing from slot 1 towards the end of the array, one element at a time, until the HPB-radiator element is reached ('forward path analysis'), completes the analysis. The goal of the reverse (forward) path analysis is to obtain the expression(s) for Γ_1 (P_{rad1} through P_{rad5}) in terms of P_{in1}, the S-parameters of the array elements 1 through 5, and the distance between the array elements.

The inter-element spacing between the array elements can be embedded as a phase shift in the S-parameters of the individual elements. This can be achieved by 'a shift in reference planes', and is discussed in detail in the section on 'the scattering matrix' in *[Pozar]*.

The first step in the reverse path analysis is illustrated in Figure 3.3. 'Load 5' in Figure 3.3 represents the array element 5. V_1^+, V_2^+, V_1^-, V_2^- in Figure 3.3 represent the voltage waves that are well known in the microwave network analysis performed using S-parameters. Following standard S-parameter network analysis, the network shown in

49

Figure 3.3 satisfies Equations 3.1, 3.2 and 3.3; S_{11}, S_{12}, S_{21}, S_{22} represent the S-parameters of the two-port network that represents slot 4; Γ_5 is the reflection coefficient of the one-port network (load 5) that represents the HPB-radiator under matched port condition.

$$V_2^+ = \Gamma_5 V_2^- \qquad (3.1)$$

$$V_2^- = S_{21} V_1^+ + S_{22} V_2^+ \qquad (3.2)$$

$$V_1^- = S_{11} V_1^+ + S_{12} V_2^+ \qquad (3.3)$$

Equations 3.1, 3.2, 3.3 can be solved to obtain the expressions in Equations 3.4 through 3.10. The reflection coefficient when port 1 of the network in Figure 3.3 is matched, Γ_4, shown in Equation 3.6 is calculated and recorded to be used in the second step of the reverse path analysis.

$$\frac{V_2^-}{V_1^+} = \frac{S_{21}}{1 - \Gamma_5 S_{22}} \qquad (3.4)$$

$$\frac{V_2^+}{V_1^+} = \frac{\Gamma_5 S_{21}}{1 - \Gamma_5 S_{22}} \qquad (3.5)$$

$$\Gamma_4 = \frac{V_1^-}{V_1^+} = S_{11} + \Gamma_5 S_{12} \frac{V_2^-}{V_1^+} \qquad (3.6)$$

$$P_{in5} = P_{in4} \left| \frac{V_2^-}{V_1^+} \right|^2 \qquad (3.7)$$

$$P_{ref4} = P_{in4} \left| \Gamma_4 \right|^2 \qquad (3.8)$$

$$P_{load5} = P_{in4} \left(\left| \frac{V_2^-}{V_1^+} \right|^2 - \left| \frac{V_2^+}{V_1^+} \right|^2 \right)$$ (3.9)

$$P_{rad4} = P_{in4} - P_{ref4} - P_{load5}$$ (3.10)

Where:

P_{in4} is the power being input at port 1 of the two-port network that represents slot 4 in Figure 3.3

P_{ref4} is the power reflected at port 1 in Figure 3.3 under matched port conditions

P_{load5} is the power delivered to the HPB-radiator

P_{rad4} is the power radiated by slot 4
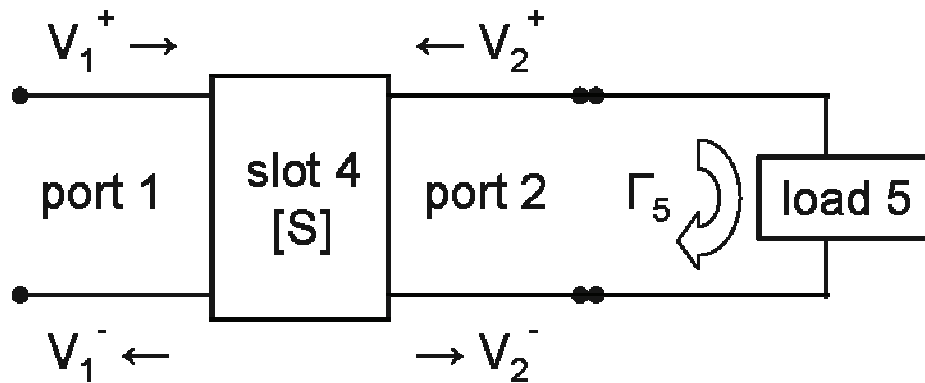
Figure 3.3. Illustration for the first step in the reverse path analysis.

In the second step of the reverse path analysis, the complete network in Figure 3.3 is considered as a single one-port network (labeled as 'load 4' in Figure 3.4) with Γ_4 computed in Equation 3.6 representing its reflection coefficient under matched port condition. This one-port network is now connected to the equivalent two-port network for slot 3 as shown in Figure 3.4. From this point, the analysis of this two-port network

51

connected to the one-port network continues in the same way as in step one of the reverse

path analysis: to obtain the reflection coefficient at port 1 in Figure 3.4 (Γ_3). In addition,

the following expressions are obtained in terms of the power being input at port 1 of the

two-port network that represents slot 3 in Figure 3.4 (P_{in3}): the power reflected at port 1

in Figure 3.4 (P_{ref3}), the power delivered to load 4 (P_{load4}) and the power radiated by slot

3 (P_{rad3}). This reverse path analysis procedure is complete when it is carried out all the

way until the first element (i.e. slot 1), at which point the value of the effective reflection

coefficient at the input of the complete network as shown in Figure 3.2 (Γ_1) is found.
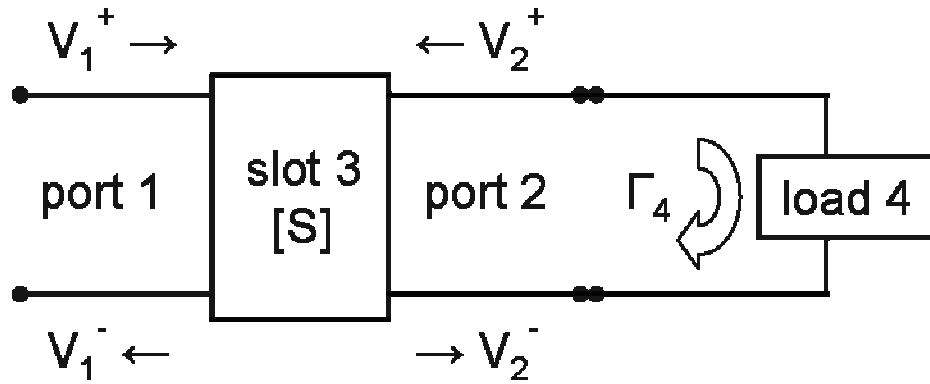
Figure 3.4. Illustration for the second step in the reverse path analysis.

Note that P_{rad1} through P_{rad5} cannot be computed in the reverse path analysis,

since P_{in1} through P_{in5} are unknown.

The forward path analysis also has a series of steps similar to reverse path

analysis, and the first step is illustrated in Figure 3.5. 'Load 2' in Figure 3.5 includes

array elements 2 through 5. Hence, it can be inferred that by starting from a known value

for P_{in1}, the values for P_{rad1} and P_{in2} can be found from the first step of the forward path

analysis. The second step of the forward path analysis is illustrated in Figure 3.6. 'Load

3' in Figure 3.6 includes array elements 3 through 5. From the value of P_{in2} obtained from the first step of the forward path analysis, the values for P_{rad2} and P_{in3} can be found from the second step of the forward path analysis. This analysis is complete when it is continued to eventually find all the powers radiated by the array elements, P_{rad1} through P_{rad5}.
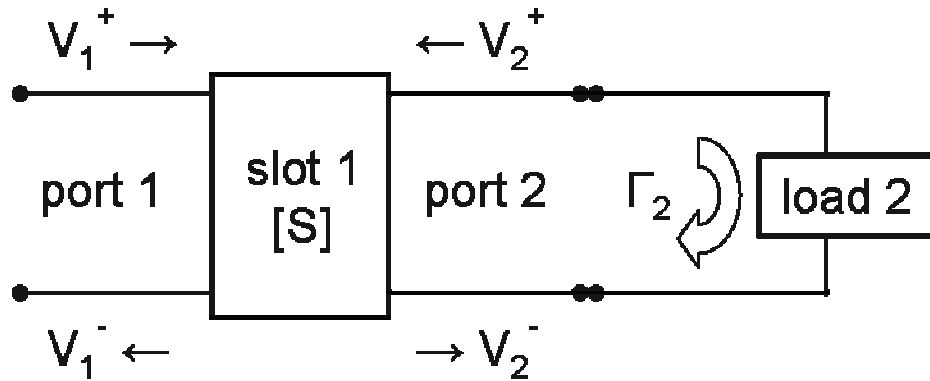
Figure 3.5. Illustration for the first step in the forward path analysis.
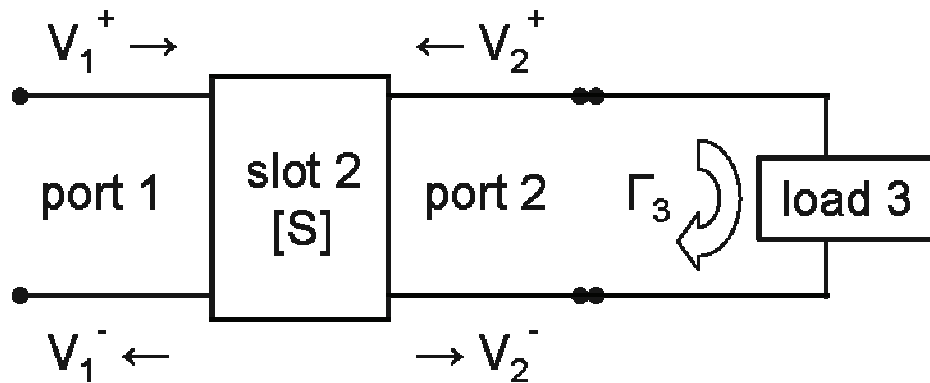
Figure 3.6. Illustration for the second step in the forward path analysis.

The S-parameters and aperture phases of the individual array elements are obtained from HFSS simulations and the coupling analysis is implemented in a routine

that iterates on the slots' dimensions and the distance between the array elements. The routine was coded in MATLAB. It is not possible to achieve the ideal case scenario: i.e. when Γ_1 through Γ_5 are equal to zero, the optimal values for P_{rad1} through P_{rad5} are given by $0.2P_{in1}$, $0.25P_{in2}$, $P_{in3}/3$, $0.5P_{in4}$, P_{in5} respectively. Hence the MATLAB routine was run for the following optimization criteria. The mean offset between the radiated powers was minimized with the following additional criteria imposed: the reflected power at the array input < 5%, the mean error in the progressive phase shift < 5$^\text{o}$. The inputs to the routine were the S-parameters and aperture phases of slots with lengths (widths) varying between 14mm (0.5mm) and 15mm (8mm), and the S-parameter and aperture phase of the optimal HPB-radiator element for the narrow-wall-slot-HPB-array presented in Chapter 2. The optimal values obtained from the MATLAB routine for the reflected power, mean error in the progressive phase shift, mean offset between the radiated powers are: <1%, 4.7$^\text{o}$, 1.2% respectively. The optimal spacing between the slots that achieved these results was $11\lambda_g/16$, where λ_g is the guide wavelength for an X-band waveguide operating at 10GHz. Also, there is a narrow-wall flare introduced near the array element 4, as shown in Figure 3.1, where the narrow dimension of the waveguide is squeezed by 20% to increase the radiated power through slot 4. Table 3.1 shows the optimal dimensions for slot 1 through slot 4, along with the powers radiated and aperture phases of the array elements 1 through 5. The aperture phase is the phase of the aperture E-field at the center of the aperture with reference to the phase of the input power (=0$^\text{o}$) at the input port of the array.

Array element	Slot dimensions	Radiated power	Aperture phase	Phase shift (mean=93.7°)
slot 1	14 x 5mm	19.8%	194.4°	
				93.3°
slot 2	15 x 8mm	19.6%	287.7°	
				94.4°
slot 3	14.5 x 4mm	19.8%	22.1°	
				84.6°
slot 4	15 x 2.5mm	17.5%	106.7°	
				102.3°
HPB-radiator		22.9%	209°	

Table 3.1. Results from mutual coupling optimization between the array elements. The aperture phase is the phase of the aperture E-field at the center of the aperture with reference to the phase of the input power (=0°) at the input port of the array.

3.2 Full-wave analysis of narrow-wall-slot-HPB-array

Since the results in table 3.1 do not include any external coupling between the array elements, the slot array is also simulated in HFSS using the optimal dimensions for the slots obtained from the MATLAB routine; the results from the HFSS simulation are as follows. The reflected power at the input of the array is <1%. Table 3.2 compares the values of power radiated and aperture phases of the array elements 1 through 5 obtained from this full-wave analysis with the optimized result from the MATLAB routine that uses microwave network analysis. Table 3.2 shows that there is good agreement between the microwave network analysis result and the full-wave analysis result.

Array element	Microwave network analysis		Full-wave analysis	
	Power radiated	Aperture phase	Power radiated	Aperture phase
slot 1	19.8%	194.4°	20.5%	202.3°
slot 2	19.6%	287.7°	20.4%	290.4°
slot 3	19.8%	22.1°	20.1%	31.7°
slot 4	17.5%	106.7°	16.8%	109.1°
HPB-radiator	22.9%	209°	22%	207.6°

Table 3.2. Results from microwave network analysis and full-wave analysis. The aperture phase is the phase of the aperture E-field at the center of the aperture with reference to the phase of the input power (=0⁰) at the input port of the array.

3.3 Double-narrow-wall-slot-HPB-array

The peak gain for the optimized narrow-wall-slot-HPB-array is approximately 12.6dB; this gain can be increased to approximately 14.9dB when the configuration shown in Figure 3.7 is used. The double-narrow-wall-slot-HPB-array, shown in Figure 3.7, is obtained from two narrow-wall-slot-HPB-arrays as follows. The double-narrow-wall-slot-HPB-array consists of two identical narrow-wall-slot-HPB-arrays with a common broad wall; the slots are moved as close to the common wall as possible. In the double-narrow-wall-slot-HPB-array configuration, the apertures of one narrow-wall-slot-HPB-array alternate with those of the other array and the center-to-center distances between the elements of the double-narrow-wall-slot-HPB-array are equal. The input phase of one array also needs to be appropriately phase shifted from the other, such that

the aperture phases of the elements of the double-narrow-wall-slot-HPB-array are in approximately a constant phase progression. The double-narrow-wall-slot-HPB-array has essentially the same overall length as the narrow-wall-slot-HPB-array, but by increasing the number of elements in the array that are in approximately a constant favorable phase progression, a higher gain was achieved. In other words, the aperture field distribution of the double-narrow-wall-slot-HPB-array is more uniform than that of the narrow-wall-slot-HPB-array, thereby resulting in a higher gain for the double-narrow-wall-slot-HPB-array.

The aperture phases/magnitudes of an antenna array interfere constructively or destructively in various directions to produce the 3-D radiation pattern. For a pencil-beam-antenna-array that radiates a perfect pencil-beam radiation pattern, its aperture phases/magnitudes are such that they constructively interfere in a very narrow set of adjacent angles in approximately the same direction that the element pattern's maxima is directed, and in the rest of the angles the aperture phases/magnitudes of the array interfere destructively.

The double-narrow-wall-slot-HPB-array produces a radiation pattern that is more similar to the pencil-beam-antenna-array's radiation pattern, when compared to the narrow-wall-slot-HPB-array. Figure 3.8 shows that the higher gain of the double- narrow-wall-slot-HPB-array compared to that of the narrow-wall-slot-HPB-array is achieved by suppressing the side lobes. Note that the vertical axis in Figures 3.8 and 3.9 represents the 'normalized' power radiated.
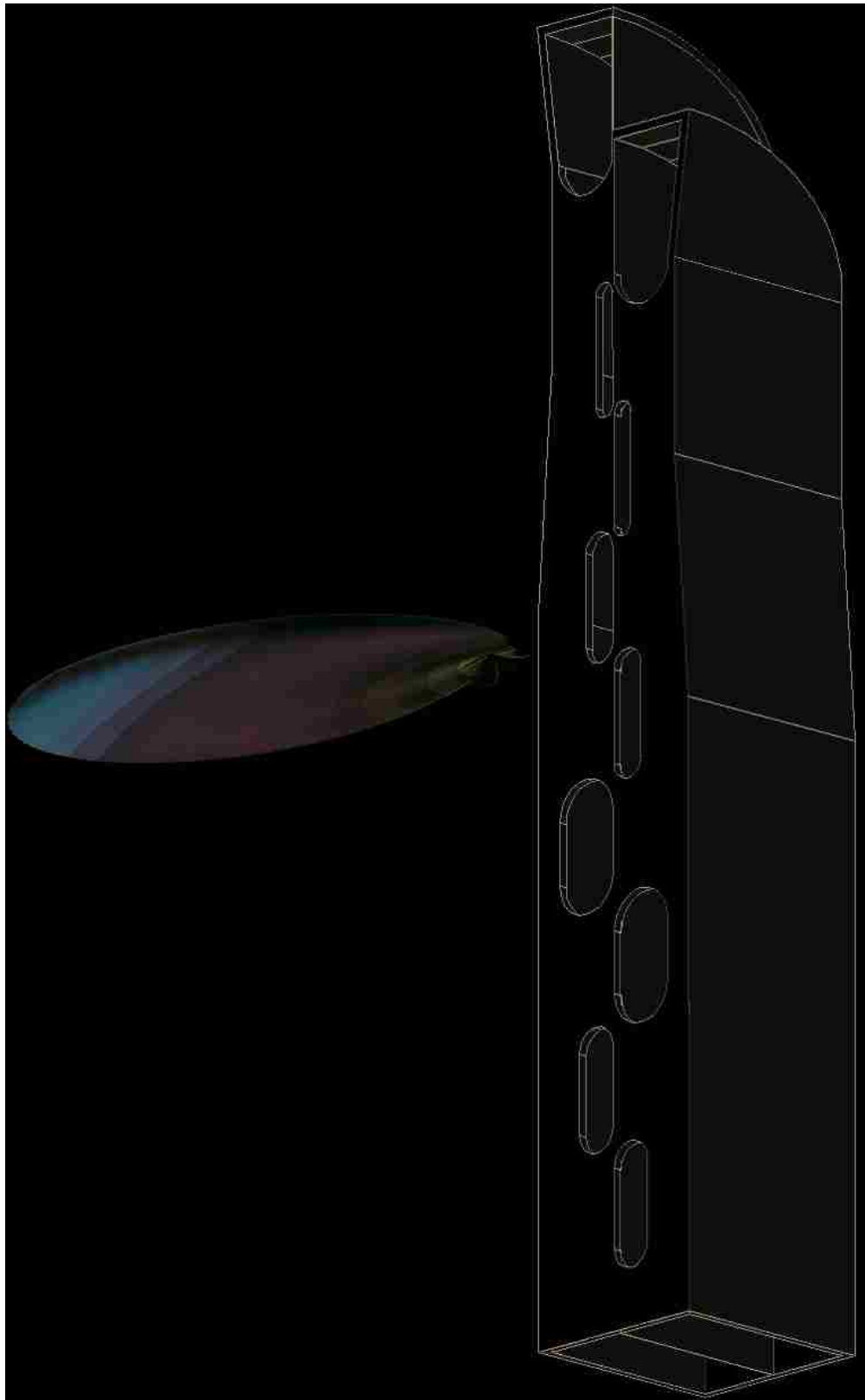
Figure 3.7. Double-narrow-wall-slot-HPB-array along with its 3-D radiation power pattern in absolute units.

Figure 3.8 compares the H-plane radiation power patterns of the narrow-wall-slot-HPB-array and the double-narrow-wall-slot-HPB-array; $\theta = 0^o$ on the horizontal axis of the plot in Figure 3.8 corresponds to the broadside direction. The H-plane radiation power pattern of the double-narrow-wall-slot-HPB-array was shifted by 1°, so that the peaks of both patterns line up for making the beam-width comparison easier.
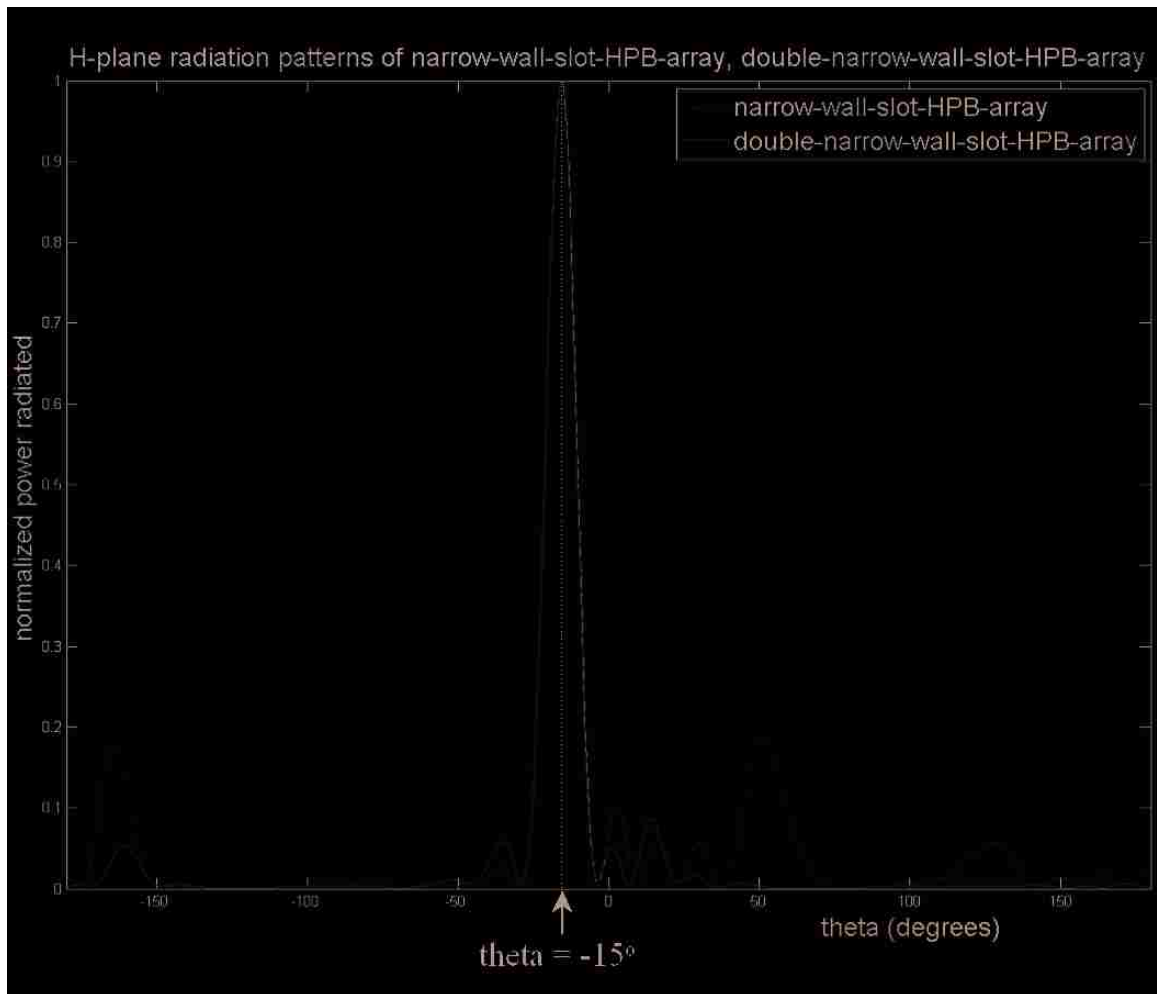
Figure 3.8. H-plane radiation power patterns of the narrow-wall-slot-HPB-array and the double-narrow-wall-slot-HPB-array.

Figure 3.9 compares the radiation power patterns of the narrow-wall-slot-HPB-array and the double-narrow-wall-slot-HPB-array in the plane cut that is orthogonal to the H-plane and passing through the θ = -15° line shown in Figure 3.8; θ = 0° on the horizontal axis of the plot in Figure 3.9 corresponds to the same spatial point in the 3-D radiation power pattern as θ = -15° on the horizontal axis of the plot in Figure 3.8.

Radiation patterns in orthogonal plane to H-plane & passing through theta=-15° line marked in Figure 3.8
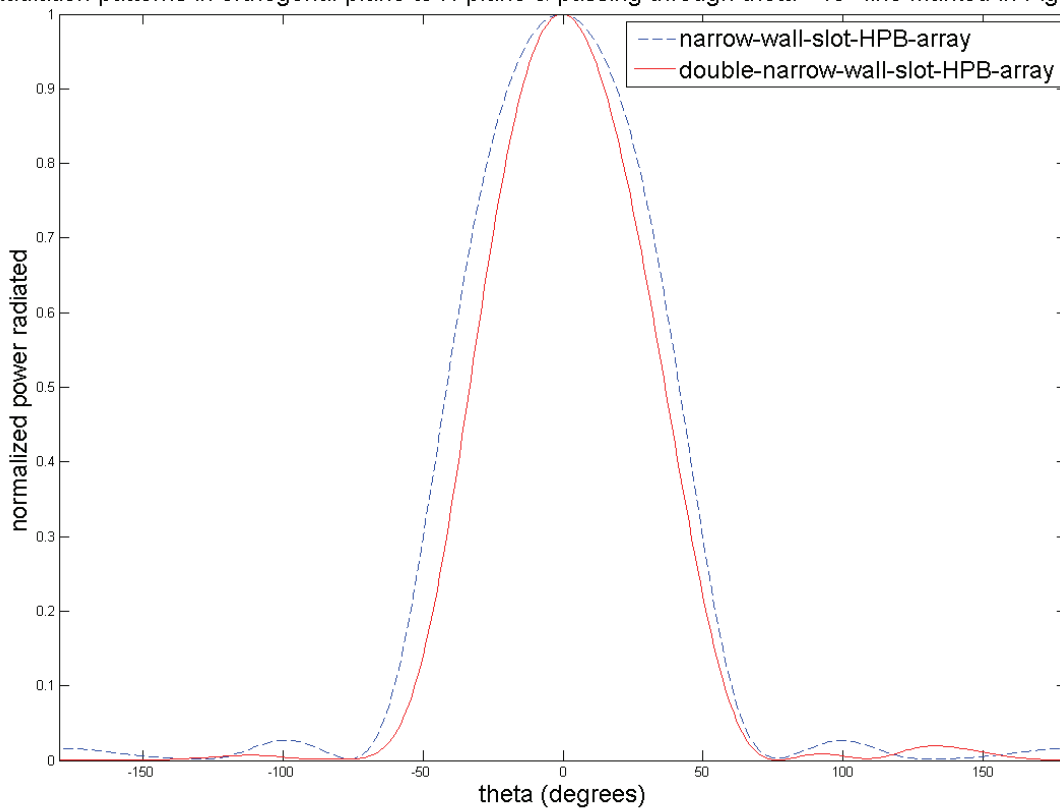
Figure 3.9. Radiation power patterns of the narrow-wall-slot-HPB-array and the double-narrow-wall-slot-HPB-array in the plane cut that is orthogonal to the H-plane and passing through the θ = -15° line shown in Figure 3.8.

4. SPLIT-WAVEGUIDE-HPB-ARRAY

The split-waveguide-HPB-array has an array of HPB-radiators with a split-waveguide input as shown in Figure 4.1. The split-waveguide-HPB-array has the added functionality of the capability to beam steer over the narrow-wall-slot-HPB-array. As shown in Figure 4.1, the split-waveguide-HPB-array has a split waveguide input with each split-input feeding a single HPB-radiator and hence its capability to beam steer. When the split-waveguide input is fed by a single waveguide, because of the orientation of the splits, the propagating dominant (TE_{10}) mode is preserved in each of the split-waveguides.
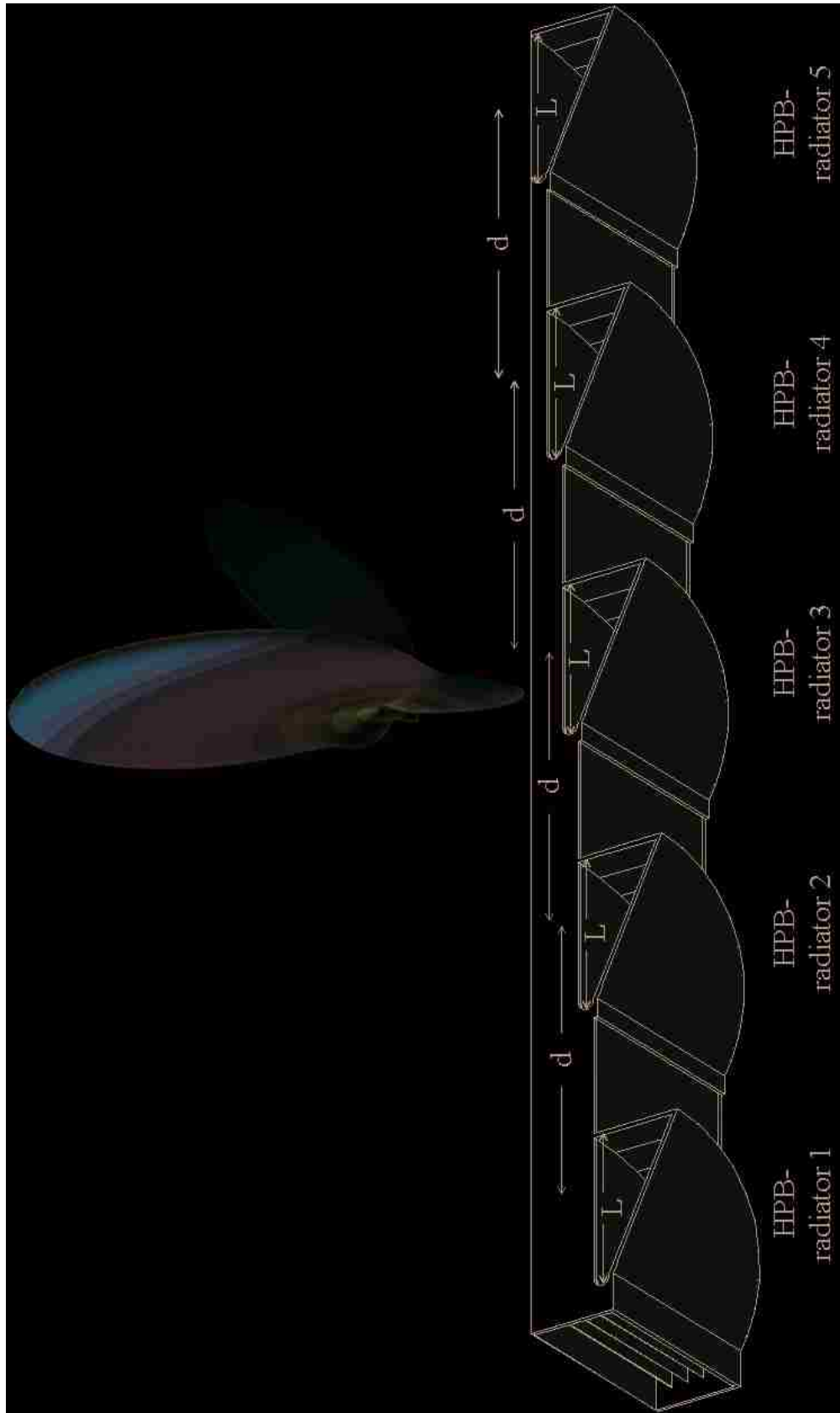
Figure 4.1. Split-waveguide-HPB-array along with its 3-D radiation power pattern in absolute units.

Energy from a single high power source can be divided using the split-waveguide design. Before the energy is sent to the split-waveguide-HPB-array, phase shifters can be inserted in the circuit. The phase shifters can be programmed to achieve a certain beam steer angle for every operating cycle of the high power source.

The capability to beam steer makes a high power antenna more versatile. For instance, some applications might require that the antenna be oriented such that the target-distance is 100m away from the vehicle, while some others might require this distance to be just 30m away from the vehicle. Without the capability to beam steer, a mechanical system needs to be put in place that can change the orientation of the antenna when/as desired. But even the best mechanical system might not be able to beam steer as fast as phase shifters controlling the individual inputs to an antenna array. The narrow-wall-slot-HPB-array design in the industrial band cannot beam steer without a bulky mechanical system. The split-waveguide-HPB-array can overcome this problem.

The length constraint imposed on the narrow-wall-slot-HPB-array's design at 10GHz, 150mm, is also imposed on the design of the split-waveguide-HPB-array. The length of the array is again measured between the following two points: the location where the first array element's aperture begins, and the location where the last array element's aperture ends.

The design of the split-waveguide-HPB-array is optimized for maximum directivity in the H-plane for the case when the split-inputs of the array do not have any phase shifts introduced, i.e. when a single waveguide feeds all the split-inputs of the array. Hence, the split-waveguide-HPB-array's uniform array design process is simplified compared to the narrow-wall-slot-HPB-array. Unlike the narrow-wall-slot-HPB-array,

the elements of the split-waveguide-HPB-array are identical and have negligible mutual coupling through the waveguide, since the HPB-radiator element has minimal reflected power into its feed-guide.

The standard HPB-radiator element used in the split-waveguide-HPB-array has a desirable half sine wave aperture E-field distribution with very little reflected power into the guide as seen in Chapter 2. Therefore the design goal of the split-waveguide-HPB-array from this point is to figure out the number of HPB-radiator elements (N) and the spacing (d) between them so that the array's directivity in the H-plane is maximized, while the length constraint on the array still holds. In addition to satisfying the length constraint, the aperture length of the HPB-radiator element (L, shown in Figure 4.1) sets a lower limit on the spacing between the array elements (i.e. $d \geq L$). Hence the design problem is two-dimensional and can be approximated to the design of a uniform linear array shown in Figure 4.2. For a uniform linear array with N elements, the normalized array factor (*AF*) is rotationally symmetric around the axis of the linear array and its value in any one of these plane cuts passing through the axis of the linear array is given by Equation 4.1 *[Balanis]*.

$$AF = \frac{1}{N} \frac{\sin\left(\frac{N}{2}\psi\right)}{\sin\left(\frac{1}{2}\psi\right)} \qquad (4.1)$$

Where:

$\psi = kd\cos\theta - \beta d$

N is the number of elements in the uniform linear array

θ, d are measured as shown in Figure 4.2

$$k = \frac{2\pi}{\lambda}$$

$$\beta = \frac{2\pi}{\lambda_g}$$

λ is the free-space wavelength

λ_g is the guide wavelength
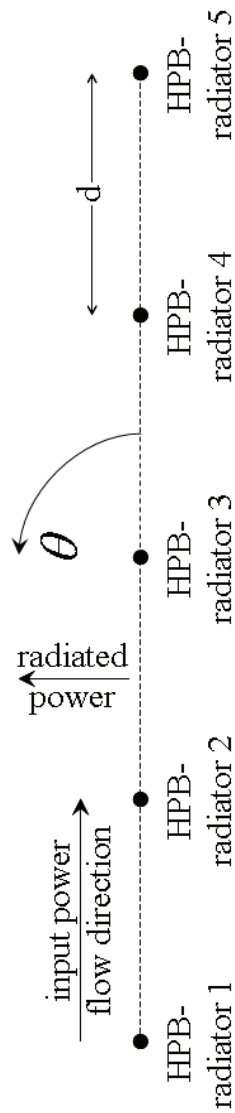
Figure 4.2. The approximately equivalent uniform array design problem for the split-waveguide-HPB-array shown in Figure 4.1.

The total pattern (*TP*) of the uniform linear array, shown in Figure 4.2, can be computed by simply multiplying its normalized array factor (*AF*) with the normalized radiation amplitude pattern (i.e. the element pattern, *EP*) of the split-waveguide-HPB-array's standard HPB-radiator element in the H-plane.

A program was developed in MATLAB that iterates on the values of 'N'and 'd' to maximize the directivity of the total pattern of the array, while satisfying the maximum length constraint on the array and the lower limit on the value of 'd' that is set by 'L'. The value of N (*d*) was varied from 2 ($0.45\lambda_g$) to 10 ($1.0\lambda_g$). The directivity of the total pattern of the array was maximized for N=5 and d=0.81λ_g; the resulting H-plane normalized radiation power patterns for the *AF*, *TP*, in addition to the H-plane normalized radiation power pattern for the *EP* are shown in Figure 4.3. Note that the horizontal axis in Figure 4.3 was made to be consistent with Figure 3-8, and is not consistent with the illustration in Figure 4.2 and Equation 4.1. Hence, $\theta = 0^{\circ}$ on the horizontal axis of the plot in Figure 4.3 corresponds to the broadside direction of the array.
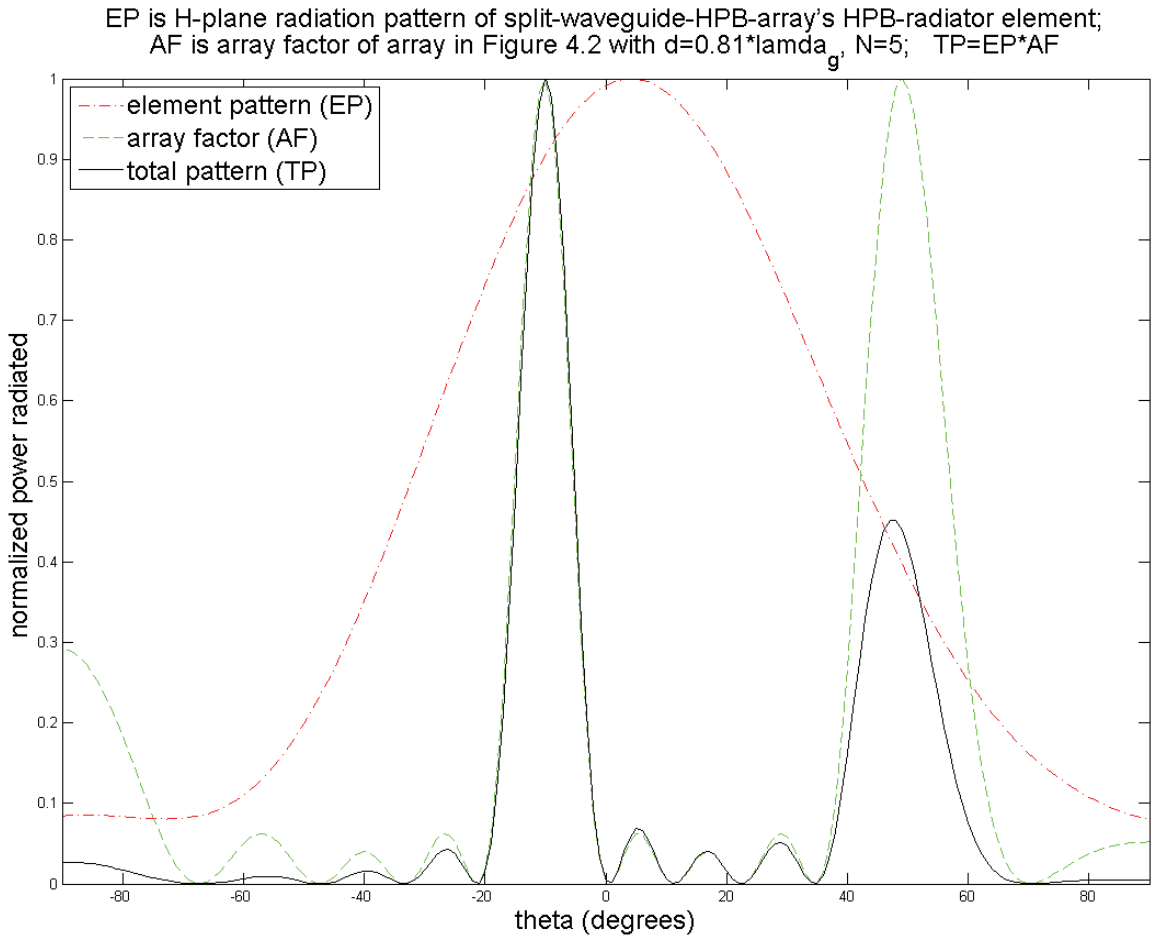
Figure 4.3. Optimal H-plane normalized radiation power patterns for *AF*, *TP* (for *N*=5 and

_d_=0.81 λ_g); H-plane normalized radiation power pattern for *EP* included.

Note that the results from the MATLAB routine are only optimal for the array

shown in Figure 4.2, which is an approximation of the split-waveguide-HPB-array shown

in Figure 4.1. So the results from the MATLAB routine were used as a guideline for

constructing the split-waveguide-HPB-array in HFSS and the distance between the

elements (d) was again iterated on, but this time, while performing a full-wave analysis

on the array. The optimal inter-element spacing distance, 'd' obtained from the full-wave

analysis was d=0.83 λ_g, which still satisfies the maximum length constraint on the array. The array shown in Figure 4.1 is the optimal split-waveguide-HPB-array.

4.1 Double- split-waveguide-HPB-array

The double-split-waveguide-HPB-array (shown in Figure 4.4) is obtained from the split-waveguide-HPB-array in the same way as the double-narrow-wall-slot-HPB-array is obtained from the narrow-wall-slot-HPB-array and is discussed in Section 3.3. The advantages of the double-split-waveguide-HPB-array over the split-waveguide-HPB-array are also similar to the ones discussed in Section 3.3. Similar to what was seen in Section 3.3, Figure 4.5 shows that the higher gain of the double-split-waveguide-HPB-array (approximately 15dB) compared to that of the split-waveguide-HPB-array (approximately 12dB) is achieved by suppressing the side lobes. Note that the vertical axis in Figures 4.5 and 4.6 represents the 'normalized' power radiated.
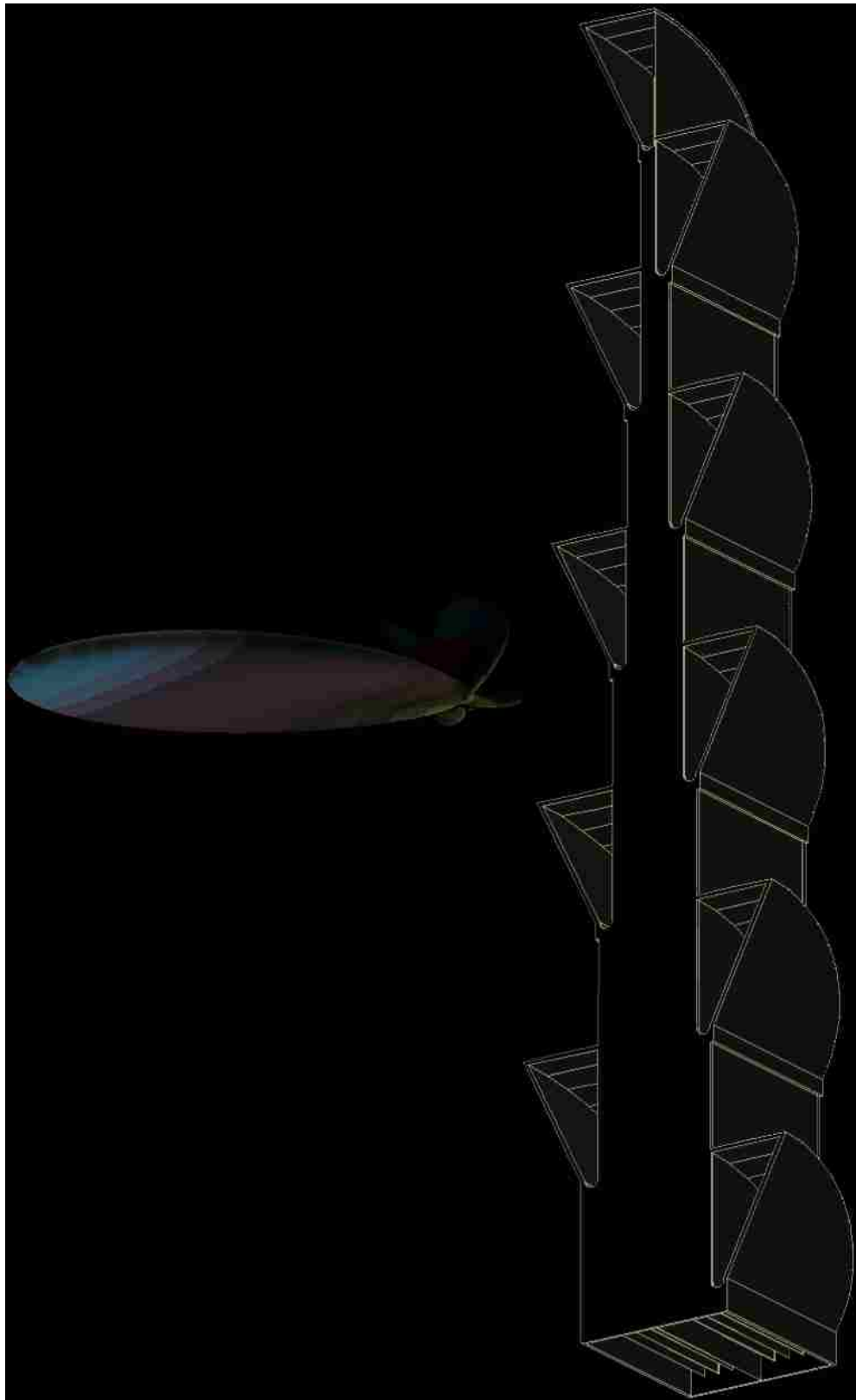
Figure 4.4. Double-split-waveguide-HPB-array along with its 3-D radiation power pattern in absolute units.

69

Following the definition of the pencil-beam-antenna-array presented in Section 3.3, the double-split-waveguide-HPB-array produces a radiation pattern that is more similar to the pencil-beam-antenna-array's radiation pattern, when compared to the split-waveguide-HPB-array.

Figure 4.5 compares the H-plane radiation power patterns of the split-waveguide-HPB-array and the double- split-waveguide-HPB-array; $\theta = 0^o$ on the horizontal axis of the plot in Figure 4.5 corresponds to the broadside direction.
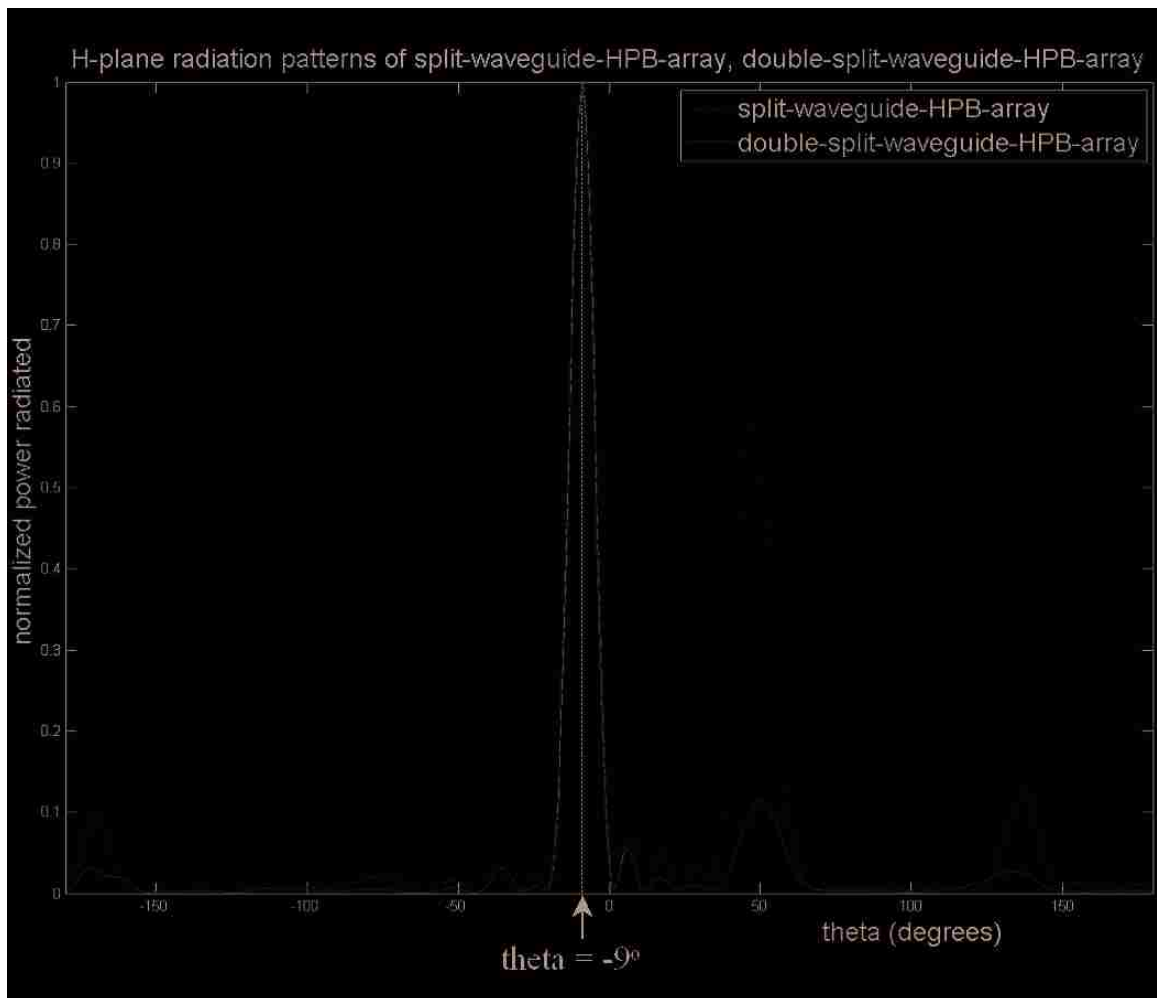
Figure 4.5. H-plane radiation power patterns of the split-waveguide-HPB-array and the double-split-waveguide-HPB-array.

Figure 4.6 compares the radiation power patterns of the split-waveguide-HPB-array and the double-split-waveguide-HPB-array in the plane cut that is orthogonal to the H-plane and passing through the $\theta = -9^{o}$ line shown in Figure 4.5; $\theta = 0^{o}$ on the horizontal axis of the plot in Figure 4.6 corresponds to the same spatial point in the 3-D radiation power pattern as $\theta = -9^{o}$ on the horizontal axis of the plot in Figure 4.5.

Radiation patterns in orthogonal plane to H-plane & passing through theta=-9° line marked in Figure 4.5
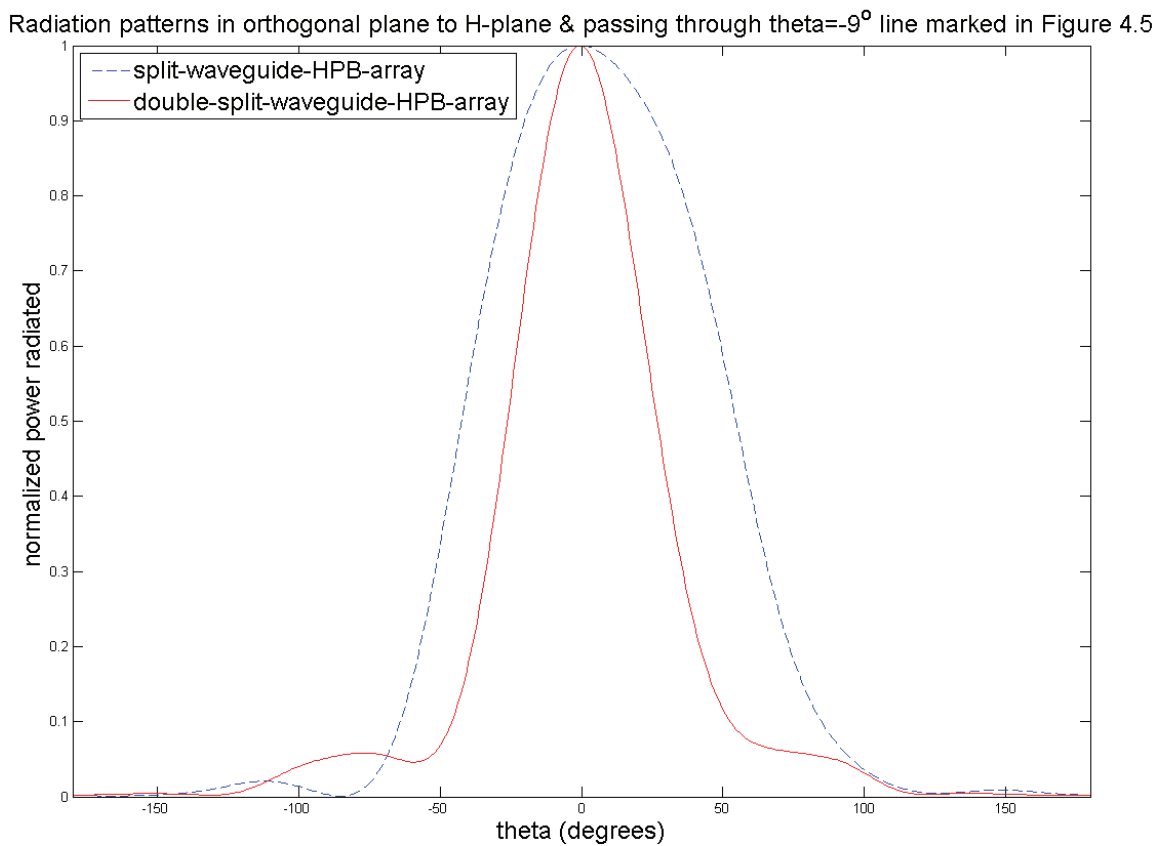
Figure 4.6. Radiation power patterns of the split-waveguide-HPB-array and the double- split-waveguide-HPB-array in the plane cut that is orthogonal to the H-plane and passing through the $\theta =$ -9° line shown in Figure 4.5.

71

5. EXPERIMENTAL RESULTS AT 10GHz AND ARRAY DESIGNS IN THE INDUSTRIAL FREQUENCY BAND

5.1 Experimental results at 10GHz

The experiments were conducted in the X-band, at 10GHz. In the first experiment, an HPB-radiator's design without the flare in the narrow wall of the waveguide was verified with the same structure's full-wave analysis results. A schematic of the X-band HPB-radiator's design used to generate the full-wave analysis results in HFSS is shown in Figure 5.1(a). Figure 5.1(b) shows the actual X-band HPB-radiator used for obtaining the experimental results. Theoretically, the narrow-wall flare in a rectangular waveguide only affects the power density inside the guide and has no effect on the propagating dominant mode structure, as long as the maximum dimension achieved by the narrow wall of the waveguide still only supports the dominant (TE_{10}) mode and not any higher order modes. Therefore the narrow-wall flare should not dominate the skewing of the experimental results from theory. Removing the narrow-wall flare for experimental verification purposes is very desirable since it greatly reduces the machining complexity.

Figure 5.1. (a) Schematic of X-band HPB-radiator for experimental verification. (b) X-band HPB-radiator used for experimental verification.

Since the split-waveguide-HPB-array has minimal mutual coupling between its elements through the waveguide, it is not proposed for experimental verification. In the second experiment, a narrow-wall-slot-HPB-array's design without any narrow-wall flare is verified with the same structure's simulation results; the justification and advantage for removing the narrow-wall flare for experimental verification purposes are the same as those mentioned previously in this section. A schematic of the X-band narrow-wall-slot-HPB-array's design used to generate the full-wave analysis results in HFSS is shown in Figure 5.2(a). Figure 5.2(b) shows the actual X-band narrow-wall-slot-HPB-array used for obtaining the experimental results. The dimensions of the HPB-radiator element used in the X-band narrow-wall-slot-HPB-array's design are the same as those shown in Figure 5.1(a). The dimensions of the array elements 1 through 4 (i.e. slot 1 through slot 4) and the inter-element spacing used in the X-band narrow-wall-slot-HPB-array's design are shown in Figure 5.2(a).
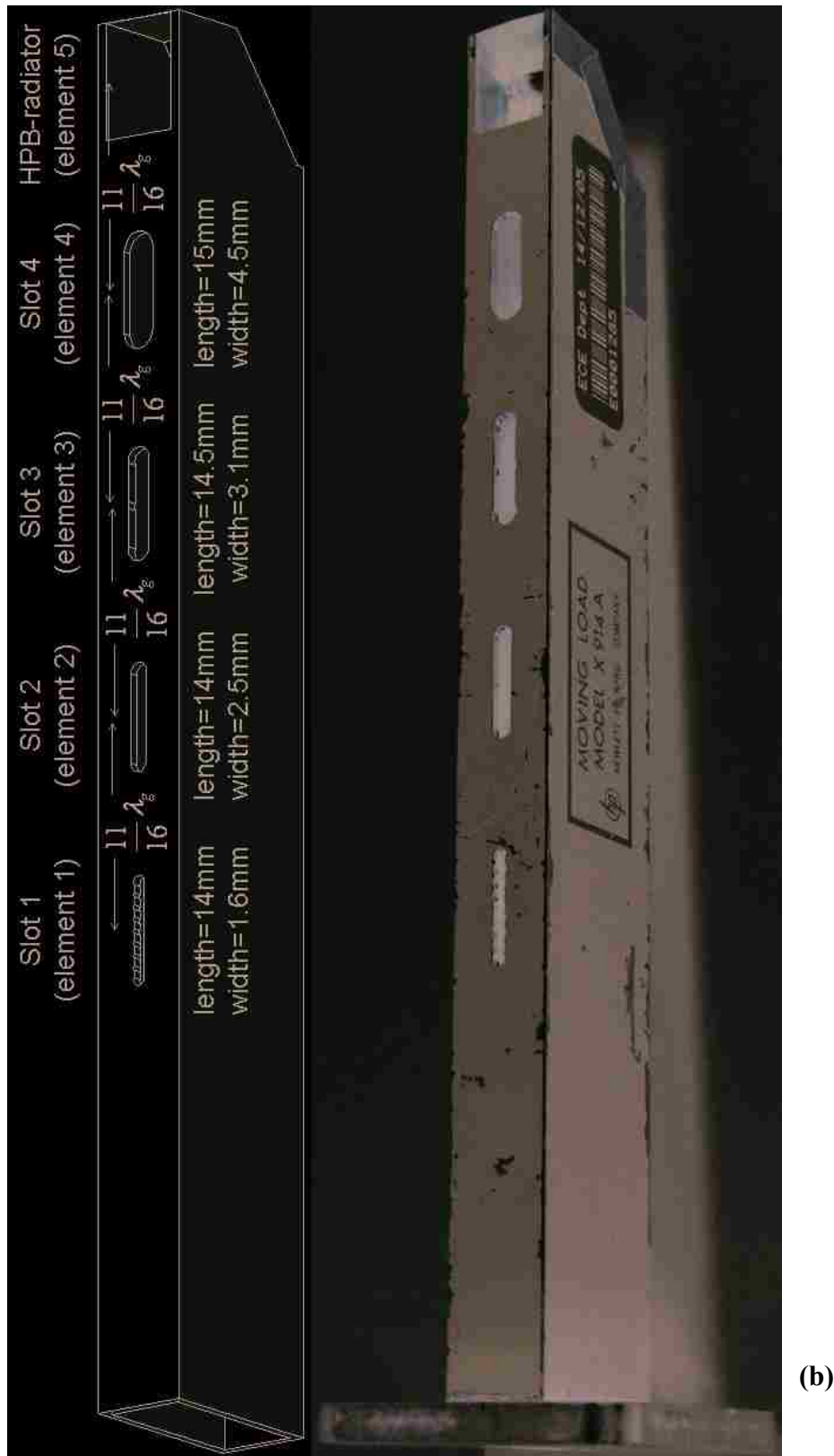
(b)

Figure 5.2. (a) Schematic of X-band narrow-wall-slot-HPB-array for experimental verification. (b) X-band narrow-wall-slot-HPB-array used for experimental verification.

75

Figure 5.3 shows the experimental set-up used to measure the reflection coefficients of the X-band HPB-radiator element and the X-band narrow-wall-slot-HPB-array designs shown in Figures 5.1 and 5.2 respectively. The reflection coefficients are obtained by sampling the standing wave patterns on the X-band waveguide slotted line shown in Figure 5.3; this technique is discussed in *[Pozar]*. For obtaining the standing wave ratio (SWR) measurements and measuring the minima locations along the length of the slotted line, the X-band HPB-radiator, the X-band narrow-wall-slot-HPB-array, and the reference short circuit (shorting plate) are connected at the 'test port' shown in Figure 5.3. The magnitude of the reflection coefficient is obtained from the corresponding SWR measurement. The phase of the reflection coefficient is computed by comparing the offset between the minima locations of the test device's standing wave pattern with those of the reference shorting plate. Table 5.1 compares the reflection coefficients obtained from the HFSS simulations and experiments, and there is good agreement between the theoretical analysis and experiments.
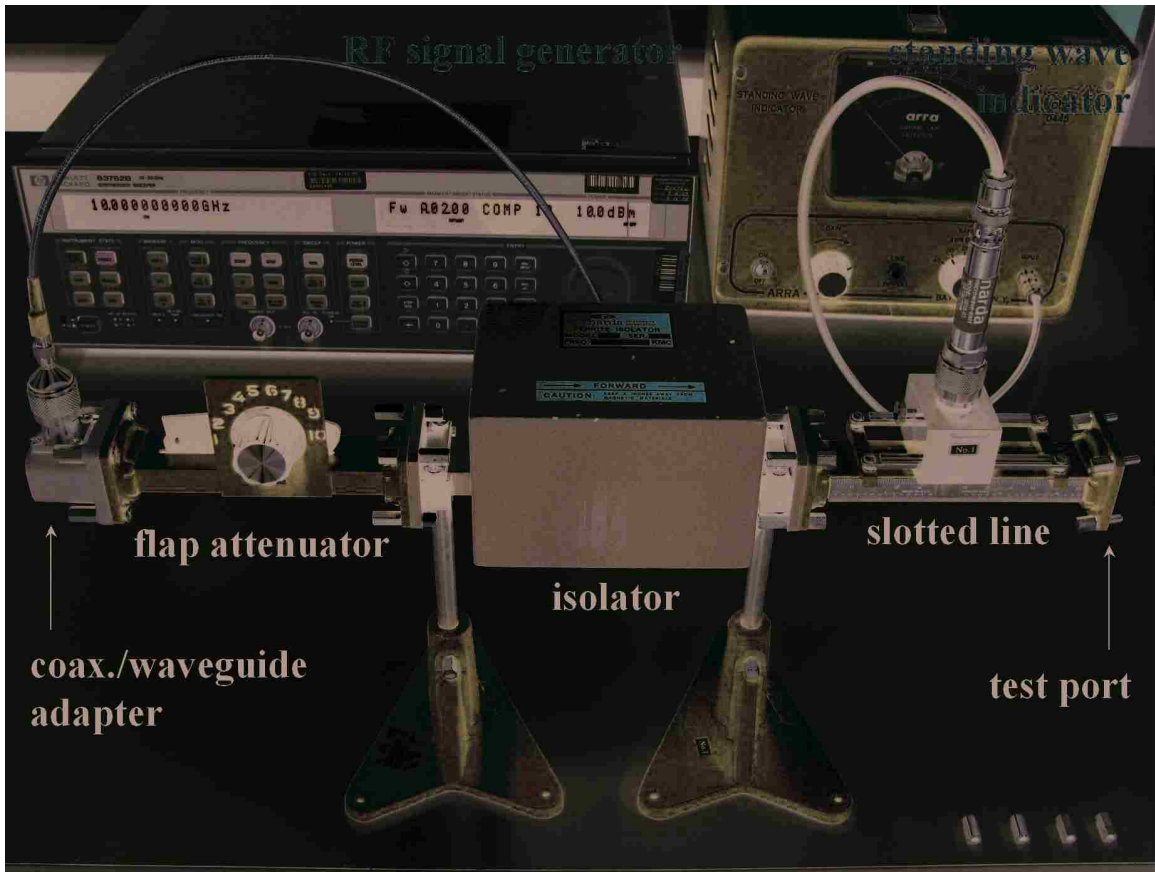
Figure 5.3. Experimental set-up for measuring reflection coefficient using the slotted line technique.

	Reflection coefficient	
Antenna	Full-wave analysis result	Experimental result
HPB-radiator	$0.17\angle-136°$	$0.18\angle-144°$
narrow-wall-slot-HPB-array	$0.17\angle162°$	$0.18\angle155°$

Table 5.1. Reflection coefficients obtained from theoretical analysis and experiments.

Figure 5.4(a) (5.5(a)) shows the experimental set-up used to measure the H-plane (E-plane) radiation pattern of the X-band HPB-radiator element. Similarly, Figure 5.6(a) (5.7(a)) shows the experimental set-up used to measure the radiation pattern in the H-plane (plane cut that is orthogonal to the H-plane and passing through the $\theta = -18^{\circ}$ line shown in Figure 5.6(b)) of the X-band narrow-wall-slot-HPB-array. The description for the radiation pattern measurement system is as follows. The transmitting antenna is a standard gain horn antenna and is mounted on a fixed axis as shown in Figures 5.4(a) through 5.7(a). The receiving antenna is the antenna under test and is mounted on a rotating axis as shown in Figures 5.4(a) through 5.7(a). Each of the measurement set-ups in Figures 5.4(a) through 5.7(a) is such that the transmitting and receiving antennas' polarizations are in the same direction.

Figures 5.4(b) through 5.7(b) compare the measured radiation patterns, from the corresponding experimental set-ups in Figures 5.4(a) through 5.7(a) respectively, with the HFSS simulation results. There is again good agreement between the theoretical analysis and experiments.

Figure 5.4(a). Experimental set-up used to measure the H-plane radiation pattern of X-band HPB-radiator element.

Figure 5.4(b). H-plane radiation pattern of X-band HPB-radiator.

Figure 5.4(b) (5.5(b)) compares the theoretical and experimental H-plane (E-plane) radiation power patterns of the X-band HPB-radiator element; $\theta = 0^o$ on the horizontal axis of the plot in Figure 5.4(b) (5.5(b)) corresponds to the broadside direction of the X-band HPB-radiator element.
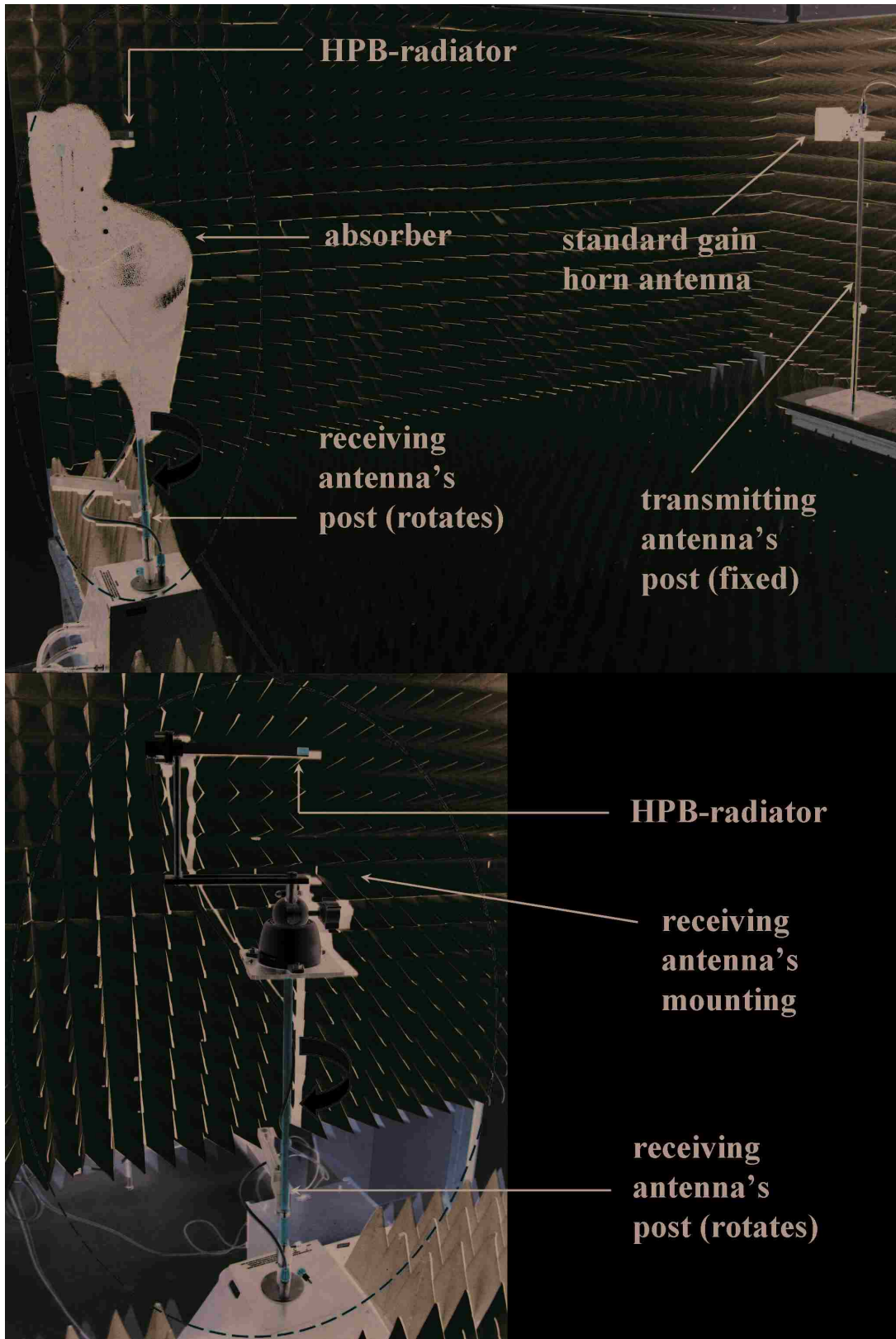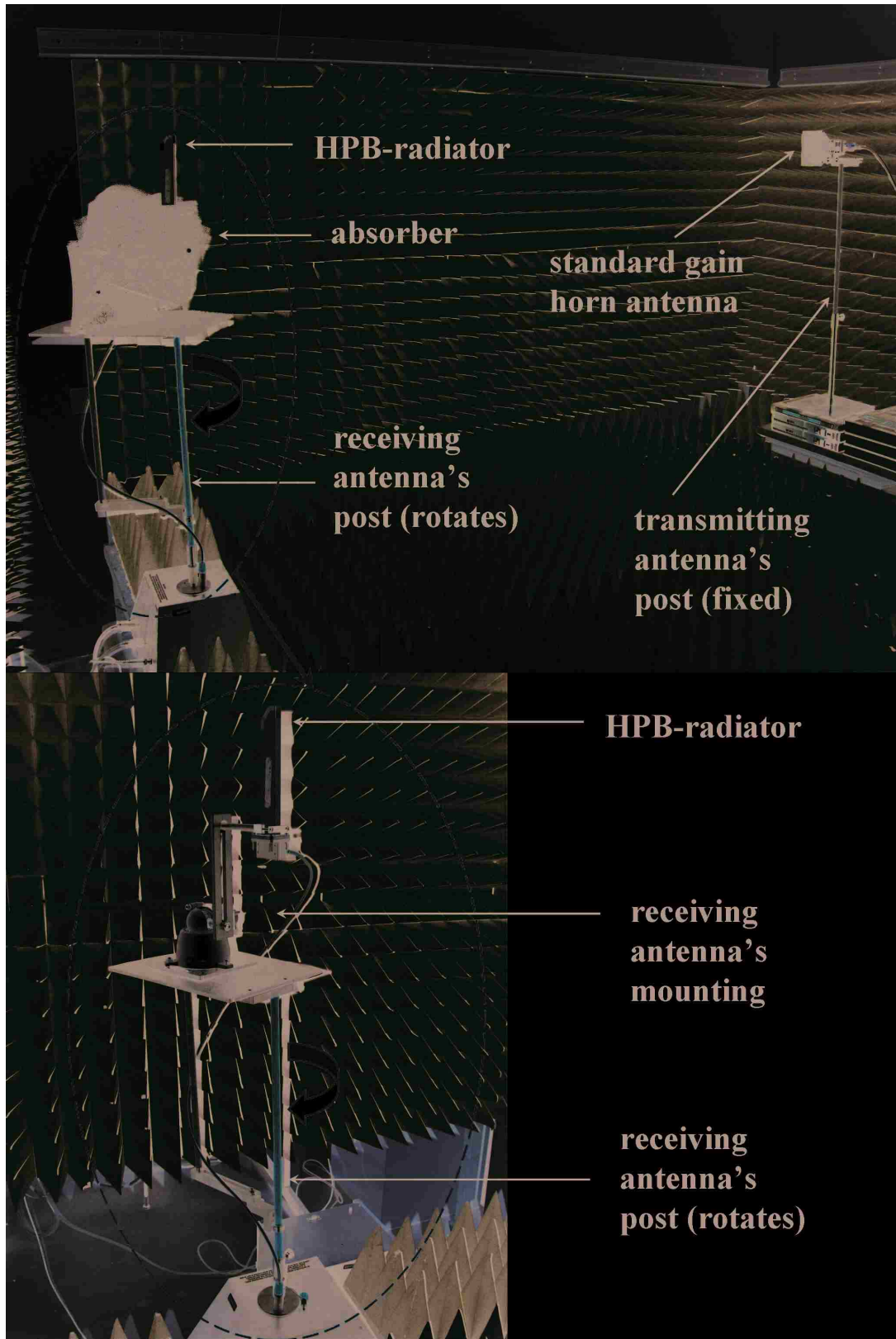
Figure 5.5(a). Experimental set-up used to measure the E-plane radiation pattern of X-band HPB-radiator element.
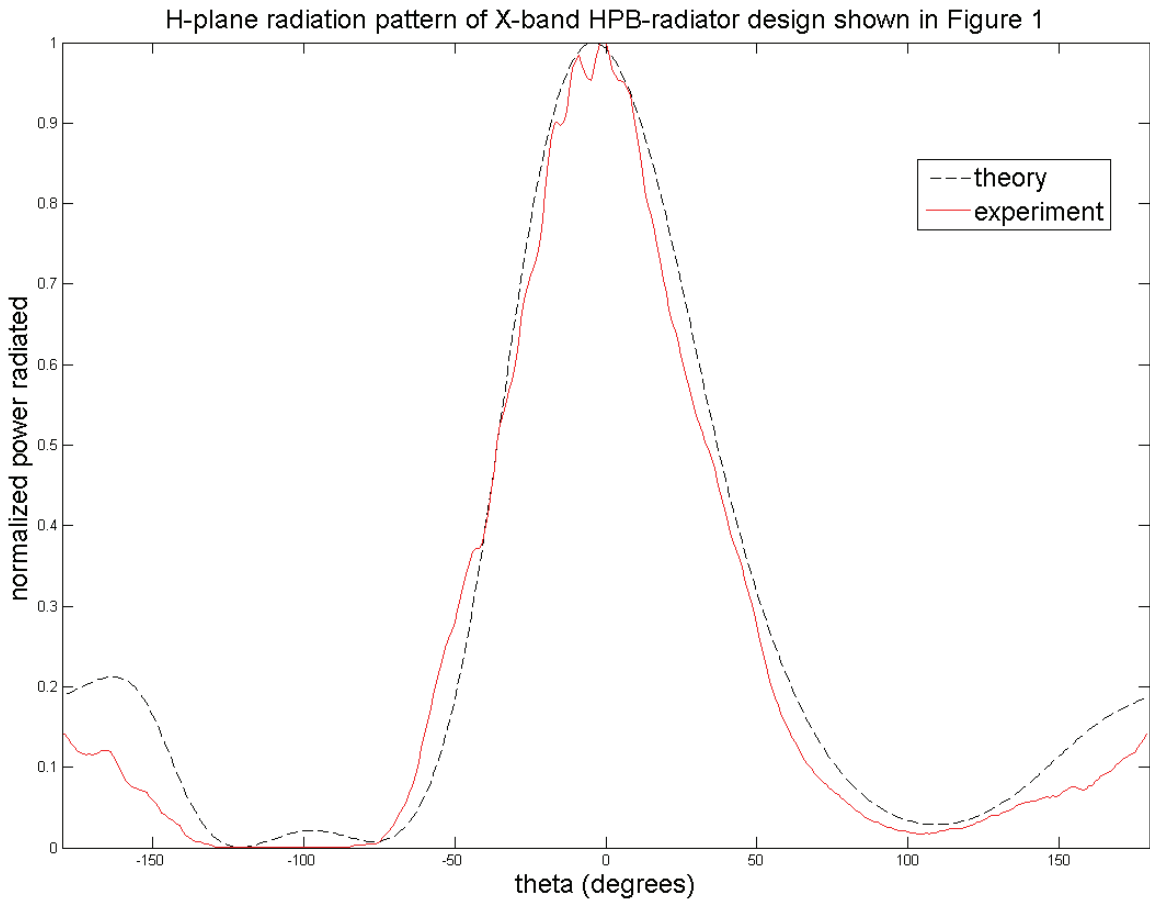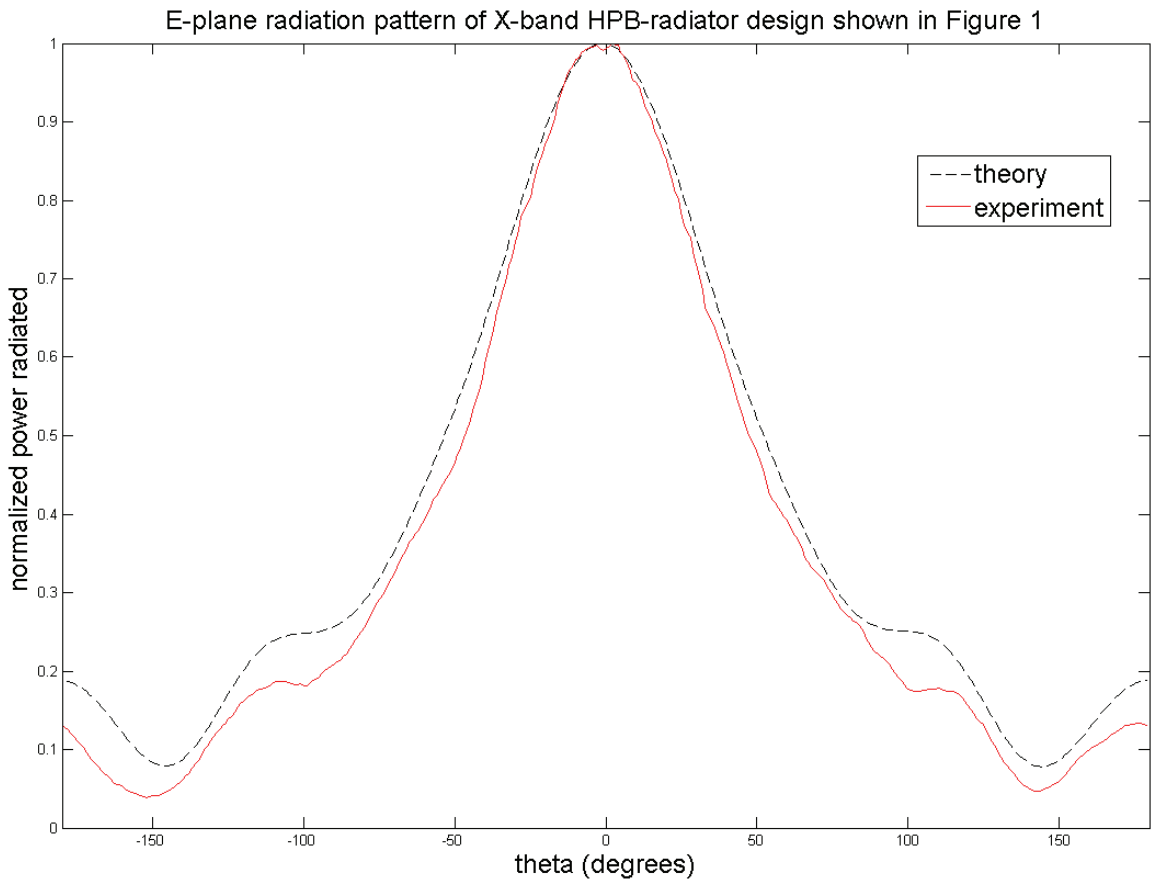
Figure 5.5(b). E-plane radiation pattern of X-band HPB-radiator.
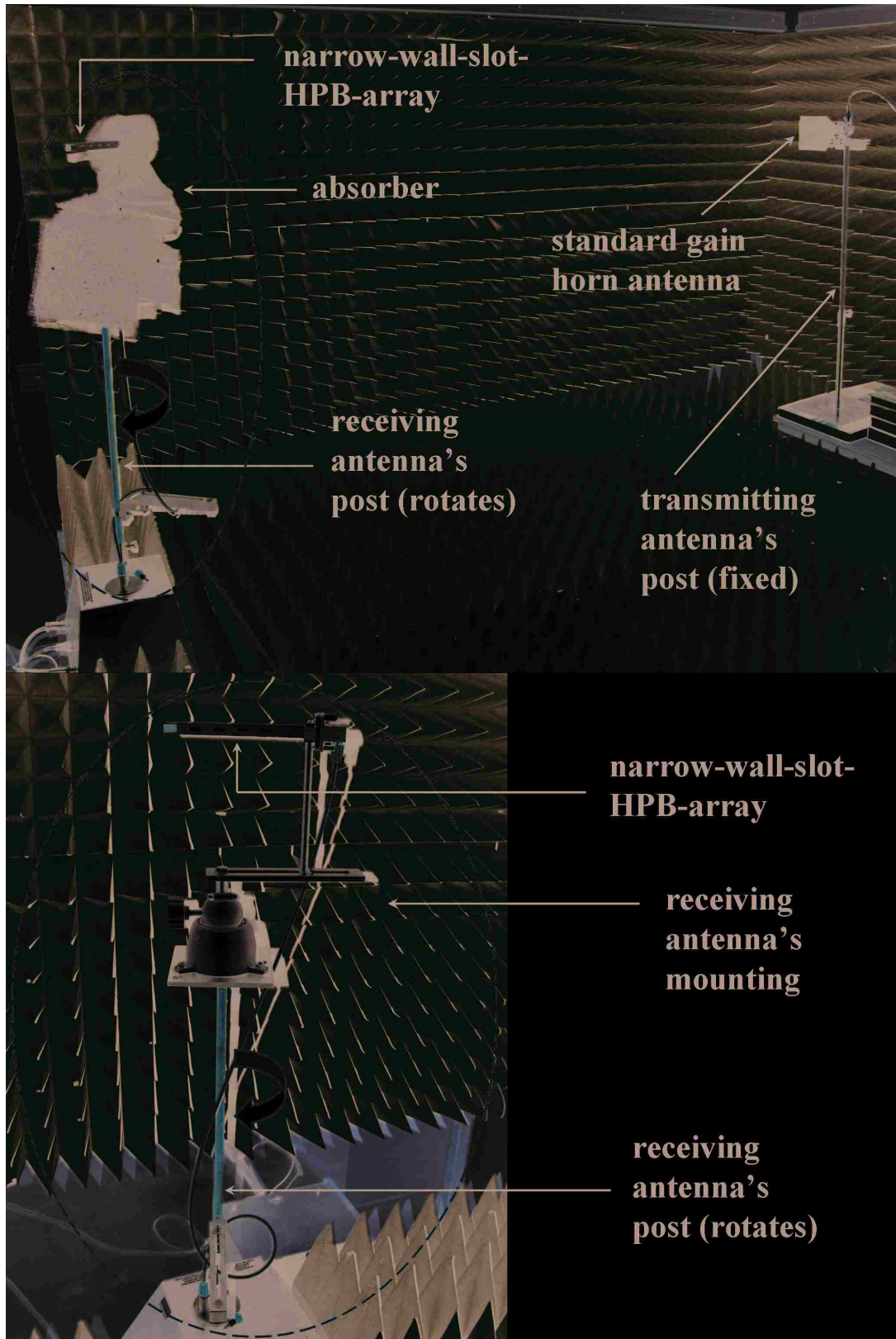
Figure 5.6(a). Experimental set-up used to measure the H-plane radiation pattern of X-band narrow-wall-slot-HPB-array.

Figure 5.6(b) compares the theoretical and experimental H-plane radiation power patterns of the X-band narrow-wall-slot-HPB-array design; $\theta = 0^o$ on the horizontal axis of the plot in Figure 5.6(b) corresponds to the broadside direction of the X-band narrow-wall-slot-HPB-array. The experimental H-plane radiation power pattern is shifted by 4° in Figure 5.6(b), so that the peaks of both patterns line up for making beam-width comparison easier.

Figure 5.6(b). H-plane radiation pattern of X-band narrow-wall-slot-HPB-array.
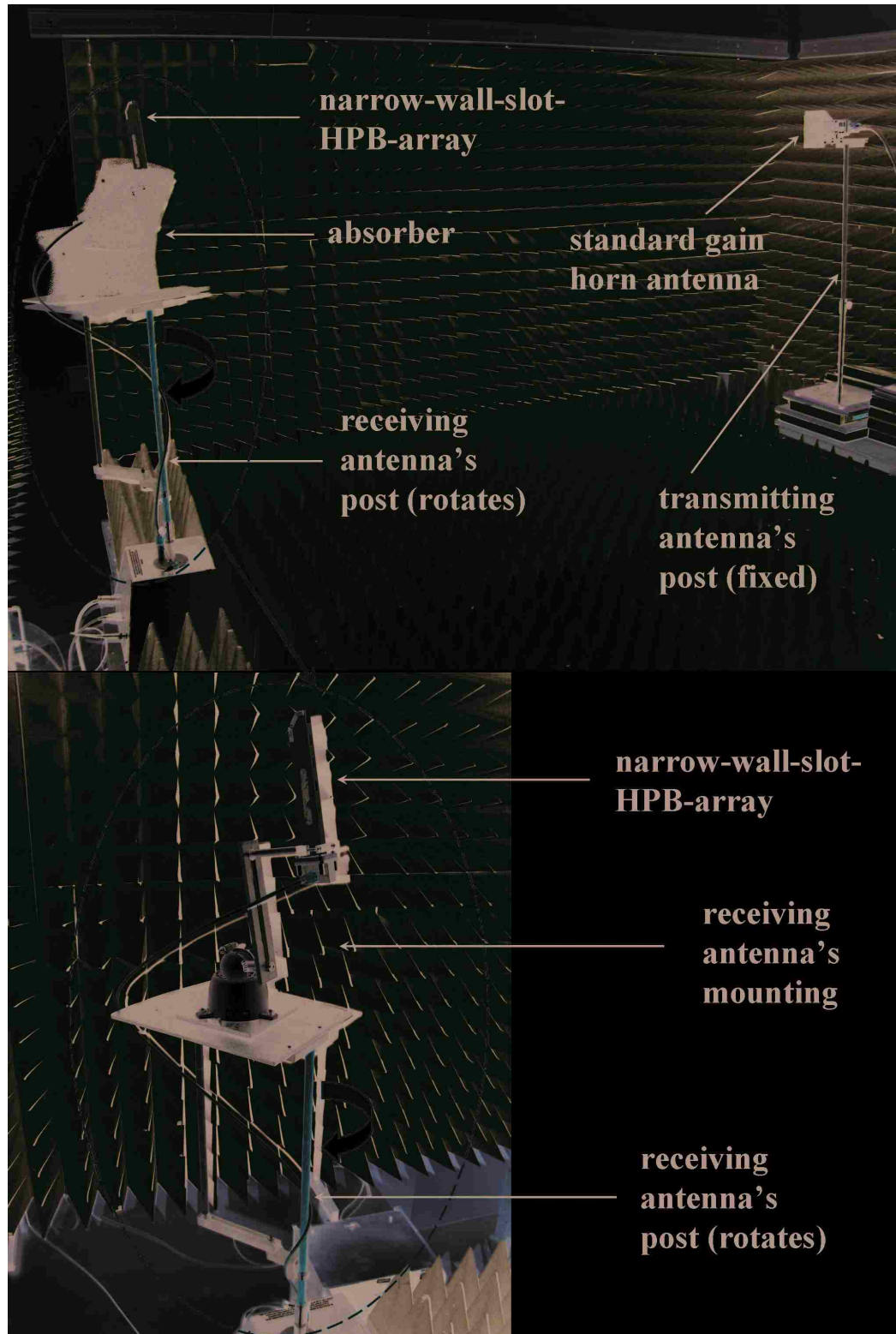
Figure 5.7(a). Experimental set-up used to measure X-band narrow-wall-slot-HPB-array's radiation pattern in the plane cut orthogonal to the H-plane and passing through θ=-18° line shown in Figure 5.6(b).

Figure 5.7(b) compares the theoretical and experimental radiation power patterns of the X-band narrow-wall-slot-HPB-array design in the plane cut that is orthogonal to the H-plane and passing through the θ = -18° line shown in Figure 5.6(b); θ = 0° on the horizontal axis of the plot in Figure 5.7(b) corresponds to the same spatial point in the 3-D radiation power pattern as θ = -18° on the horizontal axis of the plot in Figure 5.6(b).

Radiation pattern in orthogonal plane to H-plane & passing through theta=-18° line marked in Figure 5.6(b)
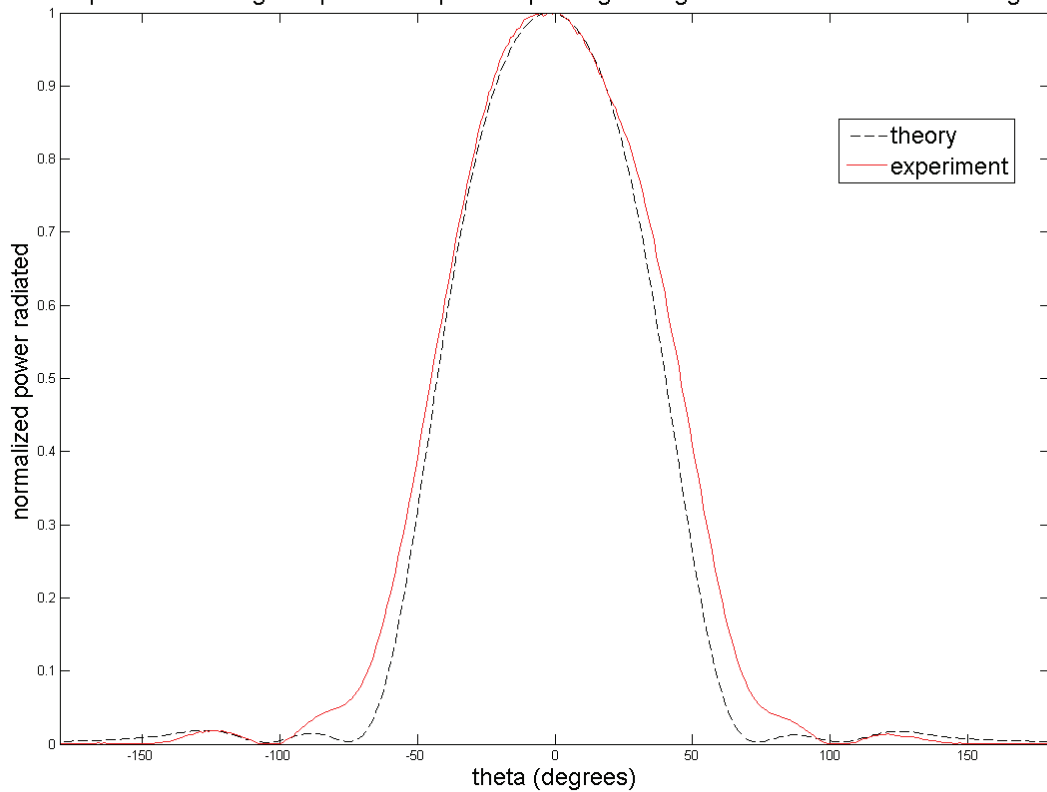
Figure 5.7(b). X-band narrow-wall-slot-HPB-array's radiation pattern in the plane cut orthogonal to the H-plane and passing through the θ=-18° line shown in Figure 5.6(b).

Figure 5.8(a) (5.8(b)) shows the orientation of the standard gain horn antenna in the experimental set-ups shown in Figures 5.4(a) (5.5(a)) and 5.6(a) (5.7(a)) for measuring the radiation patterns in the H-plane (plane cut orthogonal to the H-plane).
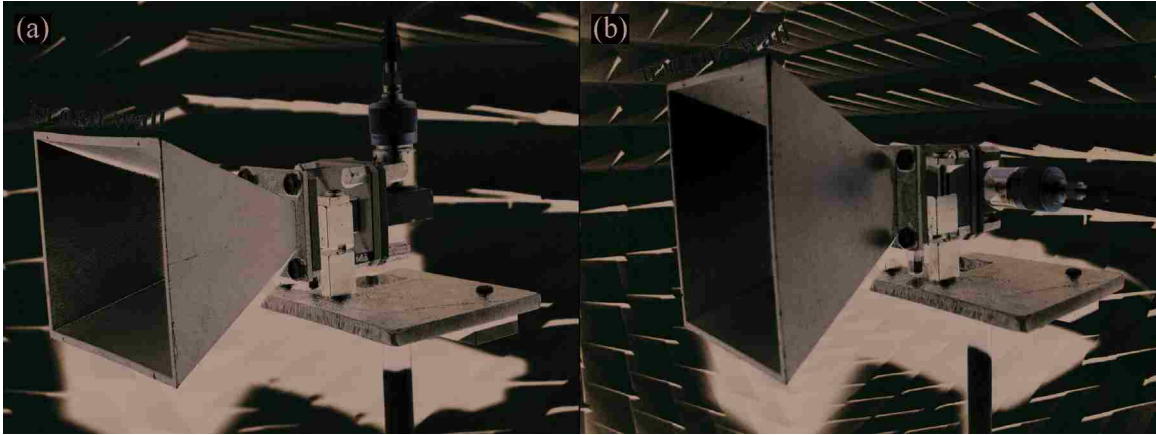
Figure 5.8. (a) Orientation of the standard gain horn in Figures 5.4(a), 5.6(a). (b) Orientation of the standard gain horn in Figures 5.5(a), 5.7(a).

5.2 <u>Array designs in the industrial frequency band</u>

In terms of the peak gain achieved by the array designs, the double-narrow-wall-slot-HPB-array and double-split-waveguide-HPB-array designs that were discussed in Sections 3.3 and 4.1 respectively are the best array designs available.

To further improve the directivity of their radiated fields, a wire mesh of appropriate dimensions can be used as a ground plane for the apertures of the double-narrow-wall-slot-HPB-array and double-split-waveguide-HPB-array.

Figure 5.9 (5.10) compares the radiation patterns of the arrays in the H-plane (plane cut that is orthogonal to the H-plane and passing through the $\theta = -17^o$ line shown in Figure 5.9). The H-plane radiation power pattern of the double-split-waveguide-HPB-array is shifted by 8° in Figure 5.9, so that the peaks of both patterns line up for making beam-width comparison easier.
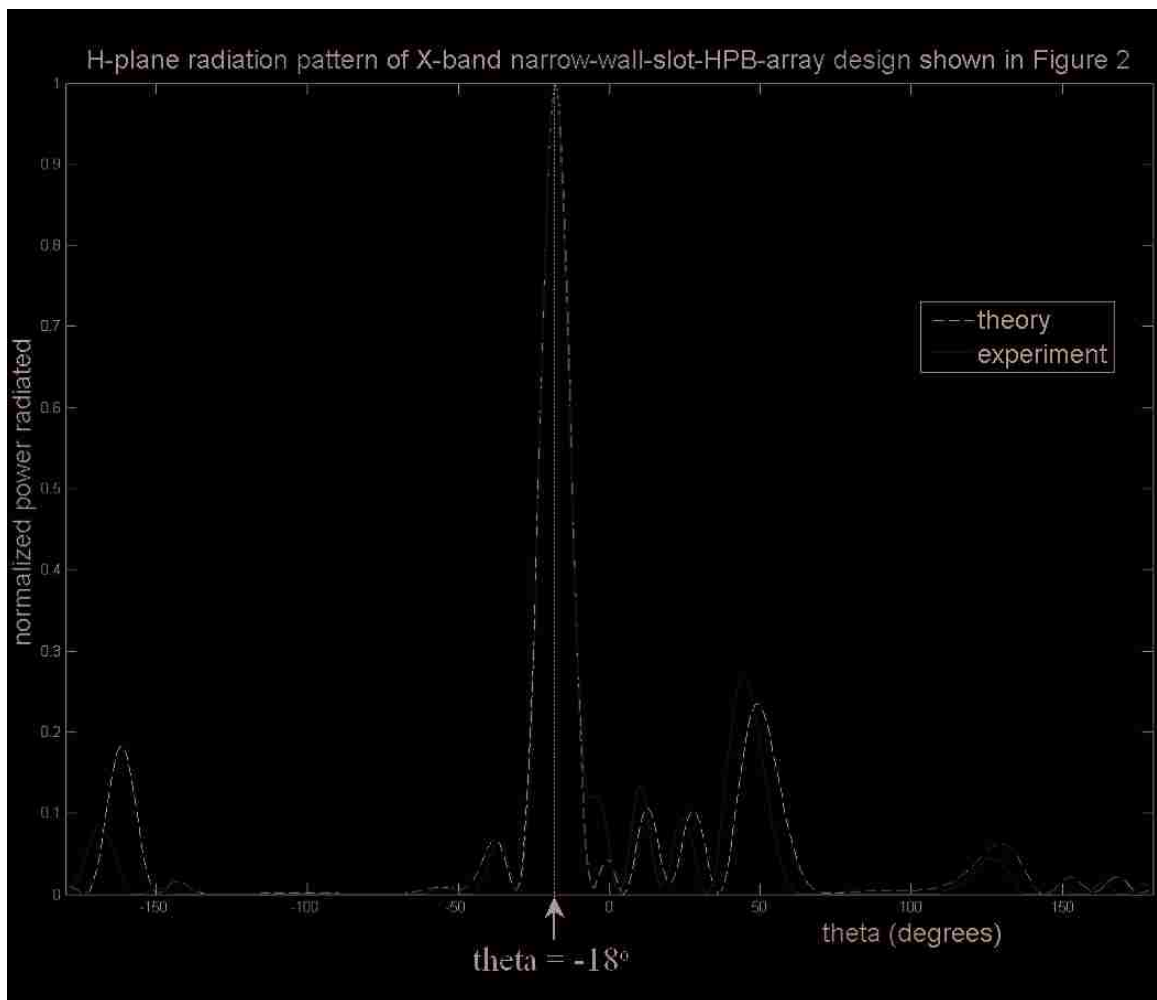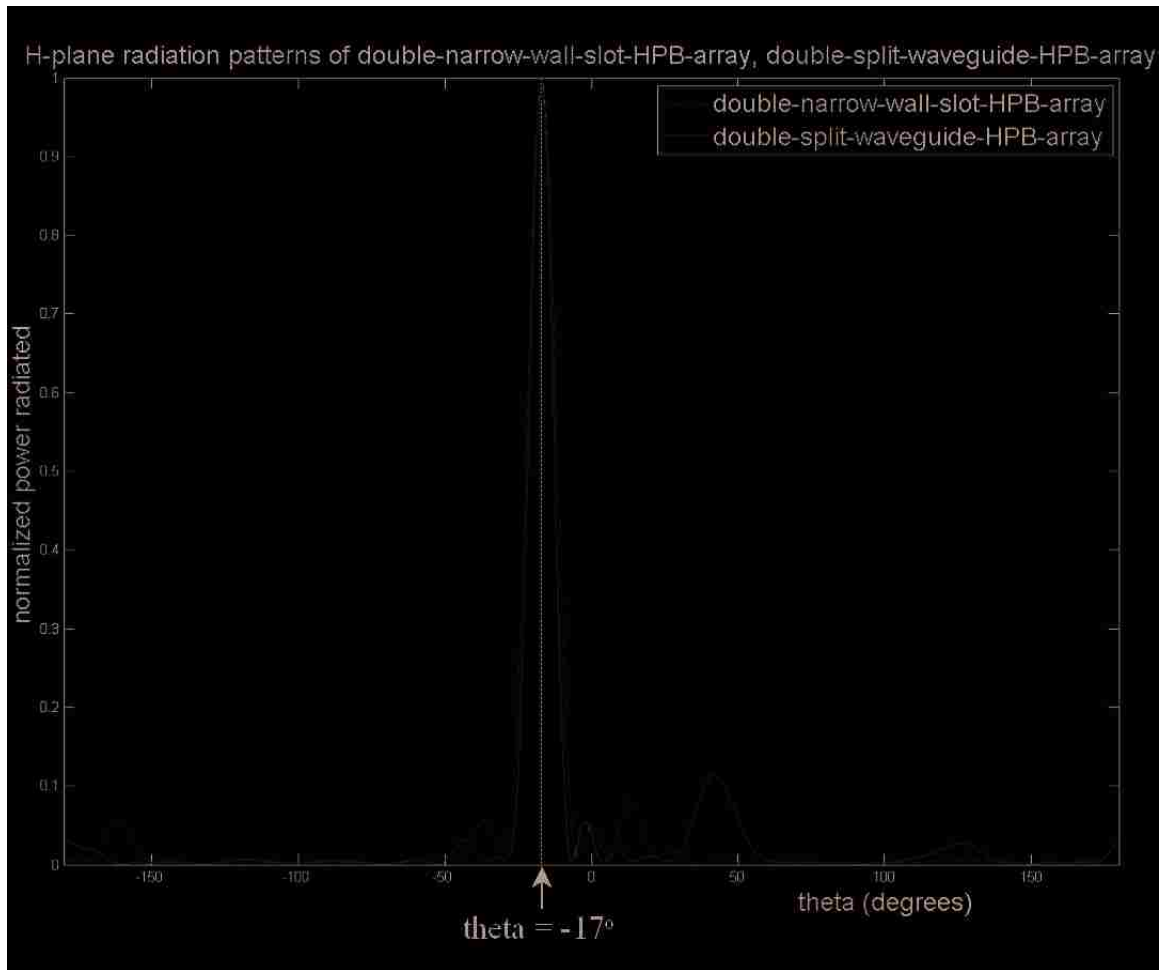
**Figure 5.9. H-plane radiation patterns of the double-narrow-wall-slot-HPB-array, double-split-waveguide-HPB-array.**
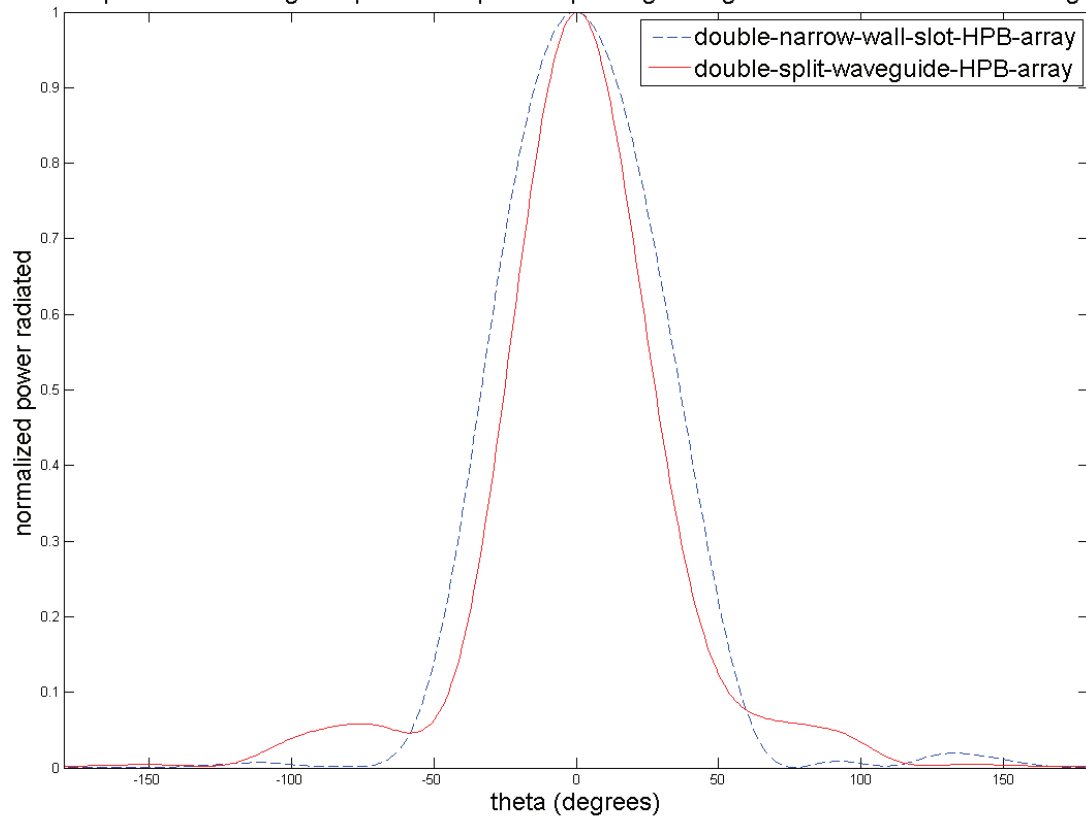
Figure 5.10. Radiation patterns of the double-narrow-wall-slot-HPB-array, double-split-waveguide-HPB-array, in the plane cut orthogonal to the H-plane and passing through the θ=-17° line shown in Figure 5.9.

In this section, the dimensions of the double-narrow-wall-slot-HPB-array and the double-split-waveguide-HPB-array designs at 10GHz are scaled up for operation in the industrial (ISM i.e. Industrial, Scientific and Medical) radio band. The ISM frequency band ranges from 902MHz to 928MHz. The scaling up of dimensions is only to change the operating frequency and needs to be such that the performance of the waveguide antennas is still identical, i.e. the gain of the antenna, the reflected power into the feed-waveguide are the same for the X-band and ISM band antennas. For the TE$_{10}$ mode of

operation, the WR-975 (L-band) waveguide supports the ISM band frequency signals. The goal of the analysis is to find the operating frequency in the ISM band (f_L) and the proportionality constant (C) that is used to scale up the dimensions of the array designs at 10GHz for operation at the frequency of choice in the ISM band.

The free-space wavelength (λ_X) at 10GHz is 30mm. The broad dimension (a_X) of an X-band waveguide that is also used to compute the guide wavelength at 10GHz (λ_{gX}) is 22.86mm. So, for a standard X-band waveguide under the dominant (TE_{10}) operating mode at 10GHz, λ_{gX} is 39.7554mm. Therefore the ratio of λ_{gX} over λ_X at 10GHz (ratio-X) is 1.3252.

λ_L is the free-space wavelength in the ISM band that needs to be computed. The broad dimension (a_L) of a standard L-band waveguide is 247.65mm. λ_{gL} is the guide wavelength that is computed from λ_L and a_L. The value of λ_L is iterated on, until the ratio of λ_{gL} over λ_L (ratio-L) is equal to ratio-X. The choice for λ_L that satisfies the condition, ratio-L = ratio-X, is approximately 325mm. Hence the corresponding operating frequency of choice in the ISM band (f_L) with an L-band waveguide as the feed-waveguide is approximately 922.4MHz. So, for a standard L-band waveguide under the dominant (TE_{10}) operating mode at 922.4MHz, λ_{gL} is approximately 430.7mm.

Once 'f_L' is known, 'C' is simply λ_{gL} over λ_{gX} and is approximately 10.8473. Hence, all the dimensions that make up the double-narrow-wall-slot-HPB-array and the double-split-waveguide-HPB-array designs at 10GHz need to be multiplied by C = 10.8473 to obtain the corresponding array designs operating in the ISM band at 922.4MHz.

The power handling capability analysis for the array designs in the ISM band is done with the aid of HFSS. Full-wave analysis is performed on the array designs at 922.4MHz. The magnitudes of the E-field values inside the structures are obtained and the maximum field values are recorded. The well-known electrical air breakdown value of approximately 3MV/m in *[Lide, dielectric strength]*, *[Rees]* for static fields at one atmosphere of air pressure is used as the upper limit for the maximum allowable E-field values inside the structures. So, for the double-narrow-wall-slot-HPB-array (double-split-waveguide-HPB-array) operating at 922.4MHz, at an air pressure of one atmosphere, an input power of approximately 80MW (100MW) through the L-band feed-waveguide produced air breakdown inside the structure.

The air pressure at sea level is one atmosphere or 760Torr *[Goody]*, *[Lide, pressure units]*. When operating the antennas at increasing altitudes above sea level, the value of air pressure falls *[Goody]*; consequently, the electrical air breakdown value also falls *[Rees]*. As a result, the maximum allowable power through the L-band feed-waveguide needs to be appropriately adjusted depending on the altitude above sea level.

The pressure at an elevation of 'h' meters above sea level can be computed using Equation 5.1 *[Goody]*.

$$p(h) = p(0) \; e^{-\left(\frac{h}{H}\right)} \qquad \textbf{(5.1)}$$

Where:

$p(h)$ is the pressure at an elevation of 'h' meters above sea level

$p(0)$ = 760Torr is the pressure at an elevation of zero meters above sea level

H = 8400 meters is the approximate scale height of the Earth's atmosphere *[Goody]*

Between the air pressure values of approximately 260Torr and 760Torr: the electrical air breakdown values are directly proportional to the air pressure values *[Rees, sparking potentials]*, and can be computed using Equation 5.2. Using Equation 5.1, the air pressure on Mount Everest can be approximated to 265Torr. Since the antennas are to be mounted on a land vehicle, in the above-mentioned range of air pressure values for which Equation 5.2 is valid, the lower limit (260Torr) is adequate for the design purpose.

$$E\_field\_Br = \frac{(p)(E\_field\_Br_0)}{p_0} \qquad \textbf{(5.2)}$$

Where:

p_0 = 760Torr is the air pressure at an elevation of zero meters above sea level

$E\_field\_Br_0$ = 3MV/m is the breakdown E-field value for static fields at an air pressure of p_0 = 760Torr

p is the value of air pressure between the values of 260Torr and 760Torr

E_field_Br is the breakdown E-field value for static fields at an air pressure of 'p' Torr

It is now illustrated how the power handling capability of a high power antenna is affected by the location where it is operated. Consider for instance that the location under consideration is Albuquerque, New Mexico, U.S.A. at an elevation of approximately 1610 meters above sea level. From Equation 5.1, the air pressure at this elevation (h=1610m) can be computed to be approximately equal to 627.44Torr. Note that this value of pressure (p) is between the values of 260Torr and 760Torr that are mentioned above. Since the electrical air breakdown value for static fields at an air pressure of 760Torr is approximately equal to 3MV/m, the corresponding air breakdown value at 627.44Torr is computed from Equation 5.2 and is approximately equal to 2.48MV/m.

Therefore, for the double-narrow-wall-slot-HPB-array (double-split-waveguide-HPB-array) operating at 922.4MHz, at an elevation of 1610 meters above sea level, an input power of approximately 66.05MW (82.56MW) through the L-band feed-waveguide would produce air breakdown inside the structure. This is approximately 82.56% of the amount of power that the corresponding array can handle at one atmosphere of air pressure.

6. FUTURE WORK

6.1 <u>Circularly polarized rectangular waveguide narrow-wall aperture array designs</u>

The array designs in Chapters 3 and 4 produce the same polarization as the structure in *[SSN 503]* and are complementary to that in *[SSN 459]*. Both types of structures are required to produce vertical as well as horizontally polarized radiated power. The structures can be used in one of the following two ways to achieve both polarizations. The two structures can be powered at the same time but with a phase shift of $\pm 90^{\circ}$ introduced between their inputs, thereby resulting in circularly polarized radiated power. In this circularly polarized mode of operation, the peak power available at the source is almost always shared between the horizontal and vertical polarization directions of the radiated field. The two structures can also be powered one after the other and not simultaneously, such that the peak power available at the source is radiated half of the time in the vertical/horizontal polarization direction. In this mode of operation the duty cycle for each structure is reduced to half.

The need for two high power antennas to radiate both vertically and horizontally polarized power can be eliminated by developing a single high power waveguide antenna that radiates circularly polarized power. The options for this single structure are shown in Figures 6.1, 6.2 and 6.3. Some existing waveguide antennas that produce circularly polarized radiated fields can be found in *[Armstrong]*, *[Montisci]*; but the structures shown in Figures 6.1, 6.2 and 6.3 are better suited for high power applications. The bends in Figures 6.1, 6.2 and 6.3 can be optimized for minimum reflections using the same techniques that were used to design the HPB-radiator's H-plane taper (discussed in Chapter 2). The advantage of the circular-polarized-slot-array over the circular-polarized-

slot-HPB-array and the circular-polarized-split-waveguide-HPB-array is its structural simplicity. Unlike the circular-polarized-slot-HPB-array, the inter-element spacing between 'all' of the apertures of the circular-polarized-slot-array is designed to obtain circularly polarized radiated fields and cannot be used as a free design variable to minimize the reflected power. Unlike the arrays in Figures 6.1 and 6.2, the circular-polarized-split-waveguide-HPB-array can beam steer because of its split-waveguide input.
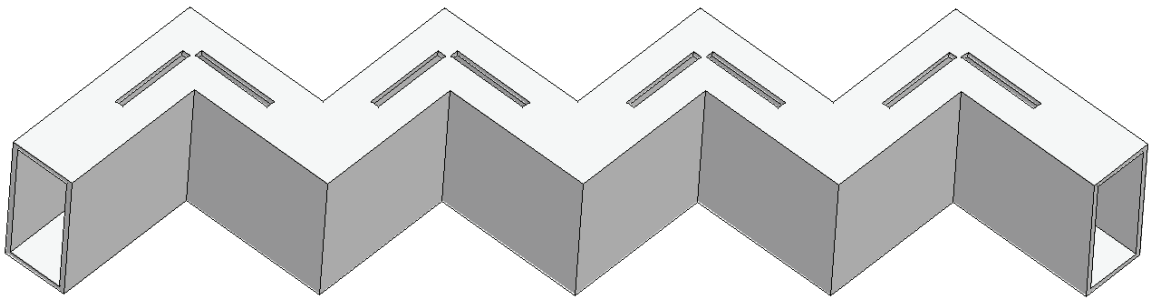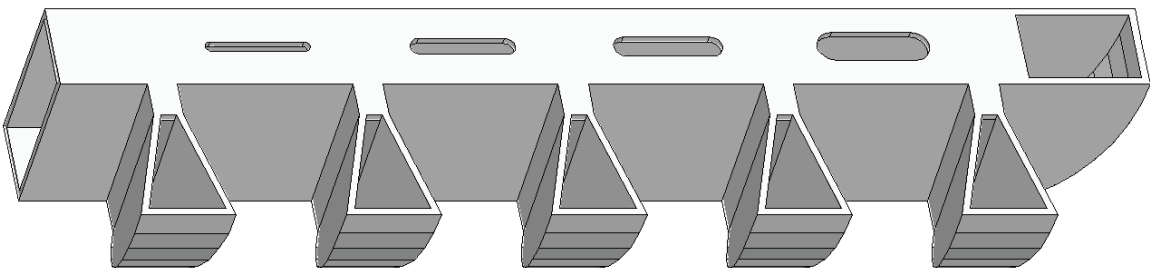

Figure 6.1. Circular-polarized-slot-array.

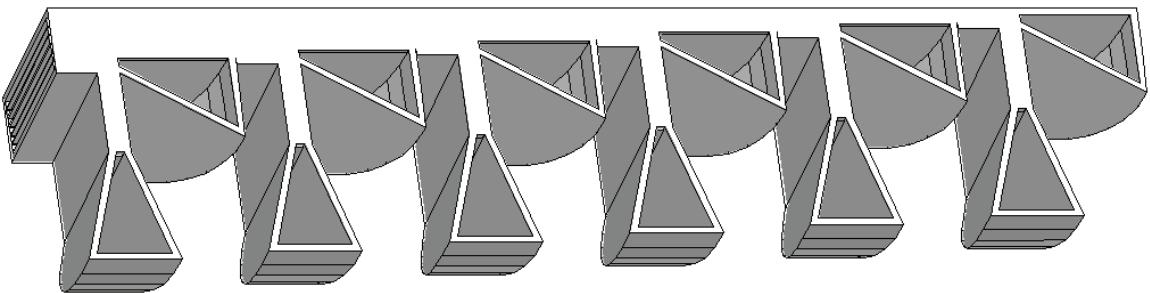Figure 6.2. Circular-polarized-slot-HPB-array.

Figure 6.3. Circular-polarized-split-waveguide-HPB-array.

6.2 <u>Modified narrow-wall-slot-HPB-array for higher gain</u>

Although the gain of the narrow-wall-slot-HPB-array is smaller compared to the double-narrow-wall-slot-HPB-array and the double-split-waveguide-HPB-array, its structural simplicity is its advantage. Therefore it can be investigated whether the gain of the narrow-wall-slot-HPB-array can be improved by slightly increasing its structural complexity. Adding a design variable to the narrow-wall-slot-HPB-array's design procedure, discussed in Chapter 3, might achieve this. The design variable under consideration is the broad dimension of the waveguide.

By including the narrow dimension as well as the broad dimension of the guide in the design variables, it needs to be verified whether the number of apertures radiating in harmony can be increased while keeping the overall length of the array constant. This would decrease the distance between the apertures, resulting in a more uniform aperture field distribution along the length of the array. The criterion that needs to be satisfied while changing the guide dimensions is that for the operating frequency under consideration, the dominant mode still needs to be the TE_{10} mode.

Following are some design considerations when the number of array elements is increased. When the narrow-wall-slot-HPB-array had only five elements as shown in Figure 3-1, in the ideal case scenario, the fractional power radiated by each element when compared to the fractional power at the input of each element ranged from 0.2 through 1; when the number of elements is increased to say ten, the same range is now 0.1 through 1. The implications of this can be that the length offset between the shortest and longest slots that is needed to produce the above mentioned higher range could make the uniform array criteria invalid. Therefore the maximum number of array elements is limited by the

maximum length offset that can be tolerated between the shortest and longest slots. More care is also needed while designing the spacing between the elements. This is due to the fact that the guide wavelength along the length of the waveguide can change even for a single frequency, since the broad dimension of the guide is included as a design variable. It needs to be verified whether by changing the dimensions of the slots appropriately along the guide, the inter-element spacing between all the elements can be kept the same and the uniform array criteria still holds. A modified narrow-wall-slot-HPB-array configuration for higher gain might look like the structure shown in Figure 6.4. Note that the (broad-wall/narrow-wall) taper shown in Figure 6.4 may not be linear.
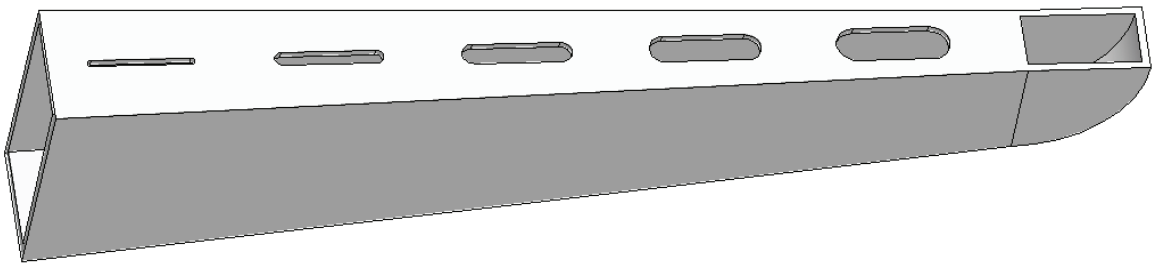

Figure 6.4. Modified narrow-wall-slot-HPB-array for higher gain.

REFERENCES

[Armstrong]

N. E. Armstrong, N. G. Alexopoulos; **On the Design of a Circularly Polarized Waveguide Narrow Wall Linear Array**; IEEE Trans. Antennas Propag., vol. 23, pp. 244-250, Mar. 1975.

[Balanis]

C. A. Balanis; **Antenna theory analysis and design**; John Wiley & Sons, New York, 1997.

[Collin]

R. E. Collin; **Field Theory of Guided Waves**; The Institute of Electrical and Electronics Engineers, Inc., New York, 1991.

[Goody]

R. M. Goody, J. C. G. Walker; **Atmospheres**; Prentice-Hall, Inc., New Jersey, 1972.

[Jasik]

H. Jasik; **Antenna Engineering Handbook**; McGraw-Hill Book Company, New York, 1961.

[Kraus]

J. D. Kraus; **Antennas**; McGraw-Hill Book Company, New York, 1950.

[Lee]

K. S. H. Lee, editor; "Table 14. Aperture Polarizabilities" in **EMP interaction: Principles, techniques, and reference data**; Hemisphere Publishing Corp., Washington, DC, 1986.

[Lide, dielectric strength]

D. R. Lide, editor; "Table 1. Dielectric Strength of Gases" in **CRC Handbook of Chemistry and Physics**; 89th Edition (Internet Version 2009), CRC Press / Taylor and Francis, Boca Raton, FL.

[Lide, pressure units]

D. R. Lide, editor; "CONVERSION FACTORS FOR PRESSURE UNITS" in **CRC Handbook of Chemistry and Physics**; 89th Edition (Internet Version 2009), CRC Press / Taylor and Francis, Boca Raton, FL.

[Montisci]

Giorgio Montisci; **Design of Circularly Polarized Waveguide Slot Linear Arrays**; IEEE Trans. Antennas Propag., vol. 54, pp. 3025-3029, Oct. 2006.

[Pozar]

D. M. Pozar; **Microwave Engineering**; John Wiley & Sons, New York, 2005.

[Rees]

J. A. Rees, editor; **Electrical Breakdown in Gases**; Halsted Press / John Wiley & Sons, New York, 1973.

[Rees, sparking potentials]

J. A. Rees, editor; "Figure 3. Calculated (x) and observed (o) sparking potentials in air" in **Electrical Breakdown in Gases**; Halsted Press / John Wiley & Sons, New York, 1973.

[SSN 459]

C. E. Baum; **High Power Scanning Waveguide Array**; Sensor and Simulation Notes, Note 459. http://www.ece.unm.edu/summa/notes/SSN/Note459.pdf

[SSN 503]

C. E. Baum; **Sidewall Waveguide Slot Antenna for High Power**; Sensor and Simulation Notes, Note 503. http://www.ece.unm.edu/summa/notes/SSN/Note503.pdf

[Stevenson]

A. F. Stevenson; **Theory of Slots in Rectangular Wave-Guides**; J. Appl. Phys., vol. 19, January 1948, pp. 24-38.